Towards Surpassing the Standard Quantum Limit Using Optical Springs

John Macarthur BSc (Hons)

School of Physics and Astronomy

University of Glasgow

Submitted in fulfilment of the requirements

for the degree of Doctor of Philosophy

September 2014

j.macarthur.1@research.gla.ac.uk

Abstract

The existence of Gravitational waves is a prediction that arose from Einstein's theory of general relativity. So far their direct detection has eluded scientists with Einstein himself believing they would never be detected. However, recent developments in advanced interferometric detectors should allow the first detections to be made when they are commissioned later this decade. This will open up an entire new field of astronomy giving deeper understanding to the physics of and proving Einstein's general theory of relativity.

Astronomers always want bigger telescopes whether it is to see further or to see more detail and this will no doubt occur with gravitational wave telescopes. Hence, further improvements in sensitivity will be required. This thesis examines techniques for improving sensitivity beyond the standard quantum limit, a future limit to sensitivity, using optical rigidity.

By coupling two suspended cavity mirrors together using only the light circulating between them the response of the system changes such that a linear restoring force is created on both cavity optics, the "optical spring".

The first experiment carried out in the scope of this thesis shows how an intentionally applied signal that changes the position of the input mirror in a rigidly coupled cavity is transferred via the optical spring to a position change

of the output cavity mirror. A small independent interferometer, a so-called local readout, is used to monitor the displacement of the output cavity mirror allowing the position of the input mirror to be inferred. This experiment verifies that it is possible to gather information on the position of the input mirror via the local readout interferometer the photons of which have never interacted with the input mirror. The local readout device was able to measure a coupled motion between the cavity mirrors, via the optical spring, of 10^{-13} m at 922 Hz. Hence this experiment can be considered as the first demonstration of an optical bar configuration which has been previously shown to be a type of quantum non-demolition measurement.

In the second experiment an optical spring, present in a 10 m cavity used as a frequency reference, provides a peak in the optical gain of this cavity. The peak in gain, due to the resonance of the optical spring, is then shown to enhance the frequency stability of the 10 m cavity around the optical spring frequency. An increase in sensitivity of 3 dB across a 50 Hz window centred around 200 Hz was measured showing that this is a good example of how the optical spring can also be used to improve high-precision classical measurements.

Overall this thesis provides examples of how optical springs can be used as a building block for improvements of high precision interferometry and quantum measurement. These technologies are likely to play a key role in future gravitational wave detectors such as the Einstein Telescope.

"Give me a lever long enough and a fulcrum on which to rest it, and I can move the world."

- Archimedes

Acknowledgements

First and foremost I wish to thank both of my supervisors Kenneth Strain and Stefan Hild, for introducing me to the fascinating field of gravitational wave detection and for their guidance throughout my time in the IGR.

Ken's seemingly encyclopedic knowledge of not just interferometry and physics but many other fascinating topics to boot proved invaluable and often very insightful. He was always available for a chat about problems and saved many hours of floundering in the lab.

Stefan's untiring enthusiasm even when things were at their worst was always a great comfort and helped me never to get too down hearted. He also provided excellent advice throughout my PhD.

Although generally assigned two supervisors I feel privileged and very fortunate to have ended up with what feels like three. Bryan Barr seems to make his way into a lot of acknowledgement sections and for good reason. His grasp of the subject both theoretical and experimental is vast and his patience in explaining it even more so. Although tested to its limits during my time his patience in breaking things down into chunks even single celled organisms could digest was vital to me in getting to this stage. Perhaps most importantly he was also always available for curry and beer.

The rest of the interferometry group were a pleasure to work with and the IGR as a whole provided a great working environment with incredibly clever driven individuals at the forefront of great research and kept me fascinated with the field throughout my PhD.

Others who deserve special thanks for both helpful work discussion as well as many an entertaining coffee break are Angus Bell, Chris Bell, Christian Killow, Borja Sorazu, Gail Penny, Iain Martin, Jamie Scott, Jenny Anderson, Kieran Craig, Matt Pitkin, Mike Perreur-Lloyd, Morag Casey, Neil Gordon, Peter Murray, Russell Jones, Sean Leavey and Siong Heng.

Finally I wish to thank the most important people Mum, Dad, Katherine and Lorna for their continued support, especially throughout the last 4 years.

Preface

Chapter 1- This chapter will give an introduction to the topic of gravitational waves including the background theory and the properties of gravitational waves. We will also discuss sources of gravitational wave signals, what we expect them to look like and estimates of their size given realistic parameters.

Chapter 2- This chapter will focus on the history and development of gravitational wave detection principles and methods. We will concentrate on ground based detectors, specifically interferometry techniques, noise sources which limit improved sensitivity and current limits of the technology. We will also give some insight into how these detectors operate.

Chapter 3- This chapter will discuss the basic concepts and mathematical derivations of optical rigidity. We will look at the field equations of an optical cavity and the power coupling that arises. In addition we will also look at suspended mirror dynamics and finally how the two interact to create optical rigidity.

Chapter 4- This chapter details the experimental apparatus used that was common to the two main experiments described in Chapters 5 and 6. It describes the lab environment, layout and some of the most important subsystems

used.

Chapter 5- This chapter describes the first experiment undertaken, showing the first demonstration of an optical bar topology using local readout methods. We show an opto-mechanically coupled cavity can be used to transfer motion of one mass to the other via the light field. More so, by monitoring the position of one mirror, information can be obtained about the motion of the other.

Chapter 6- This chapter details the second experiment undertaken, showing the idea of improving a classical measurement with quantum technology. Namely using detuned reference cavities as a way to improve the sensitivity of a measurement. Here a frequency noise limited cavity response can be altered by introducing an optical spring.

Chapter 7- This chapter sums up the conclusions and discussions of the work in this thesis and finishes with future work to be done in this area.

Constants, Variables and Abbreviations

Symbol	Description
c	$2.99792458 \times 10^8\, m/s$ Speed of light in vacuum
CDS	Control and data system
CTM	Central Test Mass
δ	Detuning (Hz)
δ_γ	Detuning parameter δ/γ
Δx	Difference in x
EOM	Electro-optic modulator
ETM	End Test Mass, cavity mirror furthest from laser
$EUCLID$	**E**asy to **U**se **C**a**L**ibrated **I**nterferometric **D**evice
f_{mod}	Modulation Frequency
f_{las}	Laser Frequency
f_{os}	Optical Spring Frequency
F_{RP}	Radiation pressure force
$\mathcal{F}$	Finesse
FSR	Free spectral range ($c/2L_{cav}$)
GW	Gravitational wave
γ	Cavity Linewidth(Hz) (HWHM of Airy peak)
h	$6.62606957 \times 10^{-34}\, m^2 kg/s$ Planck's Constant

$HWHM$	Half Width at Half maximum
ITM	Input Test Mass, cavity mirror nearest the laser
k_{os}	Optical spring constant (n/m)
$K_{os}(\Omega)$	Frequency dependant optical spring response
L_{cav}	Cavity length (m)
$LIGO$	**L**aser **I**nterferometer **G**ravitational wave **O**bvservatory
m_{red}	Effective mass or reduced mass of a system
P_{in}	Power input to cavity
P_{cav}	Intracavity power
PDH	Pound Drever Hall
PZT	Piezo transducer
ρ	Reflectivity
SQL	Standard Quantum Limit
τ	Transmission
UGP	Unity gain point (Servo gain = 1)
ω_0	Laser angular frequency $(2\pi f_{las})$
Ω	Sideband frequency

Contents

List of Figures

List of Tables

Chapter 1

Gravitational Wave Theory From General Relativity

1.1 Introduction

For many years Isaac Newton's description of gravity [1] and how mass interacts stood up to many tests and indeed led to the discovery of many planets and astronomical events. The perihelion of Mercury was the first evidence of shortcomings in Newton's theory. One other problem with Newton's theory was the idea that moving one object instantaneously had an effect on another regardless of the distance separating them. This in principle allowed faster than light data transfer which requires an infinite amount of energy to accelerate a particle, which has rest mass, to the speed of light. James Clerk Maxwell was able to show for charged particles that moving one charge did not instantaneously effect another but created a disturbance in the magnetic and electric field which propagated at the speed of light [2]. However, it was not until the early 20th century when Albert Einstein was able to unify the classical laws

of Newtonian physics with those of electrodynamics. Firstly with the theory of Special Relativity [3] where the two main outcomes were that the laws of physics held true in any inertial frame of reference and the speed of light in a vacuum is constant. This theory only applied in the special case where the effect of gravity was negligible. It was not until 1916 that Einstein was able to incorporate gravitational effects and produce the General Theory of Relativity [4].

Two main outcomes of General Relativity are that the speed of light is a constant and that mass and energy are equivalent: $E = mc^2$. One aspect of this theory is that space time is altered by the presence of energy or mass and this in turn gives rise to gravitational fields. This then shows that asymmetrical accelerations of this mass would cause fluctuations or ripples in space time. Furthermore, these ripples would propagate at the speed of light, carrying with them information about the source that created them. The term used for these is gravitational waves. This is analogous to the electromagnetic waves produced by the acceleration of a charged particle in an electric field albeit on a weaker scale. The gravitational force is considered around 10^{36} times weaker than the electromagnetic force.

Due to the weakly interacting nature of the gravitational force, gravitational waves will propagate where electromagnetic waves would scatter and be absorbed. They therefore give details on astronomical events that have so far gone uninvestigated due to the lack of information provided by electromagnetic telescopes. However, the weak coupling to matter also makes gravitational waves very difficult to detect. Detection and analysis of gravitational waves would open up a new branch of astronomy and improve our understanding of the universe dramatically.

The following chapter gives a brief introduction to Relativity only so far as to

explain the generation and some of the more interesting properties of gravitational waves. Potential sources will then be discussed including the expected waveform size and shape. Finally a measurement which indirectly proves the existence of gravitational waves is discussed.

1.2 Relativity

A starting point for the mathematical description is to find and define the correct measurement of the distance between two points x^μ and $x^\mu + dx^\mu$ in space-time. This is called the invariant or proper distance and is given by

$$ds^2 = g_{\mu\nu} dx^\mu dx^\nu, \tag{1.1}$$

where $g_{\mu\nu}$ is the metric tensor determined through the Einstein field equations described as,

$$R_{\mu\nu} - \frac{1}{2} g_{\mu\nu} R = \frac{8\pi G}{c^4} T_{\mu\nu}, \tag{1.2}$$

where $R = g_{\mu\nu} R_{\mu\nu}$ is the scalar curvature, $R_{\mu\nu}$ is the Ricci tensor, G is the gravitational constant and $T_{\mu\nu}$ is the energy momentum tensor. When operating in the weak field, space time can be thought of as approximately flat meaning the equations can be linearised. In this case the metric tensor can be written as the Minkowski metric of flat space-time plus a small perturbation $h_{\mu\nu}$:

$$g_{\mu\nu} \approx \eta_{\mu\nu} + h_{\mu\nu}, \tag{1.3}$$

where the Minkowski metric is,

$$\eta_{\mu\nu} = \begin{pmatrix} -c^2 & 0 & 0 & 0 \\ 0 & 1 & 0 & 0 \\ 0 & 0 & 1 & 0 \\ 0 & 0 & 0 & 1 \end{pmatrix}. \tag{1.4}$$

For a suitable gauge choice (Lorentz gauge condition) the field equations in vacuum reduce to

$$\left(\nabla^2 - \frac{1}{c^2}\frac{\partial^2}{\partial t^2}\right)\bar{h}_{\mu\nu} = 0, \tag{1.5}$$

which has a wavelike solution of the following form:

$$\bar{h}_{\mu\nu} = h_0 A_{\mu\nu} e^{ik_\mu x^\mu}. \tag{1.6}$$

For our gauge choice solutions to this are transverse waves propagating at the speed of light. By operating in the transverse traceless gauge, a small adjustment to the original Lorentz gauge transformation and satisfies the Lorentz condition, $A_{\mu\nu}$ is constrained so that a wave traveling in the z direction is

$$\bar{h}^{TT}_{\mu\nu} = h^{TT}_{\mu\nu} = h_0 A^{TT}_{\mu\nu} e^{jk(ct-z)}, \tag{1.7}$$

where

$$A^{TT}_{\mu\nu} = \begin{pmatrix} 0 & 0 & 0 & 0 \\ 0 & h_+ & h_\times & 0 \\ 0 & h_\times & -h_+ & 0 \\ 0 & 0 & 0 & 0 \end{pmatrix}. \tag{1.8}$$

Going back to the proper distance from the origin to point$(x_0, 0, 0)h_+ = 1$ then gives

$$\Delta\ell = \int |\mathrm{d}s^2|^{\frac{1}{2}} = \int_0^\infty |\mathrm{g}_{xx}|^{\frac{1}{2}}\, \mathrm{d}x \approx [1 + \frac{1}{2}h_0]x_0. \tag{1.9}$$

A similar argument applies for displacement from origin to $(0, y_0, 0)$ giving

$$\Delta\ell = [1 - \frac{1}{2}h_0]y_0 \tag{1.10}$$

$$\Delta x = \frac{1}{2}h_0 x_o \tag{1.11}$$

i.e. the displacement between two particles is proportional to the original separation. For this reason strain sensitivity will be discussed in future chapters relating to gravitational wave detection as this is the important parameter to be sensitive to for their detection.

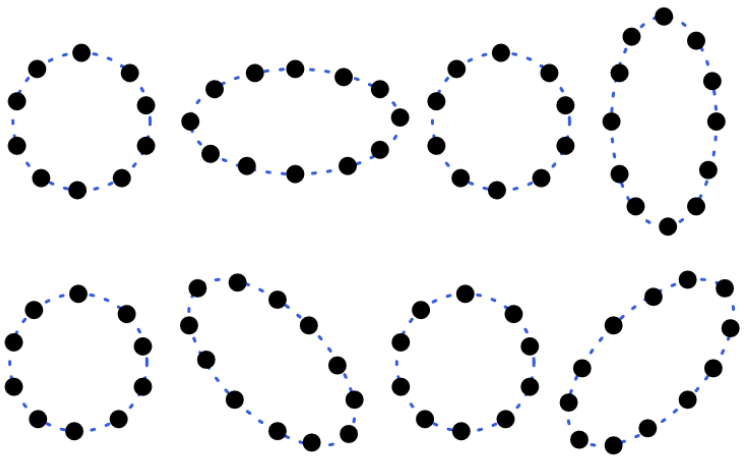

Figure 1.1: The effect a gravitational wave would have on a ring of particles evolving in time from left to right. The top row depicts + polarisation, while the bottom row depicts X polarisation with the rate of the contraction and expansion giving the frequency of the signal. The effect shown here is greatly exaggerated for ease of viewing and assumes the wave propagation is perpendicular to the page.

One of the interesting properties of gravitational waves is that they are predicted to be of quadrupolar nature, see Figure 1.1. This is due to mass always being positive and the gravitational force between objects being attractive.

1.3 Sources

From Einstein's theory of general relativity it follows that all accelerating masses emit gravitational waves. However, due to the mass dependance of these waves the effect from two people passing one another in a corridor or two lorries passing one another on a road will be extremely small. Astronomical

events are chosen as prime targets due to both their very large masses and in some cases very large accelerations. However a further problem is the $1/r$ drop-off in signal amplitude as the waves travel through space-time isotropically from the source. Even so, large astronomical events at kiloparsec (kpc) distance still have a much greater effect on space-time than any events that could be created on earth. Typical sources will now be briefly discussed describing the mechanism that allows for gravitational wave emission along with estimated strain given realistic parameters. The types of source we now describe are the most important signals for the frequency band of relevance to this thesis, 10 Hz-1 kHz [5].

1.3.1 Inspiral

Two neutron stars, two black holes or a neutron star and black hole pair whose orbits are decaying causing them to eventually coalesce are usually referred to as inspiral signals. This will cause a signal which gradually increases in amplitude over time as the period of the orbit decreases in the time before the two objects coalesce. An estimate can be made on the expected strain of such a signal using the following equation

$$h = 10^{-23} \left(\frac{100\,\mathrm{Mpc}}{r} \right) \left(\frac{M_b}{1.2 M_\odot} \right)^{5/3} \left(\frac{f}{200\,\mathrm{Hz}} \right), \tag{1.12}$$

where each bracketed property of the system is approximately unity.

1.3.2 Burst

So named as they are typically short, for example, collapsing supernovae and gamma ray bursts. Very little is known about these types of sources as they occur in violent events however the large masses and high accelerations involved

are ideal sources of gravitational waves. As such a lot of interesting science can be learnt from these types of signal.

1.3.3 Continuous Waves

These sources give rise to a repeatable pattern over a long time period and as such allow the signal to be integrated over that time giving an improved signal to noise ratio. For instance pulsars of uneven mass distribution would be emitters of gravitational wave signals. Initial LIGO was able to set spin-down limits from both the Crab and Vela pulsars[6]. Again an estimate can be made on expected strain caused by such a signal using the following equation,

$$h = 10^{-22} \left(\frac{f}{100\,\mathrm{Hz}} \right)^2 \left(\frac{1\,\mathrm{kpc}}{r} \right) \left(\frac{\epsilon}{10^{-6}} \right). \tag{1.13}$$

1.3.4 Stochastic

A stochastic source arises from the leftover remnants of the big bang giving an essentially white noise source in a similar way to the cosmic microwave background. The gravitational wave signal will have to occur much earlier in the explosion giving an even earlier view of the universe. Only non-standard inflationary cosmological models would produce waves in the band of interest. The BICEP experiment[7] gave some possible hints of this effect that are still under investigation but would indicate against the non-standard inflationary models. It is therefore unlikely to occur in this frequency band.

1.4 Indirect Proof of Existence

At the time of writing there has yet to be a direct detection of a gravitational wave. However, there has been indirect proof of their existence, i.e. measuring the effect a gravitational wave or gravitational wave emission has had on another object.

The most famous example of this is the Hulse Taylor pulsar or PSR B1913+16 which was seen to be orbiting a neutron star. The period of the radio pulses was measured over several years and was seen to decay exactly in accordance with the general theory of relativity shown in Figure 1.2 [8]. This suggested that the reduction in period of orbit was due to conversion of energy into gravitational waves. This work earned Hulse and Taylor the Nobel prize in physics in 1993.

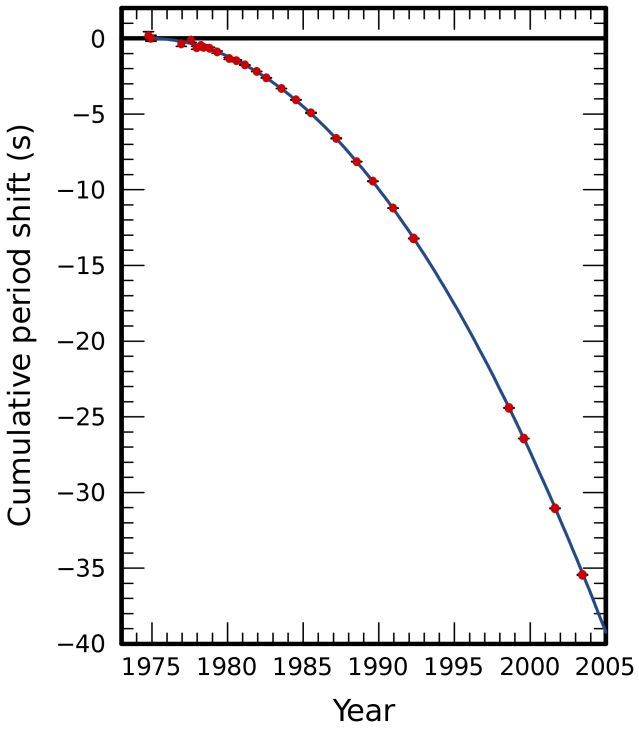

Figure 1.2: Plot showing the decay of two orbiting Neutron stars over the course of 30 years. Decay rate agrees exactly with Einstein's prediction of energy converted into gravitational waves [8].

Chapter 2

Gravitational Wave Detection

In the previous chapter the theory behind the production of gravitational waves was discussed. This chapter will look at the history and development of the field of gravitational-wave detection, focussing mainly on the ground-based interferometric type. We will then go into some detail of the basic detection principle of interferometry and move on to describe the sensitivity limitations of current GW detectors, techniques proposed to improve the instrument performance and finally we will give an outlook on potential long-term future developments.

2.1 History of Detectors

Although predicted in 1916, it was not until the 1960s that the first serious attempts were made to detect gravitational waves. This was due to many believing it to be near impossible to detect the very small strains caused by gravitational waves. The first experiments began with Joseph Weber [9] attempting

to measure the effect of a gravitational wave on a large aluminium bar. The bar weighed around 2000 kg and had a very narrow-bandwidth mechanical-mode resonance i.e. the oscillation was under-damped and so when excited amplified the signal and so the system is said to have a large Q factor. The principle of the experiment was that were a gravitational wave of the same frequency as the bar resonance to pass through the detector the signal would be amplified by the resonance to such an extent that it would be measurable by transducers mounted on the bar.

It soon became clear that these devices were not suitable for astronomy purposes as they are sensitive only at the very narrow linewidth, tens of Hz, of the mechanical resonance. A broadband detector was then required to allow events to be tracked as they evolve in frequency and also to allow a much wider range of single frequency events to be measured, vastly increasing the number of possible detections.

For this reason a new device needed to be developed to cover a much larger frequency band with similar sensitivity. The Michelson interferometer became the detection method of choice being a device that measures strain, with its orthogonal arms being perfectly suited to maximising signal size from the quadrupolar gravitational wave signal. Many years were then spent on developing techniques to increase the sensitivity of the Michelson interferometer which I will now briefly outline, describing the main subsystems of the interferometers currently being used. The frequency band covered by Michelson interferometers is currently around 10 Hz to 1 kHz and so is able to detect sources similar to those described in section 1.3.

2.2 Interferometry, Sensing and Control

The design of current gravitational wave detectors is centred around a traditional Michelson interferometer whereby the arm lengths are equal and complete destructive interference occurs at the beam splitter and there is no light detected at the output port. Differential motion of the end mirrors ideally caused by a gravitational wave passing through the interferometer in a direction perpendicular to the plane of the arms causes a change in the interference pattern measured at the dark port of the beam splitter.

There currently exists a worldwide network of detectors, GEO600 in Hannover, Germany, two LIGO detectors, one in Livingston, Louisiana and the other in Hanford, Washington and finally VIRGO near Pisa, Italy [10][11][12]. These detectors were built in the 1990s and have already completed taking data for several years at their design sensitivity. They are all now in the process of being upgraded to the advanced generation GEO-HF [13], Advanced LIGO [14] and Advanced VIRGO [15] and will all be an order of magnitude more sensitive. There is also a Japanese detector KAGRA [16] currently under construction in the Kamioka mine. The reason for the operation of many detectors is to allow better triangulation based on the timing difference in detections; it also allows for better sky coverage as each detector has a null point where a signal incident upon it at a certain angle can cause the same amount of motion on both of the end mirrors giving no differential motion and therefore no interference signal at the beam splitter.

(a) GEO 600

(b) LIGO Livingston

(c) LIGO Hanford

Figure 2.1: Aerial shots of the two LIGO detectors and the GEO detector (Images from the LIGO scientific community).

2.2.1 Fabry-Pérot Cavities

As can be seen from the images in Figure 2.1, the arm lengths of these detectors are very long, 600m in GEO and 4km in LIGO. The reason for this is that interferometers measure differential changes in arm length, or strain $\delta l/L$, so increasing L will make the detector more sensitive as explained in equation 1.11. There is still a limit based on technical challenges with making arm lengths too long. These include large beam spot sizes requiring very large mirrors, eventually the curvature of the earth and, of course, financial reasons of vacuum systems becoming more expensive.

A different method of increasing the phase effect in the arm is by bouncing

the light back and forth many times in a delay line [17], but this has quite a limited improvement as the effective length increase is only the number of reflections. The drawback of this method is that after a few round trips mirrors are required to be very large to accommodate all the separate reflections so factors of 10-20 are about all that can be done with this method. By collapsing these into a single reflection, Fabry-Pérot cavities are formed which do not require large mirrors and many more reflections take place, typically 1000's. Here the number of round trips each photon takes is set by the transmissive and reflective properties of the mirrors and is fully derived in section 3.1. This increases the effective length of the arm cavities by approximately the number of round trips.

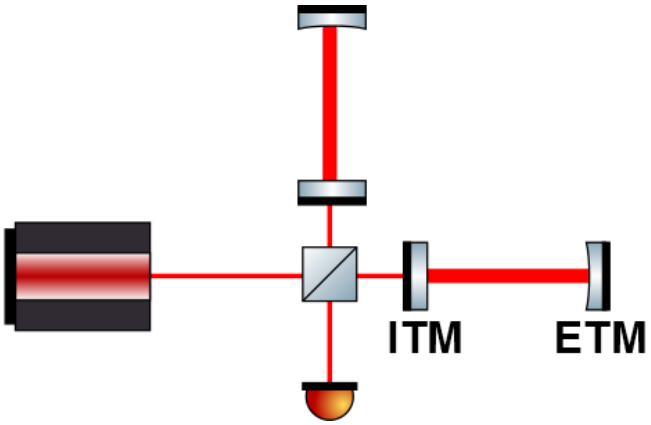

Figure 2.2: Michelson Interferometer with Fabry-Pérot arm cavities. The arms are usually described by points of compass, so in this case ITM and ETM North and East relative to the beam splitter.

As seen in Figure 2.2 a mirror called the input test mass (ITM) is inserted close to the beam splitter at one end of the arm and another, the end test mass(ETM), at the far end to create one of the Fabry-Pérot cavities which are at either end of the beam tubes shown in Figure 2.1.

2.2.2 Power and Signal Recycling

As mentioned previously the interferometer is set up to operate at the dark fringe, i.e. when both arm lengths are equal, and complete destructive interference occurs at the beam splitter. Under this condition all of the light is reflected back towards the input laser due to energy conservation and so the interferometer behaves as a mirror. It is possible to recycle this potentially wasted light by placing a mirror between the laser and beam splitter as shown in Figure 2.3, labeled PR for power recycling. This creates another cavity with the interferometer and if the mirror is correctly placed the field is resonantly enhanced back into the interferometer. This increase in power in the cavity arms means more photons sample the surface of each mirror, reducing photon counting errors and improving statistics. It also means that even a small signal will have more photons in it, making it easier to measure. However, as is always the way, this causes other problems due to thermal distortions and radiation pressure, caused by absorption of some of the high power beams which will be described in Section 5.0.1.

A similar approach can be taken with the output port. Although slightly counterintuitive, placing a mirror in front of a photodiode has the effect that when a signal is detected it is resonantly enhanced before reaching the photodiode [18]. By placing a mirror at the dark port as shown in Figure 2.3, another cavity is created with the interferometer which will resonantly enhance any signal at the output. This also allows tuning of the detector response to be more sensitive at some frequencies at the expense of others. This is done by tuning this cavity slightly off resonance or by altering the transmission of the mirror. A higher reflectivity means the signal will be resonantly enhanced for longer, creating a larger signal, however this also reduces the bandwidth of the signal recycling.

Broadband signal recycling is a technique whereby the signal recycling cavity is anti resonant with the carrier field. This increases the reflectivity of the ITMs at the carrier frequency from the perspective of any differential signals within the arm cavities. This means that signals remain within the cavity for longer, interacting with the gravitational wave longer, giving bigger signals but reducing the bandwidth. Although named broadband, this technique still has a narrow bandwidth only not as extreme as the detuned case already discussed. Another technique used is resonant sideband extraction [19], whereby the signal recycling cavity is resonant with the carrier field. In this case the signal remains in the arm cavities for a shorter time, thereby increasing the bandwidth but reducing signal size.

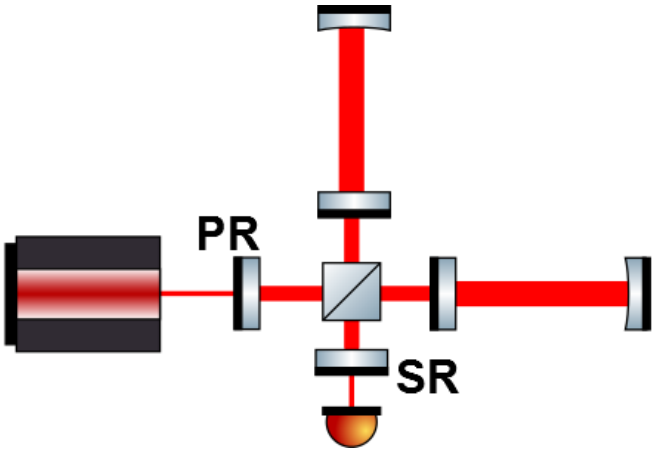

Figure 2.3: Michelson Interferometer with Fabry-Pérot arm cavities, power and signal recycling.

Advanced LIGO will be the first detector to use all three techniques, Fabry-Pérot arm cavities, power recycling and broadband signal recycling with the option to change to detuned at a later date. Initial LIGO used only Fabry-Pérot cavities and Power recycling, GEO used dual recycling but only folded arms.

2.2.3 Length Sensing and Control

The detector has now gone from a simple Michelson interferometer with laser, beam splitter, two mirrors and a photodiode to a complex system. This requires exact control of mirror positions relative to one another and many subsystems must operate in harmony. We will now go through some of the control requirements for these systems and how output signals are generated.

Each of these mirrors should be free to move from the effect of a gravitational wave, however remain in the working condition for the interferometer. This can be achieved by suspending the mirrors and other optics as the bottom stage of a pendulum. This has the effect of each behaving as a free mass above the pendulum resonance, and also isolates the mirrors from ground motion which will be discussed in more detail in Section 3.2.

Forces are then applied to the mirrors through wound coils and magnets for position and alignment control of the mirrors. This keeps the mirrors parallel to one another and also keeps the separation of the mirrors to a multiple of half the laser wavelength, which creates the resonant enhancement within the cavities. This is discussed in further detail in Section 4.3.

Often control signals are created using RF modulation and demodulation schemes. These require phase modulation sidebands to be imposed on the light entering the experiment. When propagated inside a cavity the phase of the carrier component moves relative to non-resonant sideband fields (which is directly reflected from the ITM), resulting in a change to the relative strength of the beat frequencies. Monitoring the fields exiting the cavity on photo detectors, and demodulating at the modulation/beat frequency, reveals an antisymmetric error signal. This length-sensitive signal can then be applied with suitable negative feedback through electromagnetic actuators to control the

cavity mirror positions. A mathematical explanation of this follows in Section 3.1.2.

Usually Michelson interferometers are operated at the dark fringe such that complete destructive interference occurs at the beam splitter. This helps to suppress common-mode noise and maximise the effect of power recycling, therefore maximising the signal to noise ratio. One technique to read out signals from the interferometer is heterodyne readout. Here, frequency separated sidebands are applied to the input light field and a small, static, differential arm-length change is applied to the interferometer, known as Schnupp asymmetry. This allows propagation of the sideband field once it has interacted with any gravitational wave signal to the output port where it can then be demodulated at the sideband frequency leaving the gravitational-wave signal. Another method, now more favored as the readout scheme for Advanced LIGO, is the DC readout, a form of homodyne detection. In this scheme the local oscillator is obtained by applying a slight offset to the arm length to allow a small amount of carrier field to propagate to the output port. This setup has the benefit of the carrier sharing the optical path with the sidebands, and so remains perfectly in phase, optimising demodulation. Further details on both detection principles can be found in [20].

2.3 Noise Sources

Trying to measure such small strains as $h = 10^{-21}$ creates interesting problems in suppressing all noise sources below this level. The noise sources in this instrument have been broken down into four parts: noise sources that create unwanted mirror motion, noise sources that act on the laser, noise sources that act on gravity, and noise sources that arise from the quantum nature of light

and matter. The first three of these noise sources have all required years of research and design to produce subsystems of the interferometer that enable us to reach the regime where instruments are expected to be limited by the fourth, quantum noise. These four noise sources will now be discussed as to where they arise from and the main subsystems developed to mitigate these problems.

2.3.1 Mirror Motion

One of the key aspects required for Michelson interferometers to work as gravitational wave detectors is that the mirrors used for measurements, i.e. the two cavity mirrors in each arm and the beam splitter, must behave as free masses in the detection band of interest. They must only move relative to one another due to a gravitational wave; any other movement of an amplitude greater than that of a gravitational wave is considered a noise and must be reduced below this level, as otherwise it would mask the gravitational wave signal.

The first type of mirror motion comes from ground motion coupling to the mirrors and requires the use of seismic isolation systems. There are several subsystems that do this, low frequencies are accounted for by using Hydraulic External Pre-Isolation (HEPI) and Internal Seismic Isolation (ISI). The main isolation in the detection band is achieved by suspending the optics as the bottom stage of a 4 level pendulum [21]. The pendulums ensure isolation in the 6 degrees of freedom and allow the mirror to behave as a free mass at frequencies that are large compared to their fundamental resonance frequency. The bottom stage of the four is connected to the stage above by 4 very thin (100 μm) silica fibres. These fibres must be of very high quality as they fully support the optic, which weighs 40 kg for reasons discussed in Section 5.0.1.

This gives very high Q suspension modes, typically around $10^4 - 10^7$. The mathematical description of suspension isolation is given in Section 3.2.

Figure 2.4: Quad suspension being prepared to be installed into advanced LIGO. red coloured object is the main mirror, coloured red due to being covered in protective film that is only removed at the last minute (Image from the LIGO scientific community).

The second type of mirror motion we shall consider is movements internal to the mirror itself. It consists mainly of thermal effects, causing both Brownian motion of the mirror surface but also internal mechanical modes. A high quality optic substrate is required to absorb as little of the high power beam as possible, typically $< 2\,\text{ppm}$. Absorption, even if on a small scale, given the extremely high circulating power (the reason for which will be discussed later), will also cause expansion, causing lensing of the optic and also changes of refractive index. This is countered through the use of ring heaters placed near the optic to heat the outside edge of the optic by the same amount,

negating the lens [22]. There also exist difficulties not only in achieving the very high reflectivities of 99.99 % required using multi-stack coatings, but also the smoothness of the final layer. The curvature and smoothness of optics is vital to ensure maintaining as much of the light in the resonant cavity mode as possible. The Advanced LIGO cavities are expected to have a round trip loss of only 75ppm.

2.3.2 Laser Motion

Although a laser mode is thought of as a single-frequency beam, the reality is that this single frequency changes over time due to fluctuations in the pump power and the laser crystal temperature changing. For the purposes of interferometry this is not usually considered a problem in a simple Michelson, as when the arm lengths are the same, changes in frequency do not matter as the light travels the same distance and destructive interference occurs at the beam splitter with light of the same frequency. However, when arm cavities, which can never be perfectly identical are used, this is no longer the case and it becomes much more important to keep the frequency constant. This is achieved in several ways, firstly the laser itself is very well designed with spectral linewidth of 1 kHz over 100 ms and relative power fluctuations of 2×10^{-9}. The input beam is also passed through mode cleaners which serve the dual purpose of further stabilising the frequency of the laser beam before it enters the interferometer and also of filtering out higher-order spatial modes caused from unwanted distortion in the input optics. The output field of the interferometer is also passed through a mode-cleaning cavity to remove noise caused by mirror imperfections and slight misalignments.

Nowadays the maximal obtainable laser power is no longer limited by the

available lasers, but by how much light power the system can handle without creating thermal lenses too strong due to the bulk absorption of materials being too high. With as little as 1 ppm absorption given the very high cicrculating powers in the arm cavities of 100s kw it is easily possible to heat the optics. For this reason Laguerre-Gauss(LG) modes were suggested for use in future detectors, the reason being the intensity profile of the beam is more spread out. This has many benefits, including thermal lenses being less strong, and sampling a larger area of the mirror, reducing the effect of coating Brownian motion. The first experiment of injecting an LG33 beam into a suspended cavity was conducted at Glasgow with the results setting new requirements on mirror surface quality to be achieved before using these types of beams will become a viable option [23].

2.3.3 Gravity Motion

Caused by local changes in the gravitational field, direct coupling of mass density fluctuations to the mirrors can exist, for example, seismically driven density fluctuations of the ground surrounding the mirrors, clouds passing overhead, tidal changes, vehicles moving nearby. As with all gravitational interactions the masses need to be large or close by to have an appreciable effect. However, it is very difficult to measure and model these effects as they are generally not constant or predictable. For this reason very little can be done and as such this sets the lower frequency sensitivity of ground based detectors.

Some investigation is being made into ways of possibly using seismometer arrays and feed-forward actuation onto the mirror, but this technology is not ready for integration into detectors. Other suggestions of large trenches around

the detector sites have been put forward as the most common way for gravity wave fluctuations to disperse are as earth surface ripples. Realistically the best option is to choose a seismically quiet, remote site, which is not feasible for current detectors but an important consideration for any future detectors that are to be built[24].

2.3.4 Quantum Motion

With other noise sources currently at such a low level, the quantum nature of the light is now going to be one of the future major limiting noise sources for interferometric detectors. This arises from the Heisenberg uncertainty principle applied to continuously measuring the position of a free mass, in this case the four cavity mirrors. This will be explained in more detail in Section 5.0.1.

Quantum noise consists of two parts: amplitude and phase noise, the two separate quadratures which correspond to a photon-counting error, shot noise and radiation pressure noise, amplitude noise. The shot noise of the light affects the higher frequency and radiation pressure affects at lower frequency. Generally increasing the light power is what we want to do as it is one of the few ways to increase potential signal size whilst reducing photon counting error. More light power means more photons seeing the effect of the gravitational wave. This of course has the effect due to more photons hitting the mirror of more error in the radiation pressure force caused by the change of momentum of individual photons. One way to counter this is to increase the mass of the mirrors as this will reduce the effect the force has on its displacement.

The current method of suppressing this noise source is by using a technique called squeezing [25]. The idea here is that light is input to the system through the output port of the beam splitter in a squeezed state. A squeezed state

changes the property of the light such that the important phase information noise is improved at the expense of intensity information. So far the best test in large-scale interferometers have demonstrated a squeezing level of 3dB. This is limited by loss in the injection paths of the squeezed light [26]. In future an observed squeezing level of 6dB will be targeted.

Figure 2.5 shows a simulation of all the noise sources important in advanced LIGO and the expected achievable strain sensitivity as the total sum of all of these. The plot was produced in GWIC, a programme written by the gravitational wave community to allow quick noise simulations to be carried out by tweaking different system parameters and different detector layouts.

2.4 Upgrades

As the advanced generation of detectors are commissioned and begin to take data, the limiting noise source across the majority of the detection band, 10 Hz to 1 kHz, will be quantum noise. Further upgrades will require this limit to be beaten or at least altered to allow measurements beyond this point. The other noise source that is close to limiting advanced designs is likely to be the thermal noise of the reflective coating of the mirrors. A lot of research is currently underway to design new coatings or types of reflector that could be used instead [27]. The point has now been reached where any increase in sensitivity is very important as even a factor of two improvement corresponds to a factor 8 in volume of sources that may now be detected.

Quantum non-demolition (QND) techniques is the name coined for topologies that could theoretically surpass quantum noise limited sensitivities and will be discussed in further detail in Section 5.0.3. Such techniques include the

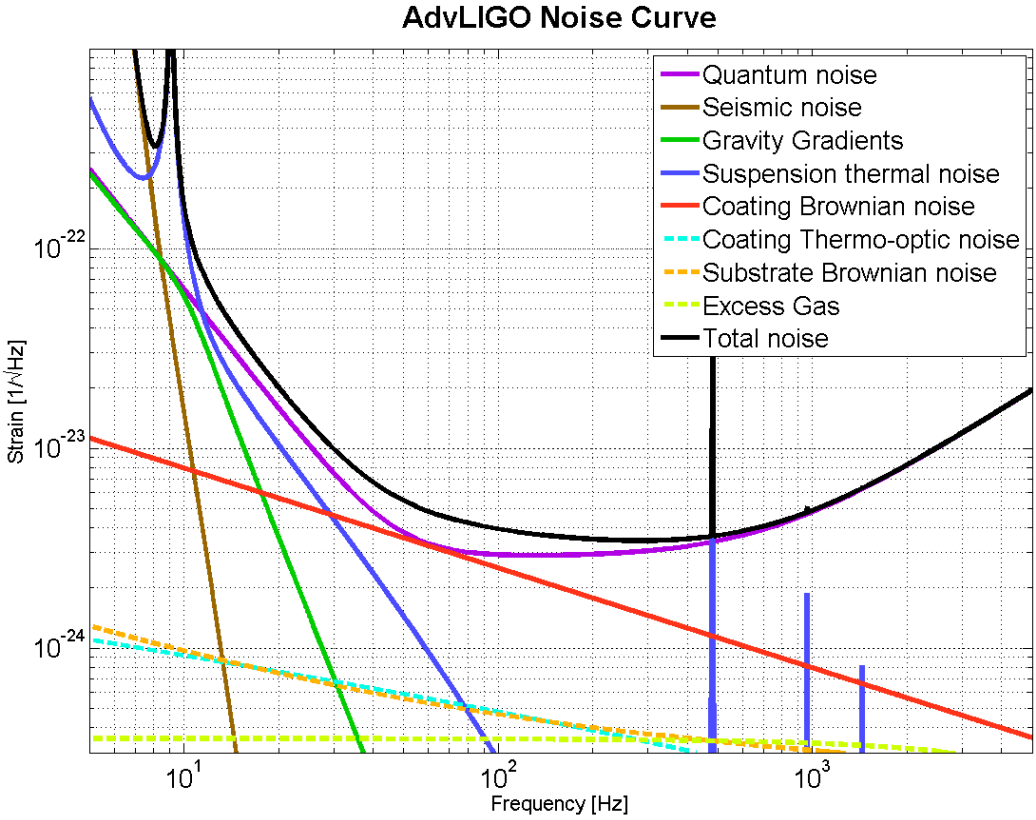

Figure 2.5: Predicted noise curves for advanced LIGO, a factor 10 improvement over initial LIGO across all frequencies. Suspension thermal noise and seismic noise are limiting at low frequency and quantum noise in the rest of the frequency band. Coating thermal noise is also close around 60Hz. Curves produced using GWIC, software written by LIGO community to simulate noise performance in various detector configurations and detector properties.

optical bar topology which will constitute a large portion of Chapter 5 of this thesis.

Other ideas include switching to speed meters. These devices use a different interferometric topology, namely, the Sagnac interferometer which can be arranged such that the output contains information about the speed of test masses and not the mirror position. Speed does commute with time and as such can in theory be measured to arbitrary accuracy without being limited by the Heisenberg uncertainty principle. This technology is currently far from detector ready and a proof of principle experiment is currently being built in the Glasgow 10 m prototype [28].

This section has concentrated on techniques for upgrades within current infrastructure at relatively small cost. Plans are currently underway at developing a third generation of detector to achieve another factor 10 improvement in sensitivity. This has been called the Einstein Telescope or ET project. This would be a completely new-build detector which is currently in the early design stages [29]. It is likely to be underground in a seismically quiet area and employ higher laser power, heavier mirror masses, taller suspensions and it will also be configured in some type of QND setup such as an optical bar.

2.5 Other Types of Detector

For various different types of supernova or rotating neutron star much smaller or larger masses or different astronomical events altogether, signals can occur at many different frequencies and could easily be created from nHz up to MHz. For this reason several other projects exist for detecting gravitational waves over different frequency bands. In the scope of this thesis only interferometric

ground-based detectors will be discussed, but for, completeness other types of detectors will now be briefly summarised.

The Laser interferometric space antenna (eLISA) [30][1] is a planned space-based project that uses interferometry in a similar way to ground-based detectors. The main difference is that this device will be sensitive to signals in the mHz regime due to low frequency noise sources not being as prominent in space. Space and vacuum constrictions are not as great in space and so the arm lengths will be of the order several million kilometres apart with test masses located on separate spacecraft, so keeping these aligned brings its own set of challenges. LISA pathfinder [31] is a project to test the technologies in a space mission and is estimated to be launched in 2015. If this is successful, the full eLISA detector could be launched by 2030. DECIGO, the Deci-Hertz interferometric gravitational wave observatory, is another space-based project which, as the name suggests, is most sensitive to signals in the frequency band 0.1 Hz to 10 Hz, filling the gap between LIGO and eLISA.

At very low frequencies, nHz, pulsar timing arrays such as the Square Kilometre Array (SKA) monitor the very repeatable electromagnetic waves emitted from pulsars. By using many detectors, very small changes in the frequency of observation of the pulses can be used to calculate the effective stretching or shrinking of space time caused by gravitational waves.

[1] eLISA, formerly refereed to as LISA (Laser Interferometer Space Antenna), was renamed eLISA after NASA withdrew funding in 2012 and the project was taken over by the European Space Agency and so became known as the European Laser Interferometer Space Antenna.

Chapter 3

Optical Rigidity

With the need for ever increasing optical power to be stored within the interferometer, radiation pressure caused by the exchange of momentum from photons to the optics can become a non-negligible noise source. The interaction between radiation pressure effects and suspended optics is well known but has rarely been investigated in the regime where the cavity response is anything but flat. In this chapter I will describe numerically the field equations for a single cavity, and subsequently the radiation pressure force. We will then look at the mechanical response of a suspended optic and how light interacts with mirrors in a suspended cavity. Finally we will show the coupling effect between radiation pressure and the pendulum restoring force, known as the optical spring.

3.1 Cavity Dynamics-Optical

An optical cavity forms a crucial part of gravitational wave detectors and is fundamental to many other optics applications. It is made up of two partially reflective mirrors facing one another with a light beam incident on the back surface of one. As the mirrors are also partially transmissive, some of this field leaks through the mirror and then circulates between both mirrors before leaking through one of the two mirrors. Dependant on reflectivity and transmissivity of the mirrors, the field can build up between the mirrors as photons take many round trips before leaking out again. The following section details how the fields propagate through an optical cavity.

3.1.1 Field Equations and Power Coupling

We now examine how the electromagnetic field propagates through an optical cavity[1]. To start with we shall look at the basic case of the transformation matrix applied to a light beam by a mirror or how a light field interacts with a partially transmissive mirror with reflectivity ρ and transmission τ.

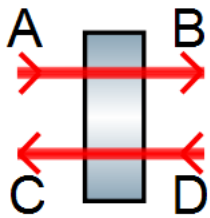

Figure 3.1: Field amplitude interactions at a mirror. A simple schematic of input beams A and D and output beams B and C for a simple mirror.

[1] This section will ignore scatter and absorption effects.

$$\begin{pmatrix} E_b \\ E_c \end{pmatrix} = \begin{pmatrix} i\tau & \rho \\ \rho & i\tau \end{pmatrix} \cdot \begin{pmatrix} E_a \\ E_d \end{pmatrix} \tag{3.1}$$

If we have an input field

$$E_i = E_o e^{i\omega t}, \tag{3.2}$$

the transformation matrix can be applied to it to obtain the transmitted and reflected fields of a mirror as follows:

$$\begin{aligned} E_b &= i\tau E_a(t) + \rho E_d, \\ E_c &= \rho E_a(t) + i\tau E_d. \end{aligned} \tag{3.3}$$

By creating a two-mirror cavity, the propagation of the field changes and the fields throughout the system can be calculated in the same way as above. The

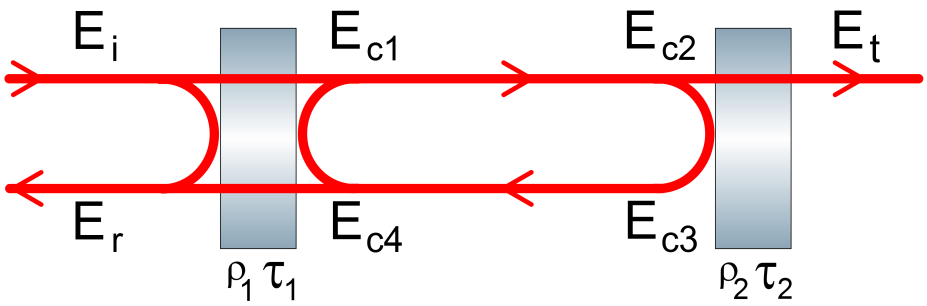

Figure 3.2: Field amplitude interactions with a two-mirror cavity with input beam E_i, reflected beam E_r, transmitted beam E_t and intracavity fields E_{c1},E_{c2},E_{c3} and E_{c4}

intracavity fields can then be described as:

$$\begin{aligned} E_{c1}(t) &= \tau_1 E_i(t) + \rho_1 E_{c4}(t), \\ E_{c2}(t) &= E_{c1}(t + c/L), \\ E_{c3}(t) &= \rho_2 E_{c2}(t), \\ E_{c4}(t) &= E_{c3}(t + c/L), \end{aligned} \tag{3.4}$$

where the fields E_{c2} and E_{c4} are simply phase changes of E_{c1} and E_{c3} respectively due to propagating the length of the cavity. The important fields are those transmitted and reflected from the cavity as they can be measured without affecting the state of the system and are as follows,

$$\begin{aligned} E_t(t) &= \tau_2 E_{c2}(t), \\ E_r(t) &= \tau_1 E_{c4}(t) + \rho_1 E_i(t). \end{aligned} \tag{3.5}$$

For the static case and constant amplitude input light field the intracavity field is

$$E_{c1} = A\tau_1 + E_{c1}\rho_1\rho_2 e^{-2i\theta}, \tag{3.6}$$

which can be solved to give

$$E_{c1} = \frac{A\tau_1}{1 - \rho_1\rho_2 e^{-2i\theta}}. \tag{3.7}$$

The reflected field is then

$$E_r = A\rho_{12}, \tag{3.8}$$

where

$$\rho_{12} = \rho_1 - \frac{\tau_1^2\rho_2 e^{-2i\theta}}{1 - \rho 1\rho 2 e^{-2i\theta}}. \tag{3.9}$$

We have therefore shown that the reflectivity of a static Fabry-Pérot cavity is a function of the detuning phase, or how close the cavity length is to a whole number of half wavelengths, and can be used effectively as a mirror with variable reflectivity for monochromatic light as experimentally demonstrated on an earlier Glasgow prototype [32].

Analogous to the above, we can express the transmitted field as

$$E_t = E_{c1}\tau_2 e^{-i\theta}, \tag{3.10}$$

$$E_t = \frac{A\tau_1\tau_2 e^{(-i\theta)}}{1 - \rho_1\rho_2 e^{-2i\theta}}. \tag{3.11}$$

Hence, the transmitted field is directly proportional to the intracavity field and is often used to determine the stored power inside a cavity.

If the distance between the mirrors and the frequency of the laser are arranged so that the light entering the cavity is in phase with the light already inside the cavity, then the intracavity field is resonantly enhanced. The maximum amplitude of the cavity field occurs when the term $e^{-2i\theta} = 1$. In this situation the maximum amplitude gain of the cavity is

$$g_{12} = \frac{\tau_1}{(1 - \rho_1\rho_2)}. \tag{3.12}$$

We now consider the power inside the cavity if the cavity is not exactly a whole number of half wavelengths in length which is given by

$$P = P_{in} g_{12} \frac{1}{1 + \mathcal{F}\sin^2\theta}. \tag{3.13}$$

This was calculated in [33] where θ is the detuning in terms of degrees from resonance where $\lambda_{las}/2 = 180^o$ and $\mathcal{F}$ is the finesse. This is a measure of how quickly the power in the cavity falls off as it is detuned and is dependent on the reflectivities of the cavity mirrors as follows:

$$\mathcal{F} = \frac{4\rho_1\rho_2}{(1 - \rho_1\rho_2)^2}. \tag{3.14}$$

The free spectral range (FSR) of a cavity is the frequency separation between successive resonances. It can also be thought of as one over the time it takes the light to complete one round trip of the cavity and is defined by

$$FSR = \frac{c}{2L}, \tag{3.15}$$

where L is the the cavity length.

One of the most useful equations in interferometry is relating changes in frequency to changes in length. By starting of with a resonant cavity the total

cavity length must equal a whole number of half wavelengths on resonance, Gouy phase affects have been omitted here for simplicity.

$$N\frac{\lambda_{las}}{2} = L_{cav} \tag{3.16}$$

substituting

$$c = f_{las}\lambda_{las} \tag{3.17}$$

gives

$$\frac{Nc}{2} = f_{las}L_{cav}. \tag{3.18}$$

The above has to be true for any given resonance and so the fractional change in length $\Delta\ell$ must equal the fractional change in frequency Δf,

$$\frac{\Delta\ell}{L} = \frac{\Delta f}{f_{las}}. \tag{3.19}$$

The finesse ($\mathcal{F}$), can also be described by the ratio of the FSR to the width of the resonance peak, which is called the cavity linewidth γ, and is the HWHM of the resonance peak as a function of detuning and can therefore be described in frequency or length.

$$\mathcal{F} = \frac{FSR}{2\gamma}. \tag{3.20}$$

An optical cavity can exhibit very different behaviour based on the mirror parameters. The different levels of transmission determine whether a cavity is over-coupled ($\tau_1 > \tau_2$) or under-coupled ($\tau_1 < \tau_2$) or impedance-matched ($\tau_1 = \tau_2$). This determines whether more light is reflected from or transmitted through the cavity. For the purpose of the experimental setup used we deal with an overcoupled cavity due to its similarity to an interferometer whereby having more light reflected back to the beam splitter will improve signal contrast. For further detail and the derivations of this see [34].

The curvature of the mirrors will affect the beam size on each mirror, the shape of beam inside the cavity and also the cavity stability. The beam size

is important for GW detectors as we wish to make it as large as possible to reduce thermal noise. As the beam size increases on the cavity mirrors, the cavity stability decreases.

As the cavity will only resonate at certain frequencies it acts as a very good filter as only one spatial mode order can be resonant at any one time. This proves useful as cavities can be used to filter laser beams to only allow propagation of a single mode. This technique is used in gravitational wave detectors to filter both the input and output beams of the detector [34].

The cavity also behaves as a filter in the sense that higher frequency signals are suppressed. As the storage time of the cavity increases (higher reflectivity cavity mirrors), photons stay in the cavity longer and as such high frequency effects are lost. The same effect also occurs due to the time it takes a photon to travel the length of the cavity. A cavity therefore behaves as a first-order low-pass filter, where the corner is at the cavity linewidth frequency [34].

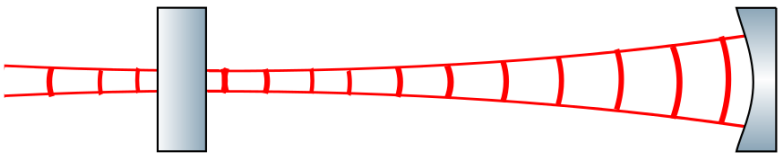

Figure 3.3: Single spatial mode matched to cavity whereby the phase front matched the radius of curvatures of each mirror. The topology is the same as that implemented in experiments discussed in this thesis, consisting of a plane input mirror and curved end mirror.

3.1.2 Modulation and Demodulation

To be able to control optical cavities and more complex interferometers it is necessary to modulate the light beam as mentioned in Section 2.2.3. By adding

sideband fields to the beam, the interaction with the cavity changes from the expressions described previously as there are now different components to the beam. These can be broken down into separate carrier and sideband fields with different relative frequencies, meaning only one can resonate in the cavity at any time. We can see in Figure 3.4 that as the cavity length is changed, the carrier, sideband and higher-order sideband fields resonate at different points.

We begin by showing how the amplitude modulation interacts with the light field. The carrier field is simply

$$E = E_0 e^{i\omega_0 t}. \tag{3.21}$$

When the carrier field is amplitude modulated, this becomes

$$E_{AM} = E_0 e^{i\omega_0 t}(1 + m\cos(\omega_m t)), \tag{3.22}$$

where m is the modulation index and ω_m the angular frequency of modulation.

We now look at the mathematics of applying phase sidebands to the carrier field.

$$E_{PM} = E_0 e^{i\omega_0 t} e^{im\cos(\omega_m t))} \tag{3.23}$$

which is different to the amplitude case as it now contains a periodic phase term $e^{im\cos(\omega_m t)}$. Expanding this with standard identities gives

$$E_0 e^{i\omega_0 t} \sum_{k=-\infty}^{\infty} i^k J_k(m) e^{ik\omega_m t}, \tag{3.24}$$

$$\approx E_0 e^{i\omega_0 t}(J_0(m) + iJ_1(m)e^{i\omega_m t} + iJ_1(m)e^{-i\omega_m t}). \tag{3.25}$$

Here $J_k(m)$ are Bessel functions of the first kind of order k.

Photodiodes used to detect these fields output a signal proportional to the power incident upon them. The output signal is obtained by multiplying the

field with its complex conjugate. For an unmodulated beam this simply gives the power, however, for a phase modulated beam it gives

$$P_{det} = P_{\omega_0} + P_{\omega_m} + P_{2\omega_m}, \tag{3.26}$$

where the ω_m terms are zero unless there is a phase change between carrier and sideband field e.g. when interacting with a cavity. As we are only interested in the ω_m we beat the whole signal P_{det} with a ω_m local oscillator. This gives a signal at DC with information about the beat between carrier and sideband which we are able to maximise by tuning the phase of the local oscillator. This gives bi-polar length-sensitive signal which allows negative feedback to be applied to actuators to control the cavity length. It is important to see that when the carrier field resonates in the cavity the sideband fields are reflected off the ITM and do not interact with the cavity. So the reflected carrier field that has interacted with the cavity mixes with the reflected sideband field. When the detected field is demodulated at the sideband frequency it gives a bi-polar signal with a zero crossing at the peak of the resonance. This technique used to readout cavity length changes is called the Pound Drever Hall method [35] and is commonly used for control of optical cavities.

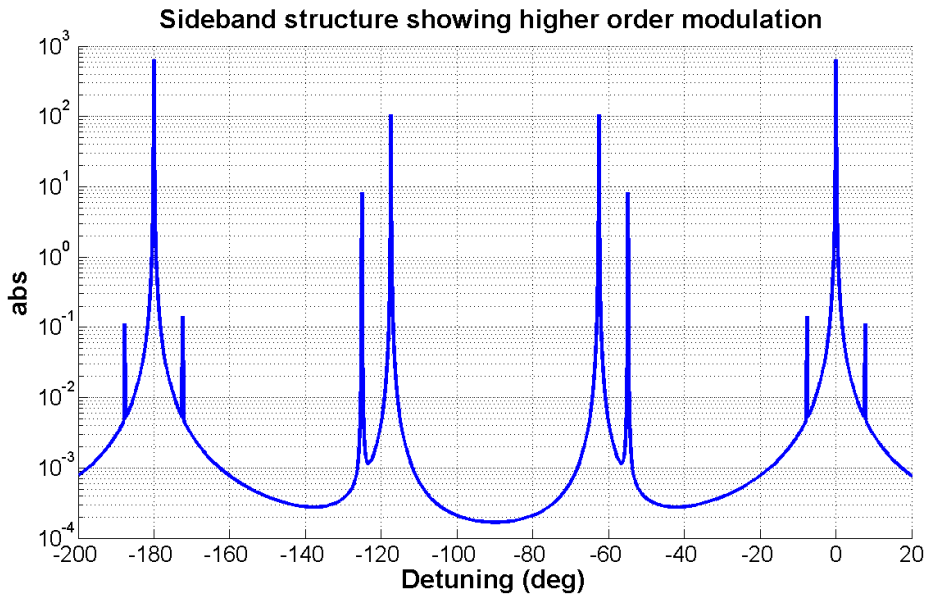

Figure 3.4: Simulation of the free spectral range of a cavity shown on logarithmic scale to illustrate the sideband structure. The inset shows the resonant Airy peak. Multiple sideband terms are applied to the light if the expansion is done completely at multiples of f_{mod}.

3.2 Cavity Dynamics-Mechanical

As previously mentioned it is important that both cavity mirrors are isolated from ground motion. One way of achieving this would be to float the mirrors using magnets. However, this is very difficult to do in a controlled manner. A much easier and more developed method is to suspend them as the bottom stage of a pendulum. The basic dynamics of pendulums and how isolation is provided will now be discussed.

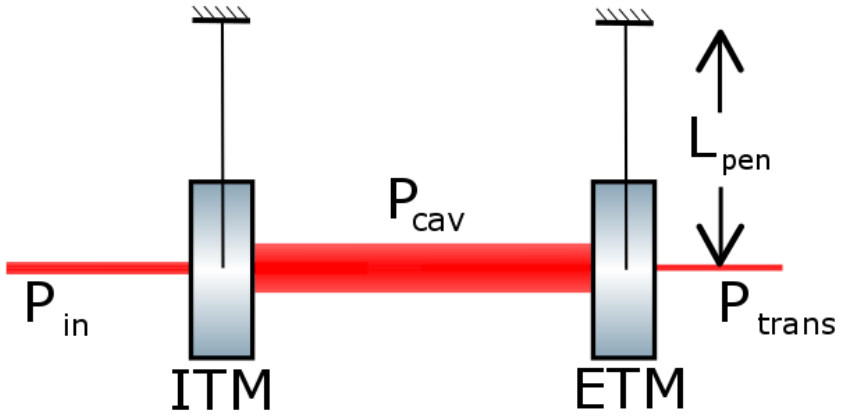

Figure 3.5: Cavity mirrors suspended as the bottom stage of a pendulum of length L_{pen}. A photograph of a suspended mirror is shown in Figure 4.7.

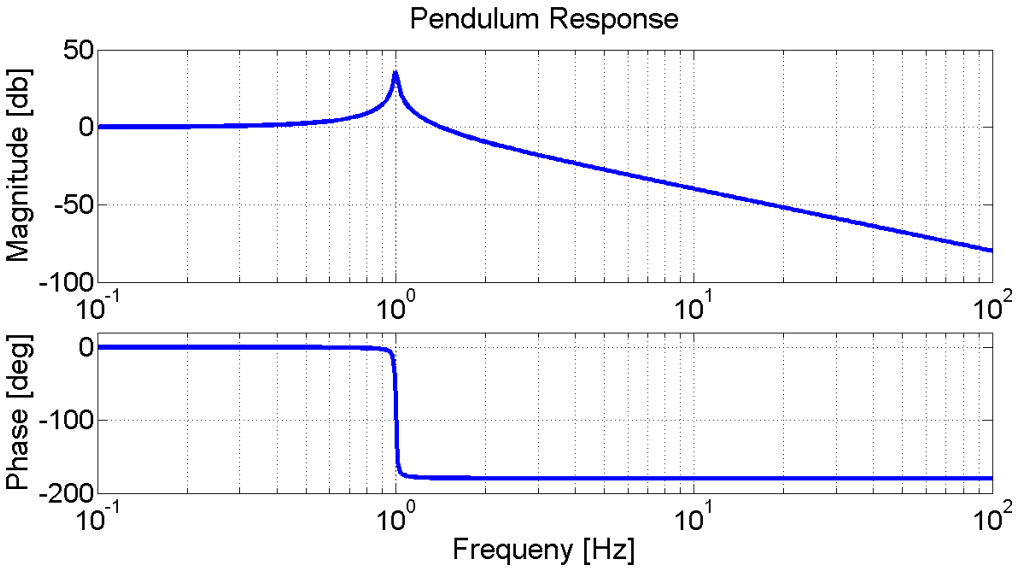

Figure 3.6: Frequency response of a simple pendulum. Length = 0.25 m giving resonance at 1 Hz.

Figure 3.6 shows the frequency response of a simple pendulum in terms of motion transferred from the suspension point to the suspended object. It is a model of a pendulum of length 0.25 m, giving a resonance at 1 Hz with a Q of the resonance of 100. The Q value sets the bandwidth of the reso-

nance, which, for the purpose of optics suspensions, we wish to make as large as possible, therefore keeping the frequency it affects very small. Above the resonance there is a drop-off in response of the form $1/f^2$, meaning at high frequencies almost no signal is transferred from the suspension point to the object being suspended. This makes it perfectly suited to work as a higher frequency isolation system for optics in gravitational wave detectors. By reducing the fundamental frequency as low as possible, the drop-off starts at lower frequency, increasing the magnitude of high frequency isolation. This isolation can be further improved by cascading pendulums, suspending one from the bottom stage of another. The $1/f^2$ then becomes $1/f^4$, improving the isolation dramatically at higher frequencies.

3.3 Radiation Pressure

Gravitational-wave-detector cavities now use very high circulating powers to reduce shot noise and increase signal size. The downside of this is that reflected photons impart momentum onto the mirror, which at high power levels can dominate the suspended-mirror dynamics. The radiation pressure force exerted on an optic is proportional to the light-field power and the reflectivity of the surface. The radiation pressure force is then (change in momentum)/time = $2m_{\text{eff}}c/t = 2hf/ct$, where $t = E_{\text{photon}}/P$, i.e.,

$$F_{RP} = \frac{(2hf/c)}{(hf/P)} = \frac{2P}{c} \tag{3.27}$$

assuming all the photons are reflected. The force exerted on the mirror by a fully reflected 1 W beam is then 6.69×10^{-9} N.

3.4 Radiation-Pressure-Dominated Dynamics of a Suspended Cavity

As most of the cavities dealt with in the field of gravitational wave detection are suspended for reasons already mentioned, large radiation pressure forces acting along the beam axis can cause an acceleration of the mirror from its equilibrium position, which in turn is then balanced by the restoring force of the pendulum. The dynamics of this will now be described.

The cavity no longer being static makes the cavity properties slightly harder to measure. The finesse of the cavity can not simply be measured by comparing the FSR to the resonance linewidth. This is an effect of using high-quality mirrors such as those used in the experiments to follow in Chapters 5 and 6. This gives rise to a very high finesse of >10000, i.e. more power stored in the cavity, and so the linewidth is very narrow compared to the FSR. What is seen experimentally as the mirrors swing and the cavity passes through a resonance is that the light power rings with an exponential decay as shown in Figure 3.7. This is caused by the longer storage time of the cavity. So, as the mirrors pass through a resonance, the power builds up to maximum almost instantaneously. Due to the higher finesse the storage time in the arm cavities is very long and so light is still stored in the cavity long after the mirror has moved away from resonance. At this point the decaying cavity field is reflecting back and beating with the now out of phase input beam. This causes the decaying exponential ringdown as seen in Figure 3.7.

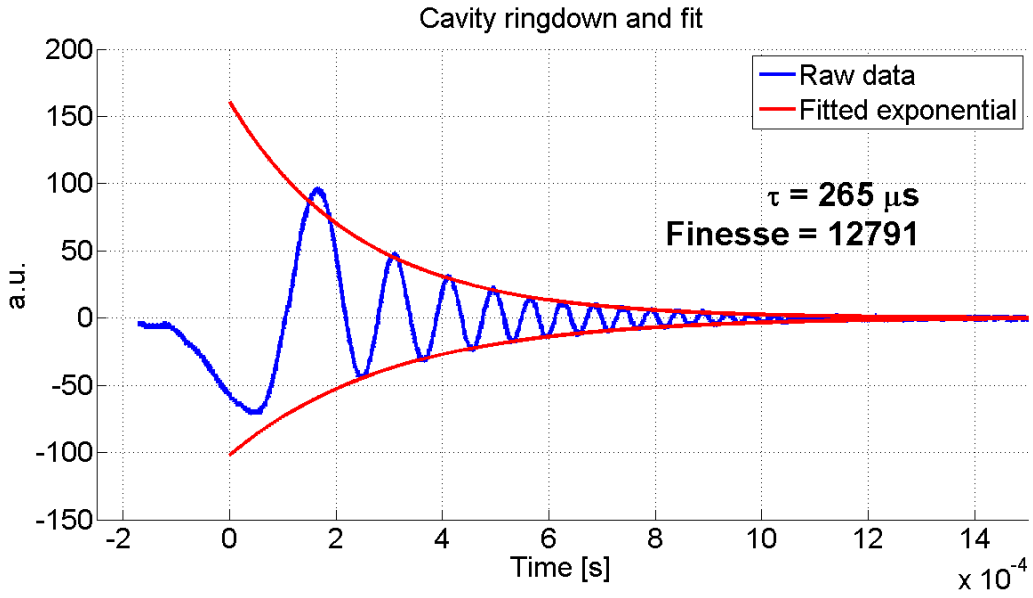

Figure 3.7: The plot shows voltage from a photodiode measuring reflected field as the cavity is unlocked with a small longitudinal drive signal applied to the ITM. The D.C. offset was removed to make the fitting of the exponential decays easier. The final decay gave a measured finesse of 13000, which gives a linewidth of 578 Hz for the cavity used in the experiments discussed later in this thesis.

From this the finesse of the cavity can then be calculated. This is achieved first by fitting an exponential envelope to the ringing decay giving the two curves shown in red in Figure 3.7. The difference of these is ten taken to remove slow drifts in the signal giving a final exponential decay with decay constant τ. The FWHM is then given by $\pi\tau$ and from this the finesse can then be calculated using equation 3.20.

Using figure 3.7 it is also possible to calculate the velocity of the mirror by measuring the time between peak and trough of an oscillation. If the non-resonant field is static and the cavity field is changing due to the mirror motion the 180 degree of phase or half a wavelength must correspond to the difference

between the peak and trough. This gives a value of 0.017 m/sec. The size of this value is explained as during the measurement the ITM was being driven longitudinally. By driving the mirror this moved the fringe through resonance much quicker meaning the decay was only due to the field leaking out of the cavity.

3.4.1 Optical Rigidity

Cavities are usually kept on resonance in one of two ways, either by changing the laser frequency to follow the cavity-length changes or by actuating on one of the mirrors' position to keep the separation constant. As one offsets the locking point to the side of the resonance peak, usually achieved by adding a static offset voltage to one of the feedback mechanisms, the intracavity power will drop and so the radiation pressure force will also drop. At this point a change in mirror position in one direction will increase the radiation pressure force due to moving closer to the cavity resonance and reduce the radiation pressure force by moving away from the cavity resonance in the other direction. The mirror motion also experiences another force when moving due to the pendulum restoring force, shown in figure 3.8, which will increase as the mirror moves away from its equilibrium and decrease as it moves closer to equilibrium.

On one side of the resonance curve a displacement will cause either an increase or decrease in the radiation pressure. On the opposite side of the resonance the same movement would have the opposite effect on radiation pressure due to the slope having the opposite gradient. On one side the radiation pressure force will act to oppose the restoring force (stable) and on the opposite it will act in the same direction (unstable). The stable configuration is known as an

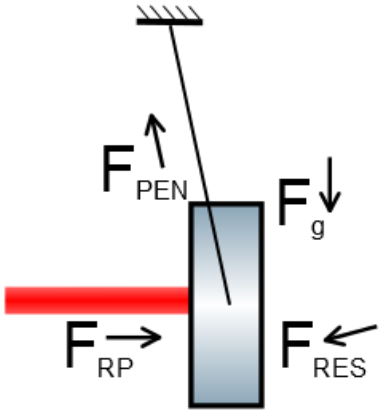

Figure 3.8: Balancing of forces between radiation pressure and pendulum restoring force.

optical spring, the unstable configuration as an anti-spring.

The optical spring behaves like a mechanical spring connecting both cavity mirrors using only photons, and therefore in contrast to a mechanical spring provides a spring without thermal noise. It behaves as any harmonic oscillator with associated, Q values and an effective Young's modulus, assuming the laser beam is a bar of width equal to the $1/e^2$ value of the beam radius at the mirror surface.

The mathematical derivation of the optical spring will now be discussed. We begin with a standard spring response,

$$\begin{aligned} F_{restoring} = -k_{os}x &= \frac{md^2x}{dt^2} \\ \frac{d^2x}{dt^2} + \frac{-k}{m}x &= 0. \end{aligned} \tag{3.28}$$

The optical spring constant k_{os} can be calculated by relating the radiation pressure force to the pendulum restoring force, both as a function of detuning. The further the system is detuned from resonance, the lower the radiation

pressure force but the higher the pendulum restoring force.

Total restoring force = pendulum restoring force + radiation pressure force

$$dF = \underbrace{-m\omega_{pen}^2}_{k_{pen}} dx + \underbrace{\frac{2P(dx)}{c}}_{k_{os}} dx \tag{3.29}$$

$$P(dx) = \frac{\partial P(\theta)}{\partial \theta}\frac{\partial \theta}{\partial x} \tag{3.30}$$

Using the small-angle approximation for $\sin\theta = \theta$ and substituting Equation 3.13 we get

$$\frac{\partial P(\theta)}{\partial \theta} = 2P_{in}\frac{\mathcal{F}\theta}{(1+\mathcal{F}\theta^2)^2} \tag{3.31}$$

and

$$\frac{\partial \theta}{\partial x} = \frac{2\pi}{\lambda} \tag{3.32}$$

$$\Rightarrow k_{os} = \frac{8\pi P_{in}\mathcal{F}\theta}{c\lambda(1+\mathcal{F}\theta^2)^2} \tag{3.33}$$

As expected the above expression is dependent on the shape of Airy peak, the finesse $\mathcal{F}$, the amount of detuning θ, and the amount of input power to the cavity P_{in}. The associated resonance frequency ω_{os} in radians or f_{os} in Hz can then be calculated using the reduced mass of the system m_{red} as follows:

$$\omega_{os} = \sqrt{\frac{k_{os}}{m_{red}}}. \tag{3.34}$$

The equations described above only hold true in the case in which the cavity response can be considered instant, i.e. for $f_{os} \ll \gamma$. We will now go on to describe the optical rigidity effects when this is not true and the cavity response has a large effect. The result of the cavity pole is that the optical spring force on the mirror does not respond instantaneously to a change of cavity

length. Khalili and Vyatchanin first showed this effect [36] and described it as follows:

$$k_{os}(\Omega) = -\frac{2i\omega_0^2 P_{in}}{cL}\left(\frac{1}{\ell(\Omega) - \frac{1}{\ell^*(-\Omega)}}\right), \tag{3.35}$$

where $k_{os}(\Omega)$ is the frequency-dependent spring constant. Mirror motion at Ω causes phase modulation of the carrier light with sidebands at $\omega_0 \pm \Omega$. The $\ell(\Omega)$ places poles in $K(\Omega)$ at sideband frequencies $\gamma \pm \delta$ which upon simplification gives

$$k_{os}(\Omega) = k_{os}\frac{1+\delta_\gamma^2}{(1+\imath\Omega\gamma)^2+\delta_\gamma^2}, \tag{3.36}$$

where k_{os} is the same as Equation 3.33 and δ_γ is the detuning in Hz as a fraction of the linewidth. The real part of $k_{os}(\Omega)$ then gives the frequency-dependent spring constant and the imaginary part gives the viscous damping term plotted in Figure 3.9 and Figure 3.10 respectively. We also see that as γ becomes large compared to Ω (that is to say the linewidth of the cavity is much larger than the mirror-motion frequency or the cavity response is instant compared the the measurement frequency) this term disappears and we are left with k_{os}.

It can be seen in Figure 3.10 that the points of positive spring constants coincide with a negative viscous-damping term and vice versa. This shows that optical springs are inherently unstable and that is why feedback servos are required to keep the system in its operating state.

Optical springs have been studied across a broad mass range from ng [37] up to the g scale [38], but only recently at the 100g scale, using a previous incarnation of the experiments discussed in this thesis. The experiments referenced above all took place far away from the regime whereby the optical spring is affected by the cavity pole and so making this a very interesting setup to work with.

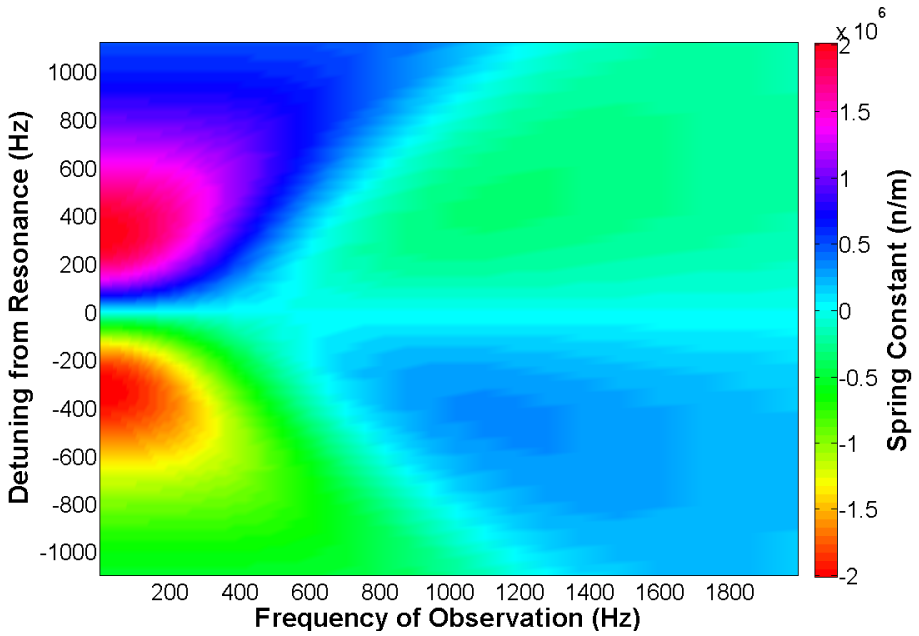

Figure 3.9: Plot showing frequency dependence of the optical spring constant on detuning. The parameters used in this simulation are for the ones used in the experiments of this thesis. The same applies for Figure 3.10.

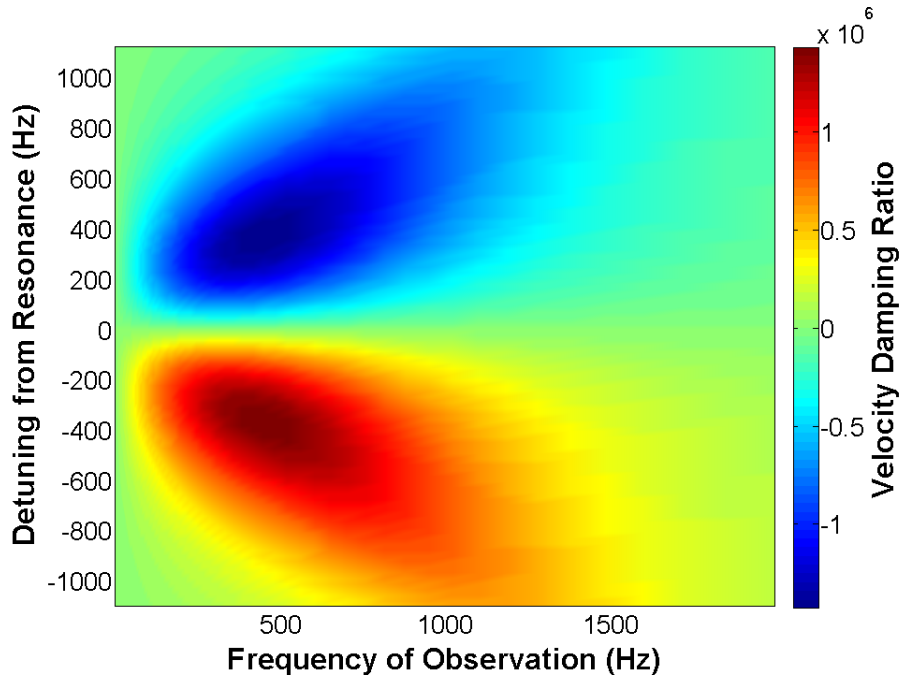

Figure 3.10: Frequency dependence of velocity damping on detuning.

3.4.2 Parametric Instabilities

Parametric instabilities can occur in radiation-pressure-dominated systems and are caused by mechanical modes of the mirror substrate pushing light power from the main carrier mode into sideband fields, which can further excite mechanical modes causing the so called parametric instability [39]. This phenomenon is only mentioned for completeness as it is common among many other optical-spring experiments due to the large radiation-pressure effects required to create optical springs. They do not affect our system for the following reasons. The linewidth of the cavity used is very low, 570 Hz, meaning there are very few photons in the cavity at the much higher-frequency mechanical modes of the mirror substrate which are typically 10s kHz. It should also be noted that parametric instabilities can occur in non-suspended cavities and have nothing to do with optical springs. They are only prominent in this field due to the large radiation pressure forces and lighter masses used.

Chapter 4

Experimental Apparatus and Design

The following chapter describes the experimental setup common to all of the experiments discussed in this thesis. The experiments are both centered around a high-finesse, suspended, 10 m Fabry-Pérot cavity whose dynamics are dominated by the radiation pressure effects of the circulating light field.

4.1 Glasgow 10 m Prototype Laboratory

The Glasgow 10 m prototype is a system which was designed for the rapid prototyping of new interferometric technologies destined for integration into the full-scale gravitational wave detectors. It fills the space between table-top proof-of-principle and full integration by using scaled-down versions of the full detectors; a required step due to the huge difference between setups and the need to have detectors operational for as long as possible. Moreover, the use of

prototype interferometers allows the testing of innovative technologies, while leaving the detectors in "observation mode" for as long as possible to maximise chance of detection. Prototypes are then required to minimise interference whilst integrating into the full-scale detector. As such, the prototype system has comparable parameter ratios with full-scale detectors, such as suspension size to beam power, spot size to mirror size and it uses similar locking schemes etc. The main difference between the prototype and a full-scale detector is that the arm length is reduced from km-scale to 10 m. The system is folded so that the arms are parallel rather than the traditional L shape due to space constraints in the lab. However, this does not hamper measurements as it was never designed as a detector for gravitational waves and thus there is no need to be sensitive to perpendicular length changes. This combination of mid-scale topology and easy reconfiguration makes the prototype system an ideal test-bed for the validation of new interferometric techniques.

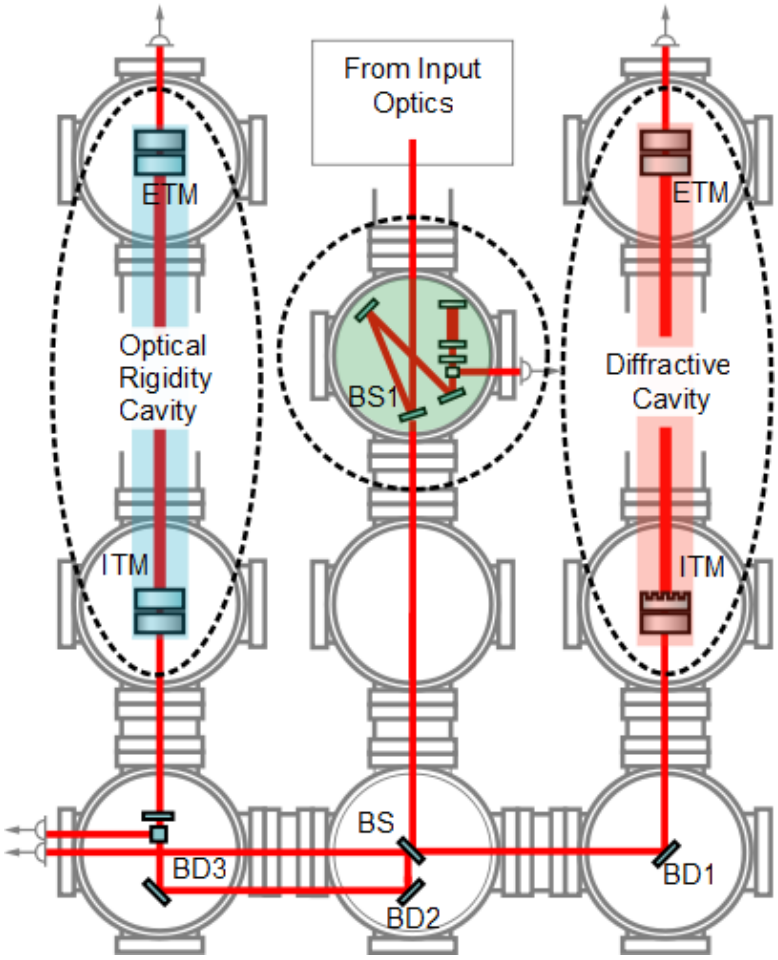

Figure 4.1: Schematic overview of the vacuum system detailing the location of each optic. The three main experimental areas coloured blue, green and red.

Figure 4.1 shows a schematic overview of the lab, indicating the 10 m arm cavity, coloured blue, that was central to the work discussed in this thesis. The 10 m diffractive cavity in this diagram was used for other experiments taking place in the lab and will not be mentioned again. The external frequency-readout cavity in green is central to the experiment detailed in chapter 6 and will be explained in full detail there.

Figure 4.2: View of the clean-room section of the 10m prototype lab where all experiments were undertaken. Long vacuum tube is skewed due to camera lens and houses the 10 m cavity referred to throughout this thesis. The main optical bench with laser, amplifier and conditioning optics is seen far left with the large tanks shown that house the suspensions for the optics. Image- K. A. Strain.

Figure 4.2 shows the clean-room area where the experiments in this thesis were undertaken. The area is a class-100 clean room with the tents around the vacuum chambers kept to class 10 with the use of downward airflow to maintain positive air pressure around the chambers and to keep the optics as clean as possible. The 9 larger chambers house the suspensions and are connected with a 60 cm-diameter beam tube.

4.2 Control and Data System

The lab uses a control and data system (CDS) based on a similar design to that used in both GEO and LIGO for control, data acquisition and environmental monitoring of the detectors. This allows the system to operate effectively as a prototype using similar setups to those used at a detector site. The CDS has

four core CPU's, one for input/output control and three on which we can run models for control and feedback. It allows data to be recorded on up to 32 inputs at up to 65 kHz sampling rate and has 16 outputs allowing it to be used in control loops for some of the sub systems in the lab. The CDS is locked to GPS signal, meaning times are noted whilst experiments are undertaken and can be post analysed.

The system allows for fast and easy adjustment of feedback loops compared to traditional analogue electronics, making the development, optimisation and integration much quicker and easier. Alterations to these feedback loops can be done in real time and without the need to switch anything on/off. It is also possible to save and analyse data from multiple channels, simultaneously shortening measurement times and improving accuracy.

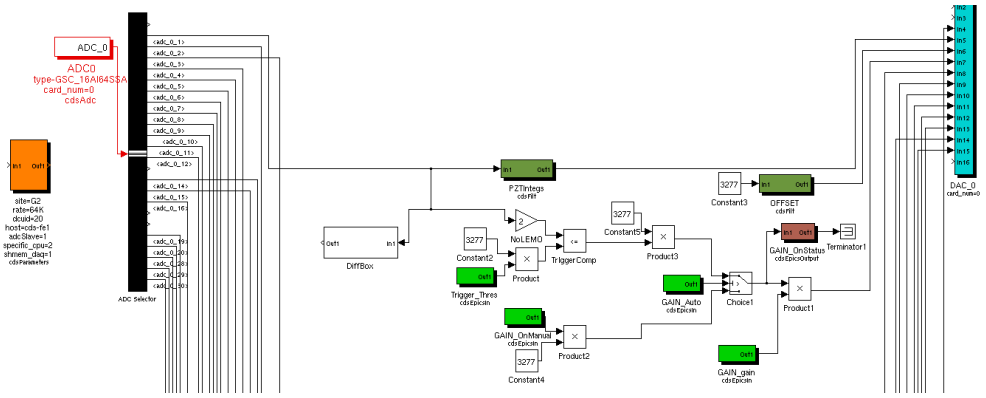

Figure 4.3: Screen shot of CDS showing simulink schematic controlling input to output commands and mathematical operations performed on signals.

The CDS is however not suitable for high-frequency feedback due to limitations imposed by the sample rate and is not as quick as analogue electronics for this purpose. An example of this is the laser-frequency feedback system that can have a bandwidth of up to 100 kHz. However, it is possible to integrate CDS with analogue control systems, which is what has been done in the laser-feedback case described in more detail later in this chapter.

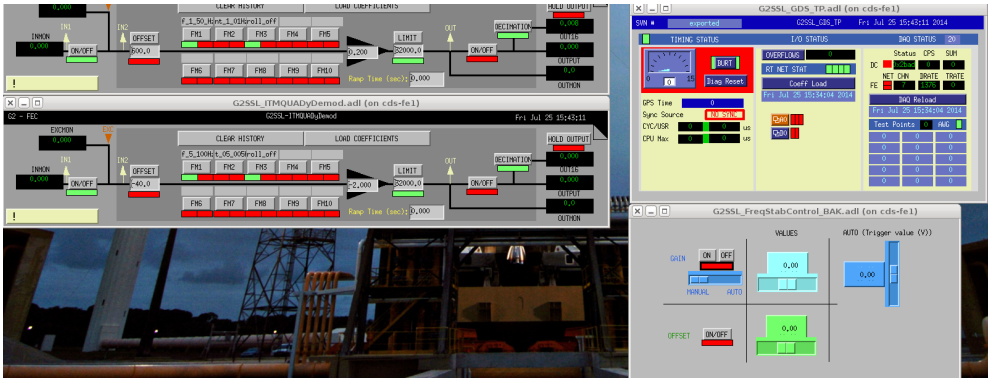

Figure 4.4: Screen shot of CDS showing filter banks for different channels (left), offset control (bottom right) and input output monitoring (top right).

In some scenarios read-in and readout noise can also be a problem, leading to the requirement of integration of additional whitening and dewhitening filters.

4.3 Optics

The two optics that make up the input and output cavity mirrors are both suspended as the bottom stage in a triple pendulum. The input steering optics that align the beam into the cavity are not required to be isolated to the same level, as the beam only hits them once, and so they only required a double pendulum. The triple-pendulum suspension of the ITM was the basis of the design for the GEO600 suspensions [40] and the LIGO quadruple suspensions [21].

The two suspensions are slightly different in design. We will first describe the three stages of the ITM triple suspension configuration. The top stage is suspended from cantilever blades attached to the frame mounted in the vacuum system to isolate vertical bouncing. Attached to this upper stage

Figure 4.5: Side by side comparison of ETM (left) and ITM (right) masses.

are the position sensor flags and coils for the damping and alignment control (discussed in the following paragraph), then two wire loops are used to suspend the intermediate mass (also 2.7 kg) and finally two more wire loops are used to suspend the ITM mirror at the bottom stage.

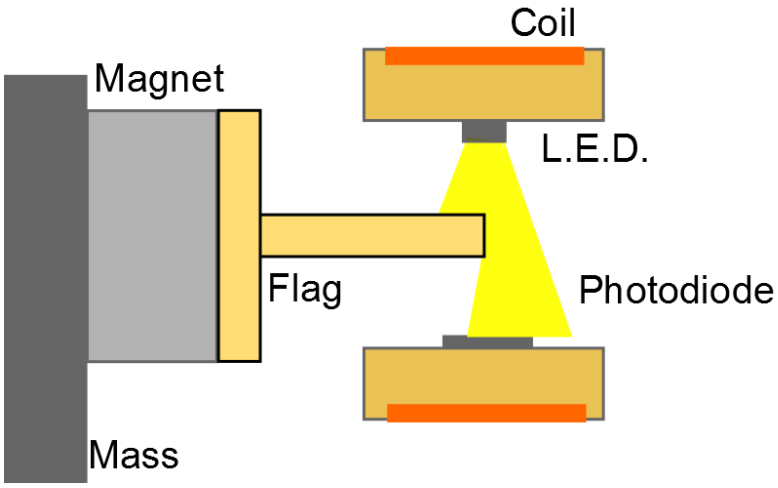

Figure 4.6: Flag position feedback sensor schematic. The magnet, and flag, are attached to the ITM suspension while the coils are attached to a frame bolted to the ground. Feedback is provided to all 6 degrees of freedom.

The flag position sensors allow monitoring of the mass position on the upper stage of the suspension and allow feedback to be applied to the mass to stabilise any oscillations. The error signal here is achieved by setting the coil (with LED and photodiode) shown in figure 4.6 such that the photodiode is neither fully bright nor dark. This is then used as a zero point crossing for stabilising suspension oscillations. The feedback is applied by applying a current through a wound copper coil, mounted on the reaction suspension which produces a magnetic field that's polarity depends on the direction of current flow. This actuates on the magnet attached to the main suspension allowing the mirror to be pushed and pulled. Static offset voltages are applied to provide alignment control. These actuators are located on the upper stage of the pendulum so any electronic noise that is introduced is still filtered by the stages below. The servo of this damping rolls on up to 0.3 Hz and is then flat. The feedback loop has a lower unity gain point (UGP) at around 0.03 Hz and has gain of around x10 from 0.3-0.58 Hz, at which point actuation drops off due to the isolation of the pendulum, and has a higher unity gain point at 10 Hz. A step-up differentiator is required in this range to change the $1/f^2$ of the pendulum to $1/f$ to provide stability at the unity gain crossing.

The ETM suspension was specifically designed for the first set of optomechanical rigidity measurements done in the Glasgow prototype [41]. The use of a light mass made it much more susceptible to the effects of radiation pressure and also helps to simplify investigations as most movement due to radiation pressure can be attributed to the ETM due to the ITM being much heavier. It makes use of a slightly simpler design compared to the ITM suspension. It uses passive eddy current damping, but still has coil-magnet control on an upper stage for alignment control [42].

Both cavity mirror suspensions have a near identical reaction pendulum chain

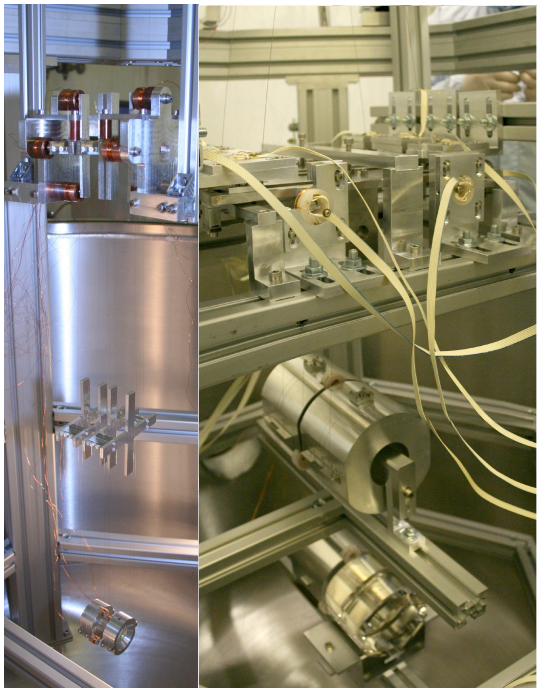

Figure 4.7: Side-by-side comparison of ITM and ETM suspensions.

which hangs behind the main optic suspension. The only difference being the bottom stage is not a mirror, but in this case an aluminium blank of the same weight as a mirror with a hole through the centre to allow the beam to pass through. The main purpose for this is to allow actuation directly onto the mirrors without seismically short-circuiting the main suspension. The reaction chain also acts as an injection point for feedback actuation and to probe cavity response. This is done in a similar way to the damping with magnets attached to the mirror and wound coils through which current is passed attached to reaction mass. A diagram showing the back surface of the ETM is seen in Figure 4.8, showing the location of the magnets at 4,8 and 12 o'clock.

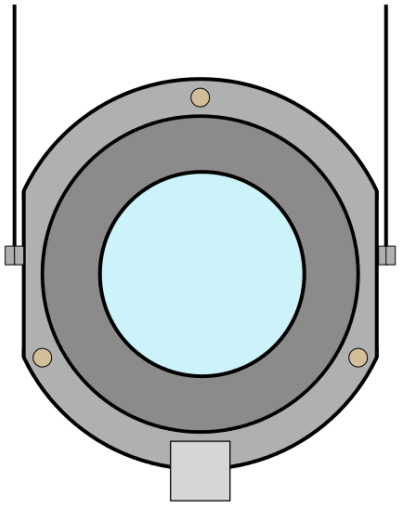

Figure 4.8: Diagram of ETM showing beveled aluminium holder with small, square, silvered mirror glued to the back surface (purpose explained in Chapter 5). Also shown are the clamping points on either side for the suspension wire and also three neodymium magnets glued to the surface at 4,8 and 12 o'clock.

Each stage of the suspension chain has a length of 30 cm, giving a fundamental resonance at 0.6 Hz which can be seen in figure A.2. Above this frequency, the pendulum isolates $1/f^6$ due to the cascaded three stages meaning the ground vibrations of around 10^{-6} m are now down at 10^{-18} m by 100 Hz, well below other noise sources in this range.

4.4 Laser Amplifier

To reach the regime whereby cavity dynamics are opto-mechanically dominated, high input laser power is required for the sizes of mass used, 2.7 kg and 100 g. The main laser used was a 1064 nm, 2 W, non-planar ring-oscillator (NPRO) [43] which after beam conditioning optics, polarisers, Faraday isolators etc was reduced to around 1 W. To achieve the power needed, a laser

amplifier was built consisting of a KTP crystal (Pottassium titanyl phosphate) through which the original beam was double passed off axis. This allowed optimum gain by not saturating the crystal and also prevented potential parasitic cavity problems caused by having the crystal perpendicular to the beam path. The crystal was pumped with 20 W of 880 nm light, giving a maximum power out of the amplifier of 5.2 W.

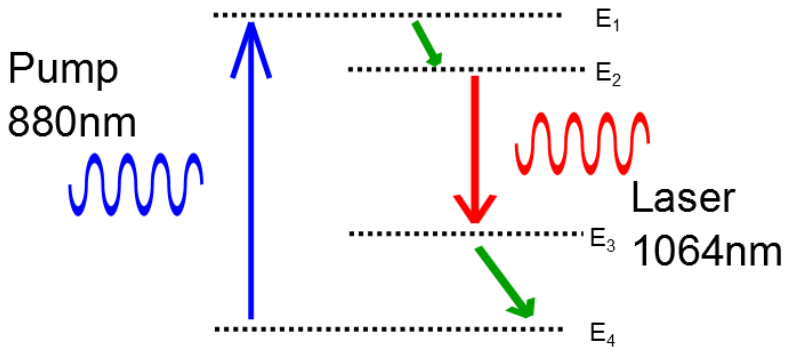

Figure 4.9: Energy level description of the amplifier setup. The crystal is a 4-level system whereby the pump light creates a population inversion from ground state E_4 to upper state E_1. A fast decay then occurs from E_1 to E_2. Stimulated emission causes emission of photon of energy $E_2 - E_3$ which gives 1064 nm. A final fast decay from E_3 to E_4 brings the system back to its ground state.

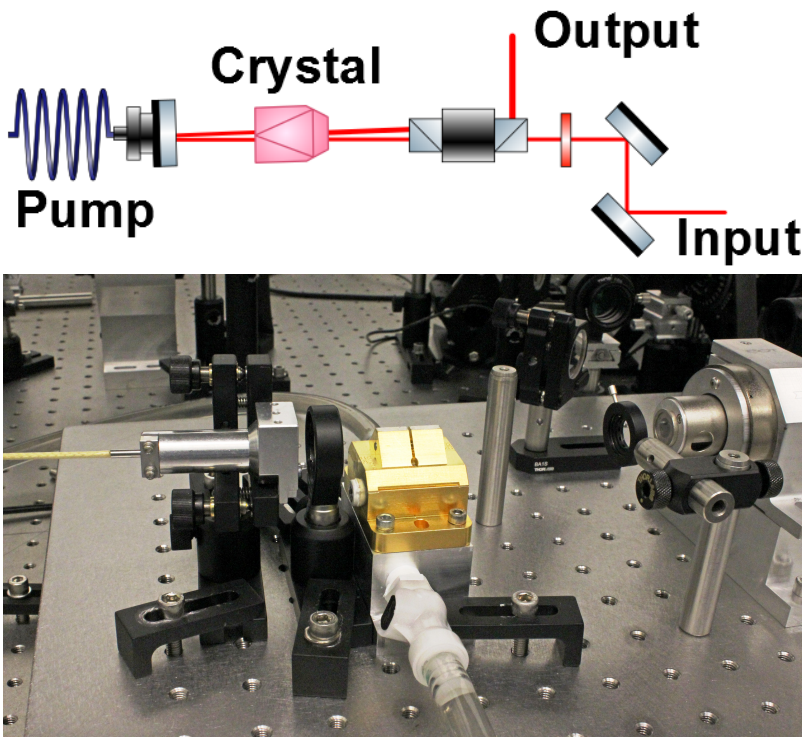

Figure 4.10: Optical layout of Laser amplifier showing the pump light entering from the left through a fibre. The KTP crystal is mounted in the gold water-cooled block, centre, and the pick off faraday isolator on the right.

4.5 Sensing and Demodulation

The arm cavity was setup to mimic the arm cavities used in a gravitational wave detector and so Pound Drever Hall (PDH) reflection-locking [35] was used. The input light was phase modulated using an electro optic modulator (EOM) at 10 MHz and the reflected signal was then detected on the RF photodiode and demodulated to give a control signal as described in Section 3.1.2. Throughput and reflected photodiodes were also used for power monitoring purposes, with the reflected signal giving a good estimation of visibility and throughput giving a good measure of power stored in the arm cavity. Both traces help to optimise

alignment of the cavity, together with rough alignment estimation based on the image of the transmitted cavity TEM modes viewed on a CCD camera. By observing the spread of mode-shape across vertical and horizontal axes it was possible to correct for first-order mirror misalignments and bring the cavity into auto-alignment range.

The main 10 MHz signal was taken from a Wenzel crystal oscillator [44], giving a very stable reference. All other 10 MHz signal generators used were phase locked to this, allowing individual optimisation of the demodulation phase. The main reason for choosing the Wenzel device to generate the sideband frequencies was the very low phase noise it produces, $-165\,\mathrm{dBc/Hz}$ at 1 kHz, which was required for one of the other experiments in the lab. An overview of the full RF sensing and demodulation setup is shown in Figure 4.11

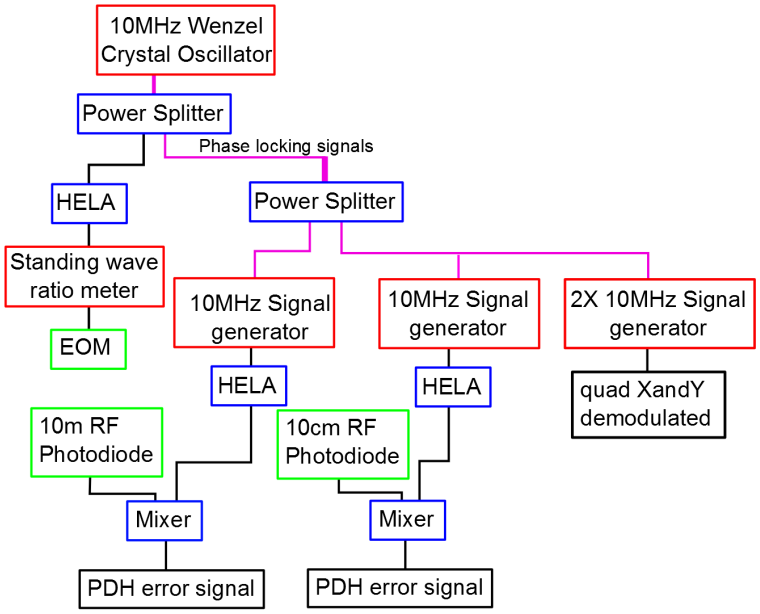

Figure 4.11: RF setup. A HELA is a low noise RF amplifier with 12 dB of gain.

As previously described in section 3.1 the sideband power related to the carrier can be expanded in terms of Bessel functions. Simulating the cavity sensing signals, it was decided that a modulation index of 0.6 would provide a strong error signal with sideband powers of about 9% of the carrier without reducing the carrier power used to produce the optical spring. This was measured using a scanning Fabry-Pérot cavity. A standing-wave ratio meter was included in the RF setup to ensure proper impedance matching and therefore power coupling into the EOM circuit.

An EG&G InGaAs photodiode was used for its high speed (flat response up to 75 MHz into a 50 Ω load) and low-noise performance. The output bench shown in Figure 4.11 was set up so that approximately 10 mW of light was incident upon the photodiode for optimum noise performance. It was then wired as part of a transimpedance amplifier shown in Figure B.3. The signal was then demodulated using a RAY-3 MiniCircuits mixer [45] which had a local oscillator specification of 23 dBm, meaning the peak-to-peak error signal size could be maximised to allow better fine-tuning and control over the detuning parameter (DC offset) used to create the optical spring.

Taking into account a photodiode efficiency of 0.6 A/W and 10 mW incident power gives 6 mA of photocurrent which flows through the 220 Ω resistor in the transimpedance amplifier, giving voltage output from photodiode amplifier of 1.32 V. It is now possible to calculate the the peak-to-peak voltage or the error signal by taking the RF power and converting it to voltage on the photodiode. The RF power is given by $\sqrt{\text{sideband power}(1\,\text{mW})} \times \sqrt{\text{carrier power}(9\,\text{mW})}$ which gives 3 mW of RF power, giving a peak-to-peak error signal size of 0.4 V.

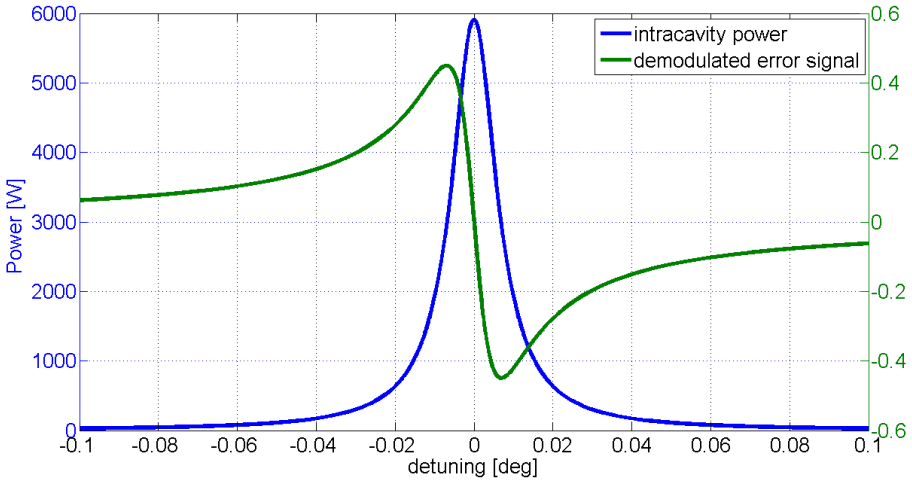

Figure 4.12: Demodulated error signal from model.

4.6 Frequency Stabilisation Servo

The 10 m cavity-locking servo for feeding back to the laser frequency was used for other experiments that were undertaken in the lab, and as such was over-designed for the requirements of the optical rigidity work discussed here. The control loop feeds back to the laser frequency via three channels, a high-frequency electro-optic modulator (EOM) (10 kHz-100 kHz), laser PZT (10 Hz-10 kHz) and the laser crystal temperature (<10 Hz). The loop has adjustable unity gain from 8 kHz up to 100 kHz and DC gain up to 100 dB. For the purpose of this experiment, the EOM was not used to allow the loop gain to be reduced at the measurement frequency, the reasons for which will be discussed later in this thesis. The full electronic schematics can be found in Appendix B.

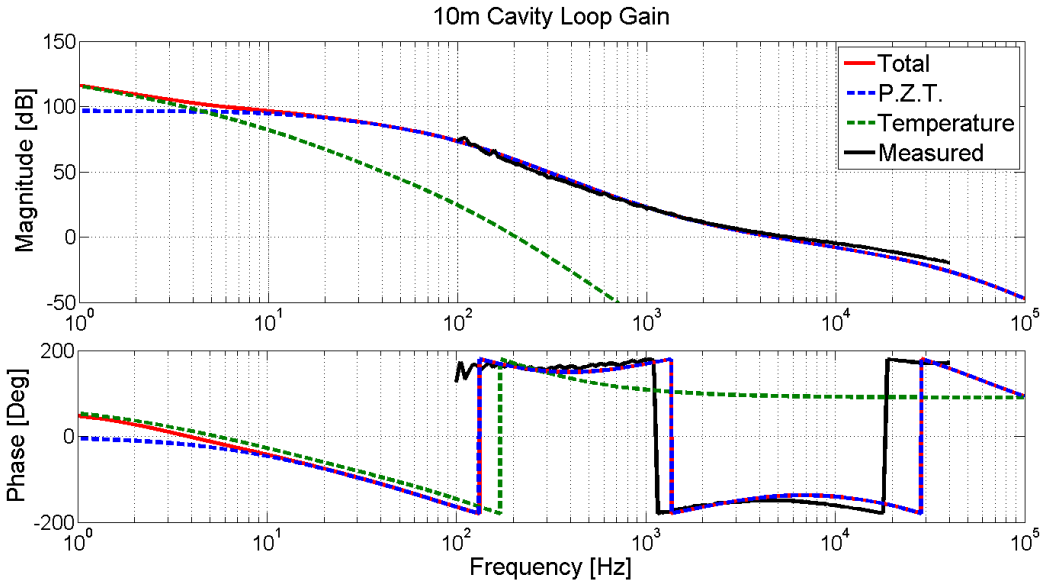

Figure 4.13: Frequency stabilisation loop response for PZT (blue) and laser temperature (green) and sum (red) feedback. The curves were produced using LISO and include the cavity pole and actuator response and the measured response of the system is shown in black.

Figure 4.13 shows both the measured and the modeled open-loop transfer function of the locked 10 m cavity frequency-stabilisation loop. The measured result only shows the region of interest between 100 Hz and 20 kHz, mainly because measurement towards lower frequency become difficult due to high Q pendulum modes and no measurements were taken in this region. The model, written in LISO, a linear analog electronic circuit simulation programme [46], and has also taken into account the cavity response and a measure of the gain based on the peak-to-peak voltage of the error signal. An additional differentiator response was also included because the EOM feedback is not being used in this configuration and electronics require additional phase at the much lower UGP to maintain stability.

The actuator response of the PZT of 1.35 MHz/V was measured numerous

times in numerous different lab experiments. For instance a measurement based on a linear mode cleaner setup allowed the laser to be well characterised as well as agreeing with the laser manual. It should also be noted that the laser has a flat frequency response across the very wide frequency range we are interested in. The temperature of the laser crystal is controlled with a peltier cooler where the response rolls off due to the temperature dissipation in the crystal. This has a cascading roll off effect from around 10 Hz; the response is approximately 1 GHz/V, which again was characterised using a linear mode cleaner. This number is not used for any calculations as measurements were all done in the flat, PZT only, response frequencies.

The CDS already records the PZT feedback signal from the servo. This was initially the signal that was filtered in the same analogue circuit to give the low frequency feedback to the laser crystal temperature. This was then integrated into a CDS filter bank to allow quick changes to be made to help optimise the system. Large DC gain was required to suppress pendulum modes, which was easy to do digitally with notches and resonant gain filters. The full filter bank and properties are described in Appendix B.

One of the reasons for the large DC gain is the large unsuppressed motion below the fundamental pendulum resonance; however, one of the more subtle effects occurs as the cavity is detuned. As the cavity is offset from resonance to create optical rigidity, the error signal becomes less linear as it moves towards the peak or trough seen in Figure 4.12, at which point the signal response drops to zero. The modeled error signal response for various detunings, calculated in Finesse, is shown in Figure 4.14

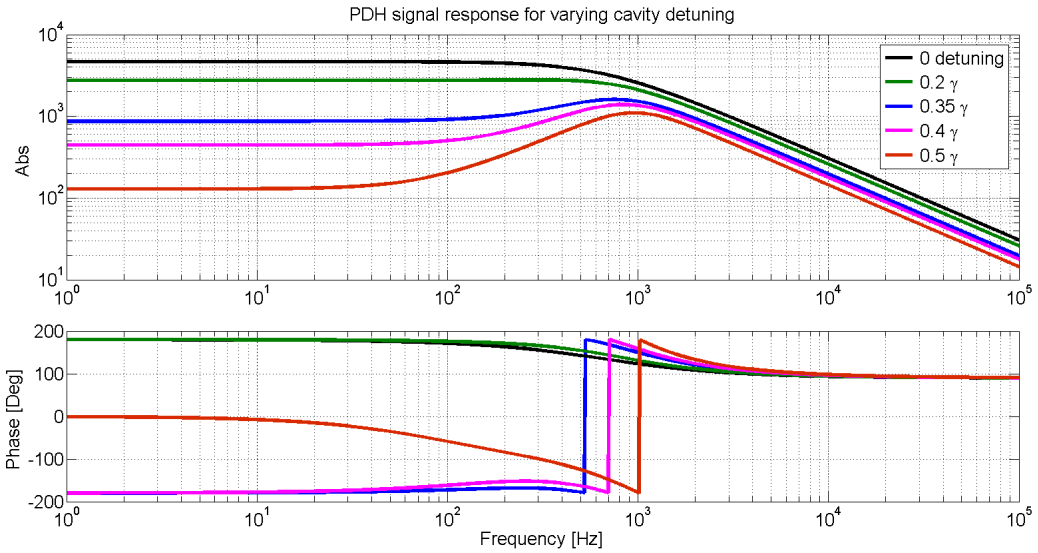

Figure 4.14: Finesse model highlighting the drop in gain at lower frequencies as the cavity is detuned further from resonance. The plot shows the PDH signal response for a variety of detunings in fractions of a linewidth (γ).

4.7 Auto Alignment Subsystem

Suspended optics, although good for isolation purposes, give rise to difficult experimental challenges of keeping the cavity at the correct operating point. Mirror motion away from the "aligned" state will cause the intracavity power to reduce, which in turn reduces the radiation pressure force on the mirror. This will then allow the pendulum restoring force to pull the pendulum back to equilibrium, causing a change in alignment, again changing the intracavity power. If this is a large effect, the system will become unstable. A further experimental investigation of this effect is detailed in section 5.3.5. Slow drifts of alignment also occur due to screws moving, optic mounts relaxing, doors slamming in adjacent rooms and temperature fluctuations causing expansions and contractions. All these effects can alter the alignment of the cavity and so

for this reason a feedback loop is created to feedback to the mirror position to keep it optimally aligned.

The technique of auto alignment has existed for a long time and is commonly applied in gravitational wave detectors and prototype systems and was first demonstrated in the Glasgow prototype many years before it looked the way it does now [47][48].

By analysing the mode component in the beam reflected from the cavity, information can be obtained about the alignment of both mirrors in tilt and rotation. Due to the carrier interacting with the cavity and the sideband field being non-resonant, if there is a misalignment in the cavity, modes will resonate. As the reflected signal is demodulated, cavity length information is obtained, whereby higher order modes indicate misalignment of the cavity mirrors.

At the heart of this system are the two quadrant photodiodes, one of which is shown in figure 4.15, which is split unsurprisingly into four, allowing signal fluctuations in tilt and rotation to be separated by summing two quadrants and subtracting from the other two. Top two minus bottom two gives tilt signals, two left minus two right gives rotation signals. These go to zero if the beam is perfectly centred with the same amount of light on each quadrant and will be used later on to create a zero-crossing point for a feedback loop to ensure the beam remains centred. Demodulating these signals allows the mode content to be seen, as tilt misalignment introduces 01 mode and rotation misalignment introduces 10 mode[1]. Again these go to zero as the amount of each mode is reduced as the system becomes better aligned.

[1] Here the mode numbers refer to the mode indices of Hermite-Gaussian modes.

During this work we had initially intended to only feedback to the ETM due to the majority of motion suspected to be introduced from the lighter mass. However, it became apparent that it was difficult to obtain information from the demodulated signals about one mirror only and there was therefore a danger of feeding back movement of the wrong mirror and therefore introducing noise. For this reason we set up two detectors, separated by 90 degrees in Gouy phase, which gave near-field (ITM) and far-field (ETM) information and so alignment information can be obtained from both mirrors. The Gouy phase separation was calculated using the JamMt tool [49] allowing the position of Gouy phase telescope lenses to be optimised (L1 and L2 in Figure 4.18).

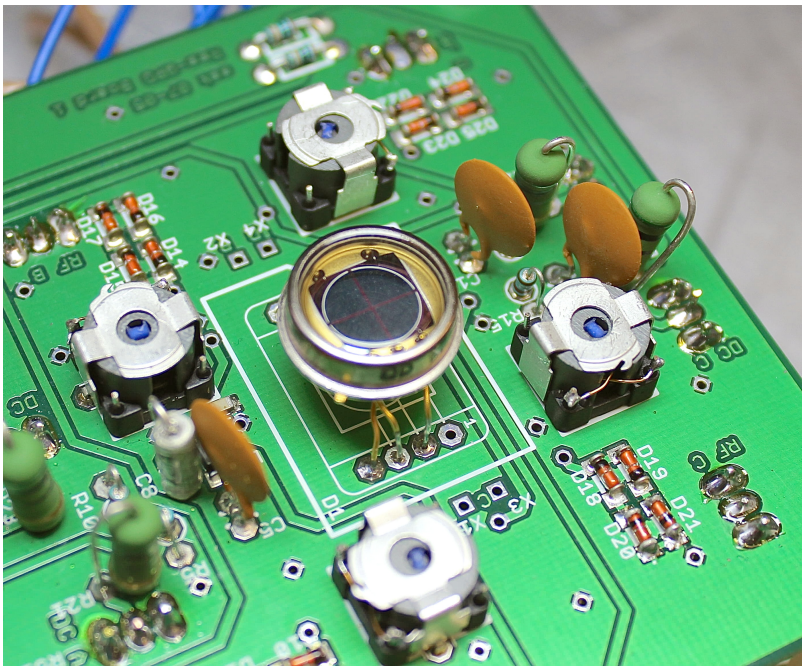

Figure 4.15: Quadrant photodiode and some of the associated electronics. One can just make out the split in the diode itself.

With the addition of a second detector it became apparent that not all noise on signals came from the ITM. For this reason, spot centering was implemented to keep the beams optimally aligned onto the photodiode. Having the beam off-

centre produced offsets in the demodulated signal and therefore in the locking point, which meant the cavity did not align to the optimum position and in some cases introduced instabilities when the feedback was applied. To this end, two scanning galvanometers were placed in the beam path, one in front of each detector. The feedback servo electronics constructed in CDS are shown in Appendix B. The locked transfer function of the centering servo is shown in figure 4.16 for one galvanometer in one axis. A unity gain frequency of around 700 Hz was achieved, well above the resonance of the galvos seen at around 320 Hz.

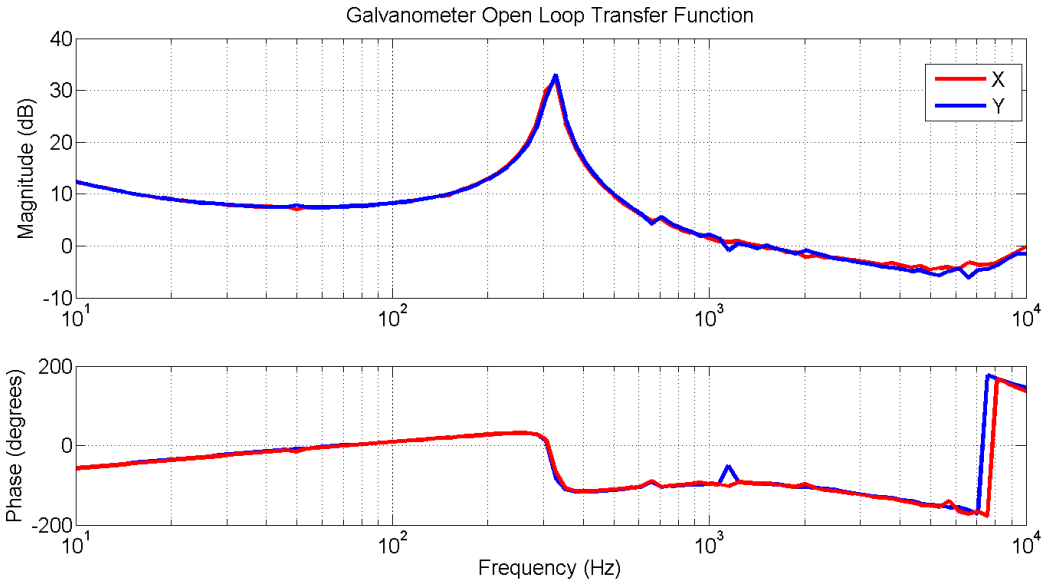

Figure 4.16: Measured spot centering servo transfer function in rotation (X) and tilt (Y).

To feedback rotation and tilt signals to the mass, the coil-magnet actuators on the bottom stage masses are used. By feeding back separate sign and magnitude to the three coils mounted at 4, 8 and 12 o'clock, tilt, rotational and longitudinal actuation can all be achieved.

Longitudinal actuation is achieved by driving all three coils with the same sign

and size of signal. Due to the bottom two magnets being positioned slightly up from the bottom of the mass they do not have as strong an effect but as there are two of them this balances the top coil. To achieve tilt actuation, the sign of the top coil is reversed to provide a push-pull actuation. Rotation can be achieved by driving the left and right coils with opposite signs with the top coil magnitude reduced to account for the small amount of tilt introduced by driving slightly below the centre of the mass. Each signal line has a small trimmer included to allow for balancing of each coil individually, which is required due to slight misalignments of the coil and magnet not being perfectly aligned.

For the auto-alignment feedback it was possible to use CDS, due to not requiring high frequency feedback, and simply feed the demodulated x and y directly into CDS. This made it quick and easy to build up filters to test the feedback system with. The Bode plot of the CDS filter bank is shown in Appendix B.

The unity gain point for each degree of freedom was around 5 Hz. Low frequency resonances make it difficult to increase this any further. The presence of an auto-alignment system allowed us to monitor the state of alignment and to switch on feedback as necessary. It was also possible to use these traces in the time domain to determine if suspensions were oscillating and if the system was well aligned. During measurements the auto alignment system was disengaged to avoid cross coupling when driving signals.

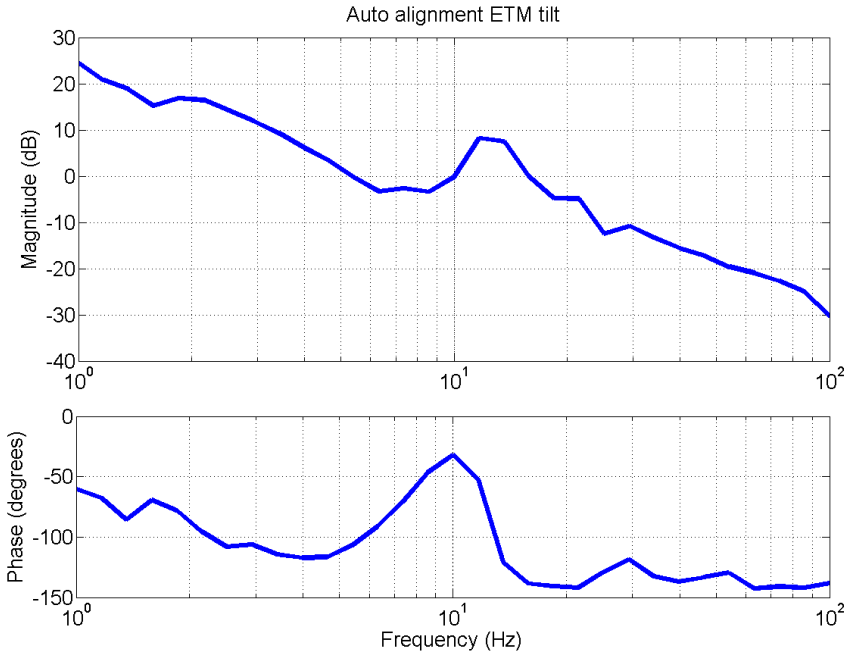

Figure 4.17: Measured transfer function of locked auto alignment on ETM tilt

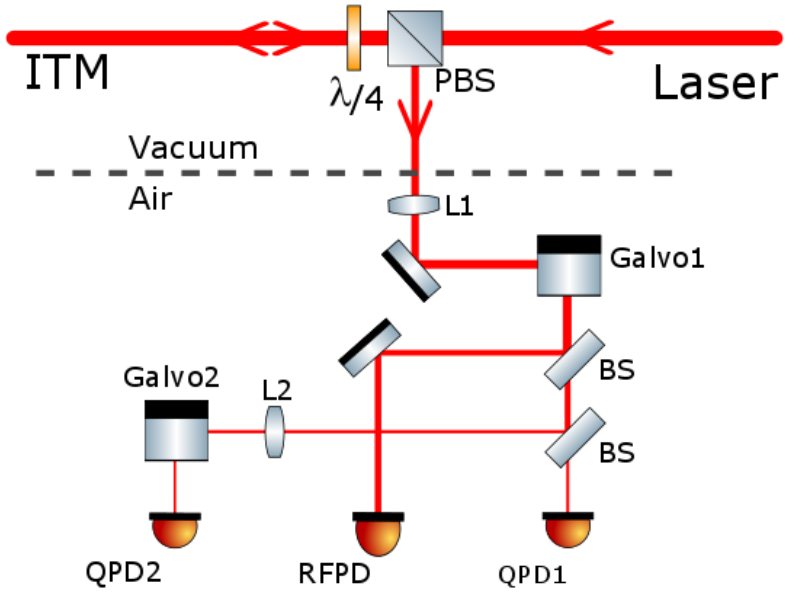

Figure 4.18: Readout bench optical layout consisting of two 50:50 beam splitters (BS), L1 and L2 are lenses that set the correct Gouy phase of the two quadrant photodiodes (QPD). The focal length of L1 is the optical path length to QPD1 and the focal length of L2 is the optical path distance to QPD2. The scanning galvanometer Galvo1 centres the beam on QPD1 and Galvo2 on QPD2.

Figure 4.19 shows the time series development as feedback of three out of the four degrees of freedom of the cavity is switched on. It shows the feedback signals going to close to zero, the optimally aligned case, as the feedback is switched on at time 5 sec. At time 26 seconds more integration is added causing the slight instability. The initial reflected D.C. photodiode voltage starts at 298 mV and once the feedback has been switched on this value drops to 252 mV, showing there is less light on the reflected photodiode, i.e. more light is coupled into the cavity due to better alignment.

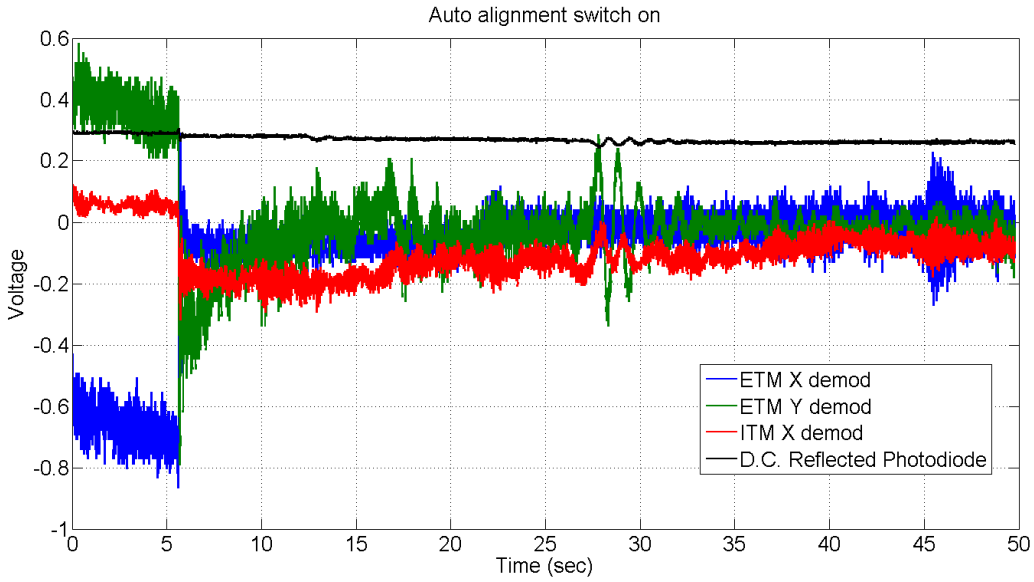

Figure 4.19: Time series showing auto alignment feedback being switched on after 5 seconds and integration added at around 26 secs. Three of the four demodulated traces move towards the zero crossing. The fourth, the reflected DC level, reduces from 298 mV after 2 seconds to 252 mV after 40 seconds showing more light is coupled into the cavity implying better alignment.

4.8 Experimental Modeling

Two separate programmes were used for modeling throughout the setup phase of this experiment and also in confirmation of results. The first, Finesse [50] was used for simulation and calculations regarding light fields, e.g. power levels, modulation levels, effects of length changes on error signals, etc. Finesse computes the light field amplitudes at every point in the interferometric setup, assuming a steady state. To do so, it is translated into a set of linear equations that are solved numerically.

The second programme, Optickle [51], includes the dynamics of the suspen-

sion and includes the effects of radiation pressure which until very recently Finesse did not. Optickle is able to study the dynamic effects in an interferometer where optics have associated mechanical transfer functions due to being suspended. This is then perfectly suited for investigation of optical-spring effects.

A sample of the code written to model the setup in both Finesse and Optickle is shown in Appendix C.

Chapter 5

Local Readout for Optical Bars

With advanced detectors expected to be quantum-noise limited (Figure 2.5), several topologies have been proposed for future upgrades. The Heisenberg Uncertainty Principle applied to the continuous measurement of a free mass, as the suspended optics are designed to be in the detection frequency band, sets the limit to the precision with which their position can be measured in the current configuration. By coupling these masses opto-mechanically, they no longer behave as free masses and as such the free-mass standard quantum limit no longer applies. The masses become harmonic oscillators with resonant frequencies that can be arranged to be in the detection band of the interferometer.

Methods have been proposed to give either a strong enhancement over a narrow band [52] (e.g. 10 Hz) or a much smaller enhancement over a broad band [53] (e.g. a factor of two improvement as might be obtained by applying squeezed light). Between these extremes there are two topologies that are the subjects

of this chapter: the local-readout and optical-bar topologies. An explanation of how these techniques are able to surpass the standard quantum limit is given, followed by detail of the first experimental proof of principle of such a setup. The associated control requirements and comments on the suitability for integration into a full-scale detector are presented.

5.0.1 Standard Quantum Limit

The standard quantum limit (SQL) arises from Heisenberg's uncertainty principle which states that there is a fundamental limit to how accurately a position can be known without imparting momentum on the object to create an error on its future position. This imposes a sensitivity limit on gravitational wave detectors in their current configuration. Heisenberg's uncertainty principle states that two non-commuting variables cannot be simultaneously measured to arbitrary accuracy but are limited such that in the position(Δx)-momentum(Δp) case the limit is set by Planck's constant:

$$\Delta x \Delta p \geq \hbar. \tag{5.1}$$

The important requirement for a gravitational wave detector is that the mirror surfaces behave as free masses and movement caused by ground vibrations, Brownian noise of the mirror surface, or the fluctuations in radiation pressure caused by the Poissonian nature of the laser beam, do not mask the gravitational wave signal to be detected. The Heisenberg uncertainty principle applied to a gravitational wave detector's sensitivity limit appears in two forms: shot noise and radiation pressure noise. As one noise is suppressed, the other increases and vice versa; the equations that describe this are shown below and the full derivation can be found in [52].

$$h_{sn}(f) = \frac{1}{L_{cav}}\sqrt{\frac{\hbar c\lambda}{2\pi P_{cav}}} \tag{5.2}$$

$$h_{rp}(f) = \frac{1}{mf^2 L_{cav}}\sqrt{\frac{\hbar P_{cav}}{2\pi^3 c\lambda}} \tag{5.3}$$

Where $h_{sn}(f)$ and $h_{rp}(f)$ are the seperate strain sensitivities for shot noise and radiation pressure noise at frequency f. P_{cav} is the intracavity power and m is the reduced mass of the cavity mirrors and L_{cav} is the cavity length. It can therefore be seen that the only way to improve sensitivity is by increasing the mass of the optic. Advanced detectors will use 40 kg masses, which are at the current limit of technology for creating a mirror that size out of material of the required quality.

The quantum noise line shown in Figure 2.5 shows the sum of radiation pressure noise and shot noise for a single-power level. The SQL line in Figure 5.1 is obtained by varying power levels and creating a line from the minimum point of each separate quantum-noise curve.

It is emphasised that the test described below is entirely classical and is intended to demonstrate methods that may later be developed to show quantum-mechanical behaviour.

5.0.2 Optical Bar in Advanced Detectors

The optical bar topology was first proposed by Braginsky [54]. The principle behind this geometry is that an additional optic is added to the interferometer, labeled CTM (central test mass) in Figure 5.2. This mirror forms a cavity with both of the ETMs, each cavity is then detuned, opto-mechanically coupling the CTM to each with optical springs. At this point any differential arm motion

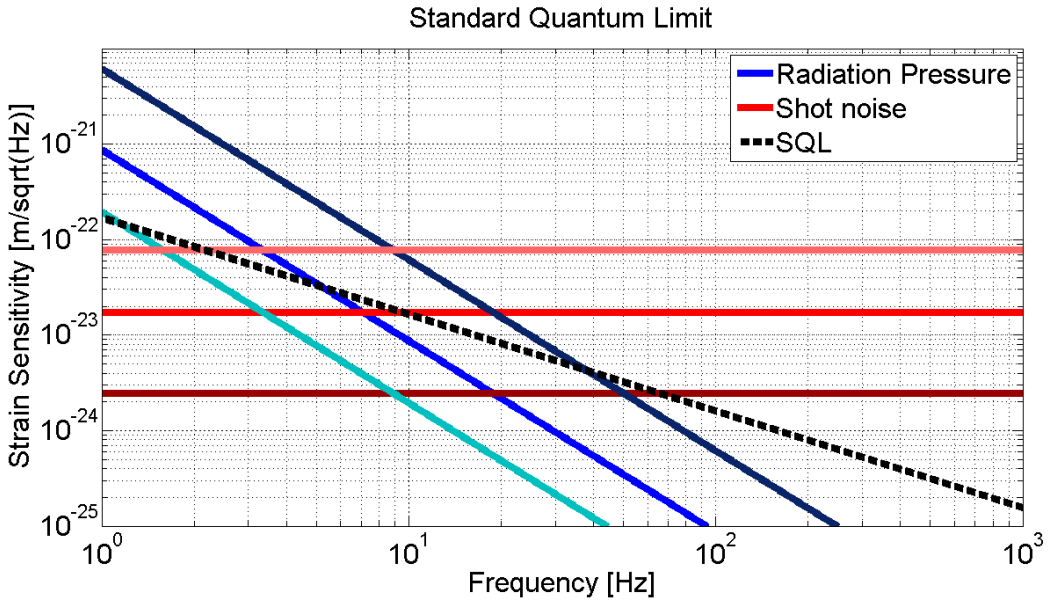

Figure 5.1: The SQL corresponds to the lowest sum of shot noise and radiation pressure noise, shown here for 3 different power levels, 1, 10 and 100 Mw. Increasing power level indicated by increase in darkness of blue/red.

caused by a GW signal will be transduced to a local movement of the CTM at the GW frequency. Not only is it visible but the effect is also double due to the push-pull effect along the beam path caused by one ETM getting closer to the CTM and the other further away. By monitoring the position of the CTM with a separate subsystem it would then be possible to measure the GW signal. The separate subsystem, known as a local readout, shown in green in Figure 5.2 does not interfere with the quantum state of the system and as such allows the interferometer to surpass the SQL as well as benefiting from spring resonant features.

Figure 5.2 is subtly different to standard GW detector in that the central beam splitter is not really a beam splitter but a high reflector meaning that system would be pumped from the back surface. Other more practical arrangements have been discussed in [55].

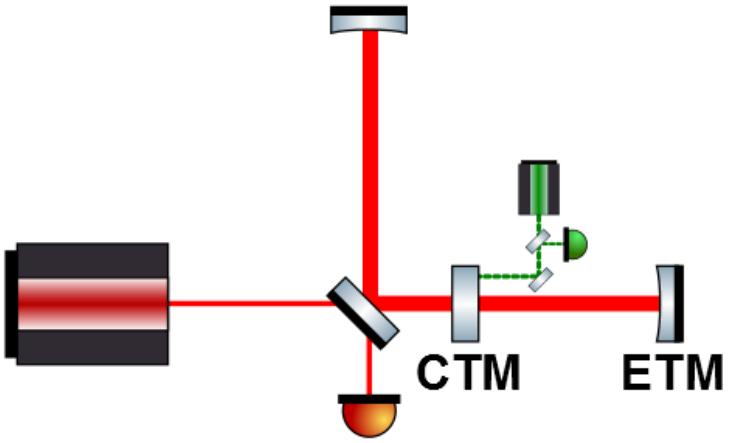

Figure 5.2: Schematic of optical bar topology. Both ETMs are coupled to the CTM with optical springs, differential arm motion generates a push/pull effect on the CTM. In green the local readout subsystem (not to scale) is shown monitoring CTM displacement.

5.0.3 Local Readout in Advanced Detectors

The local readout scheme, first proposed by Rehbein [56], differs from current Michelson interferometer configurations in two ways. Firstly, both arm cavities are detuned from resonance to rigidly couple both cavity mirrors, and secondly a separate subsystem is used to create another Michelson using the ITMs as the new ETMs. An overview of this is shown in Figure 5.3. At this point we will consider three gravitational wave frequency regimes: above, below and close to the arm cavities' optical spring resonance.

Above the optical spring frequency, the effect falls off as any harmonic oscillator above resonance as $1/f^2$, so at higher frequencies does not affect the system and the gravitational wave is measured using the standard Michelson. At and around the spring frequency there is a resonant enhancement of the gravitational wave signal caused by the optical spring and the signal is amplified and again read out in the standard Michelson. At frequencies below the

optical spring frequency the masses behave as though rigidly coupled. With this rigid coupling of the light field to the masses, a gravitational wave will induce motion of the ETM onto the ITM and the gravitational wave signal can then be read out using the subsystem of the inner interferometer.

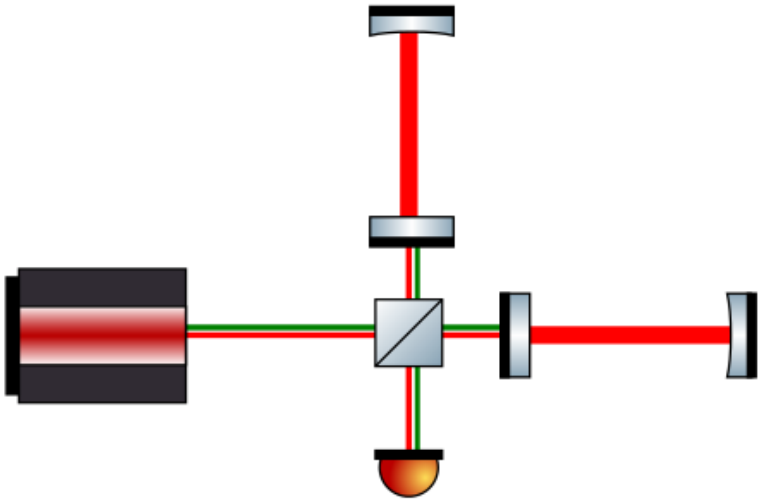

Figure 5.3: Schematic of local readout topology proposed by Rehbein et al[56]. The subsystem denoted in green is creating a Michelson interferometer using traditional ITMs as ETMs

The optimisation of parameters such as mirror mass, light power etc for this type of setup were it to be integrated into an advanced detector has already has already been undertaken [56]. The optimised sensitivity curves are shown in Figure 5.5. These curves are taken from Rehbein [56] which describes a realistic employment of this topology into a LIGO detector. The important aspect of this setup is not only the resonant enhancement caused by the optical spring but also the use of a subsystem to infer the ETM motion from photons which have never interacted with the ETM, allowing the SQL to be surpassed. Unfortunately this means the effect of the Fabry-Pérot cavities is negated as there is no phase change effect from the cavities since, due to the optical spring, the mirrors move together. This is a form of quantum non demolition (QND)

measurement, a term for these types of measurement first used in [57].

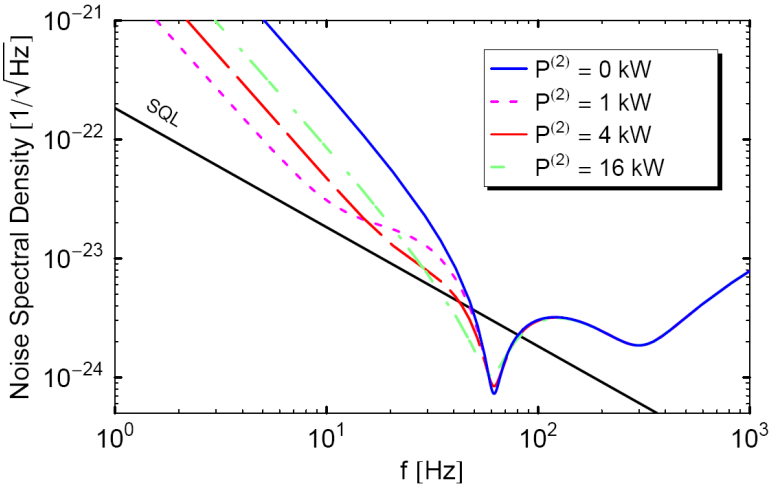

Figure 5.4: The plot shows the change in the quantum-noise limit for varying the second carrier power [56].

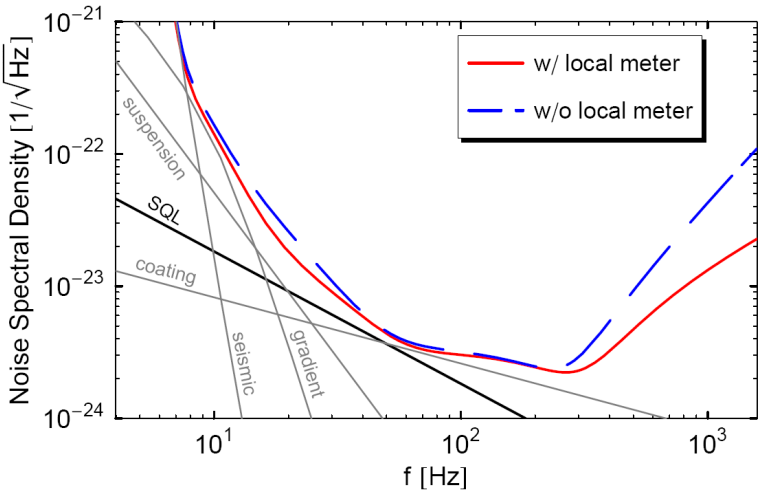

Figure 5.5: Potential sensitivity improvement in Advanced LIGO for local read-out integration using carrier power of 4 kW [56].

5.1 Experimental Aim

The aims of the experiment were to undertake the first demonstration of an optical bar setup and to investigate the development that would need to take place before it was integrated into a full scale gravitational wave detector. To achieve this, a subsystem was set up to continuously measure the displacement of the ETM of an opto-mechanically coupled cavity. The plan is then to drive the ITM along the cavity axis mimicking a GW signal, and to measure the coupling of motion to the ETM using the sub system. This will show that the sub system is able to measure the motion of the ITM using photons which have never interacted with the other cavity mirror.

5.2 Local Readout Devices

For the purpose of this experiment, two separate systems were used as local readout devices. The first was a displacement sensor monitoring the position of the ETM cavity mirror. The other was a separate suspended cavity which was able to measure the frequency of the light in the 10 m cavity.

The frequency-readout cavity will be described in full in the following chapter but the key points are summarised here. The full layout of the system can be seen in Figure A.1, showing how the cavity interacts with the rest of the system. 30% of the light input to the system was picked off to an ultra-low-noise cavity that was set up to show frequency noise by reducing mirror displacement noise to $10^{-17}\,\mathrm{m}/\sqrt{\mathrm{Hz}}$ at 200 Hz. The cavity was locked using reflection PDH and feedback was applied to the cavity length by actuating on the ETM longitudinal coil drivers. This means that the error point signal gives a good description of frequency changes of the light in the 10 m cavity.

The second device used to monitor ETM motion along the cavity axis, was a EUCLID (Easy to Use Calibrated Laser Interferometer Device) which was developed in Birmingham University [58]. It has a design sensitivity of $10^{-13}\,\mathrm{m}/\sqrt{\mathrm{Hz}}$ at 100 Hz and was installed on a 5-axis micron alignment stage on top of a rubber isolation platform. The vibration isolation reduced the influence of ground motion, while the precision stage provided the necessary alignment of the EUCLID beam to within better than 1 degree as set out in its user manual. The light source in the EUCLID is a 633nm Vecsel. To allow the resulting beam to be reflected from the ETM back to the detection optics within the EUCLID, a small aluminised mirror was mounted on the lower front surface of the aluminium (mirror-holder) part of the ETM. An identical mirror was also mounted on the back surface of the ETM to maintain the balance of the suspension.

The EUCLID is basically a Michelson interferometer where one arm is internal to the device and the other arm is ejected out and reflected of the surface one wishes to measure. For best frequency-noise suppression this requires both arm lengths to be close to identical, i.e. the EUCLID should be placed very close to the object it is trying to measure due to the internal arm length being quite short of the order 10's mm. A full description of the EUCLID can be found in [58].

5.2.1 EUCLID Readout

We now look at how to interpret the data acquired from the EUCLID. It was connected via USB to a stand-alone lab computer where recording could be controlled with the supplied software, allowing decimation rate, sample rates, resolution and length of measurement to be set. The data was then recon-

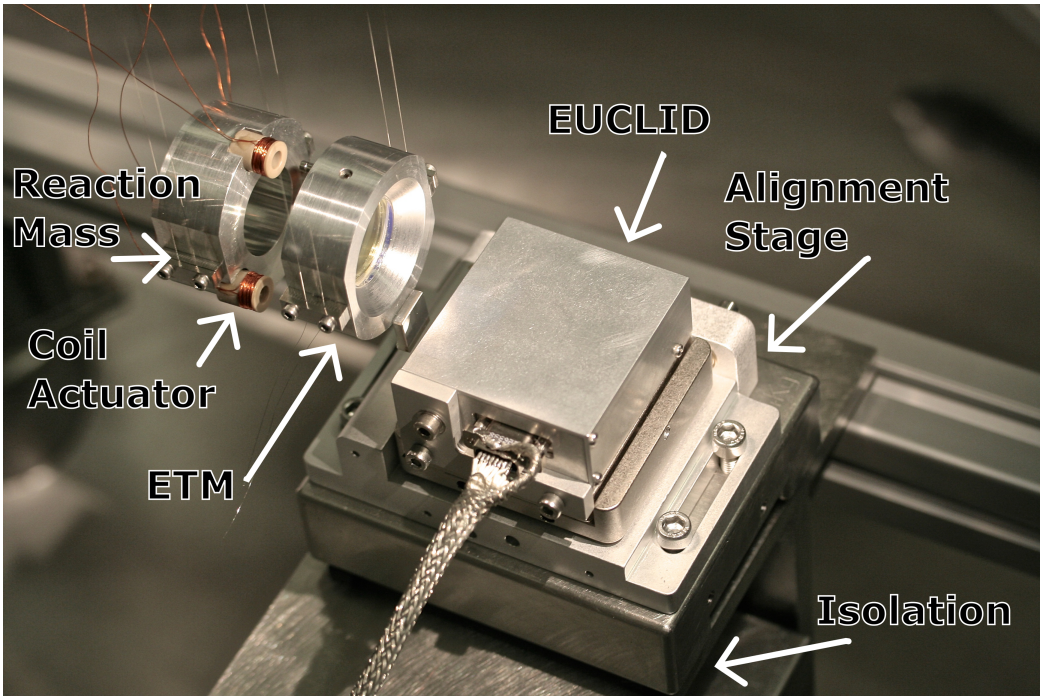

Figure 5.6: Image showing the bottom stage of the ETM suspension , reaction mass suspension, one of the small silvered mirrors and the EUCLID.

structed in a supplied Matlab script to create one time series of displacement, allowing spectra to be created. At this point it becomes important to fully understand as best as we can the spectra observed from the EUCLID and how to interpret them.

The alternative ways to generate useful spectra are either to employ the entire data set (windowed as necessary) to produce maximum resolution, or to average the results from shorter stretches, to give a better estimate of the noise (with lower frequency resolution). Figure 5.7 shows the sensitivity curve measured by the EUCLID with low resolution/more averages. At low-frequency the pendulum modes can be seen (see also figure A.2). At high-frequency, the noise level matched the specification given in the EUCLID data sheet. The mid-frequency noise shoulder is caused by up-conversion of large low frequency motion. This was verified by injecting gradually larger signals onto ETM and seeing the shoulder increase in frequency. It is possible to overcome this effect by selecting only lower-velocity segments of the time series data, however then the benefit of longer integration time is lost. The effects of up-conversion in the measurements were minimised by taking data in the evening, when the building was quieter.

From analysing the low frequency modes of the pendulum motion shown in figure A.2 as well as other tests including the comparison with a commercial Polytec vibrometer [59], the EUCLID is well calibrated in magnitude as a function of frequency.

5.2.2 Required Signal Size

It is important to choose the optimal frequency for best SNR at which to inject signals and characterise the system. The steps used for this calculation will

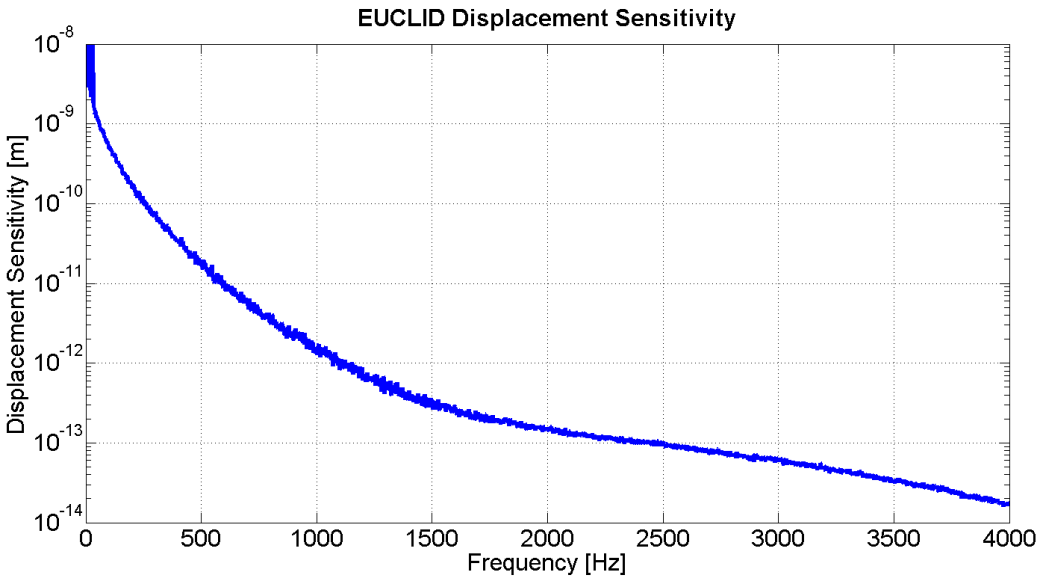

Figure 5.7: EUCLID sensitivity curve. Figure A.2 shows the low frequency end of the spectrum in more detail.

now be explained. In magnitude, the lower limit of the measurement is set by the EUCLID sensitivity curve, with the upper limit is set by the distance the mass can be pushed until the frequency stabilisation servo can no longer keep the cavity locked.

With a cavity linewidth of 560 Hz, any strong optical resonance features will be suppressed above this, and the EUCLID not having the required noise performance below this frequency, it became clear that measurements would need to be made in a frequency range above the optical spring resonance. The resulting response is like any damped harmonic oscillator above resonance, e.g. the response of the simple pendulum described in Section 3.2. As it was impractical to synchronise EUCLID data with our signal sources, we did not investigate the phase behaviour to confirm the expected 180 degree change.

The largest motion we can apply to the ITM is around 0.6×10^{-11} m or, and the highest frequency is the cavity linewidth, $\gamma = 570$ Hz. There are two reasons

for this limit, firstly, the amount of current that can be passed through the coils to actuate on the mass, and secondly not injecting too big a signal such that we approach the point of zero feedback in the error-signal slope at a detuning of ± HWHM of the cavity (seen in Figure 4.12). The slope of the error signal goes to zero as the linewidth is approached and so there is no feedback at these points. The feedback servo works to counter any cavity-length change by altering the laser frequency to follow the motion. How closely it follows is dependant on the loop gain shown in Figure 4.13.

It is possible to calculate the amount of power fluctuation for a given displacement by looking at the Airy peak of the cavity in figure 5.8. This is the property we wish to try to maximise to get the largest power change for a given length change $\frac{\partial P(\theta)}{\partial \theta}$ in equation 3.32. This occurs at the steepest part of the Airy peak around detuning of ± HWHM, however, this would mean only small signals could be driven due to approaching the point of zero feedback in the error signal slope so a compromise must be found. Smaller detuning means larger signals can be driven, but this limits the optical spring strength.

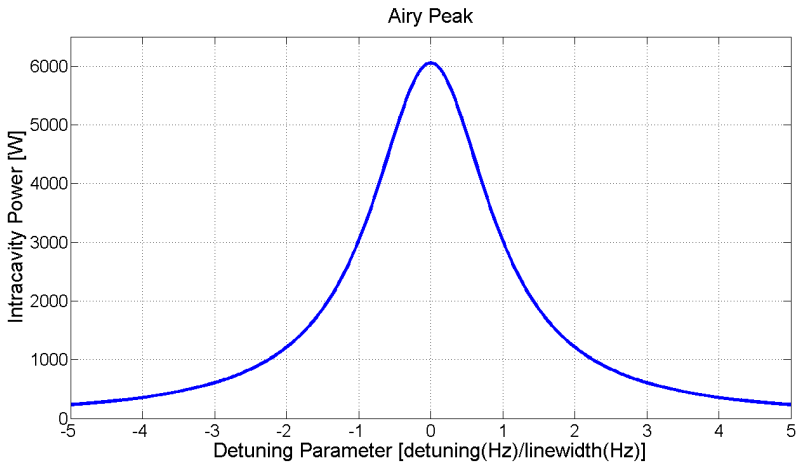

Figure 5.8: Intracavity power as a function of cavity detuning in terms of fraction of the cavity linewidth.

5.3 Measurements

The main aim of the optical bar and local readout experiment was to add a longitudinal (along cavity axis) signal onto the ITM of the detuned cavity and measure the coupling of motion to the ETM with a separate subsystem. The system setup for the experiment is shown in figure 5.9, with the full system shown in figure A.1.

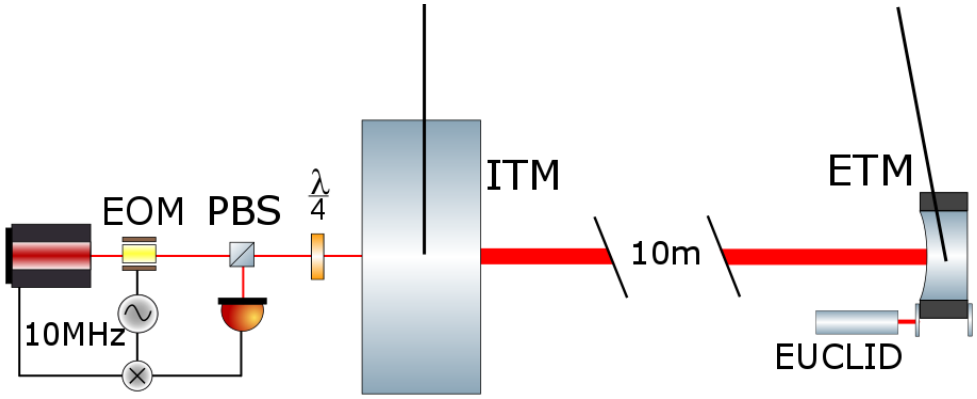

Figure 5.9: Schematic of experimental setup.

An extension of this idea was to actuate on the frequency of the light. This provides a complementary test that removes some variables from the measurement. Both modulation of the laser frequency and driving the test mass create sidebands on the light. It was therefore important that the effects produced by these two methods of introducing phase sidebands were in agreement. Modulating the light frequency can be done directly, with a reliable calibration.

Cavity Property	
ITM transmission	416 ppm*
ETM transmission	2.4 ppm*
Finesse	12780*
round trip loss	65 ppm
intracavity power	6 kW

*Table 5.1: Table showing predicted and measured values of 10m cavity properties. * indicates measured values, other parameters are calculated from model.*

5.3.1 Actuation on the Mass

Due to the impracticality of measuring the power directly incident on the 10 m cavity when the system is in vacuum, the ratio of the power there to that at a monitor point on the laser bench was established. This monitor was then used as an indication of the power incident on the cavity. The power in the system is accounted for as follows: 5.2 W leaving the amplifier with a wave plate and polarising beam-splitter immediately afterwards which is used for power control. This was set to reduce the power by 0.465 times. 50% of the light light is directed, by a beam-splitter to a separate experiment (not described in this thesis). A further 30% of the power goes to the frequency readout cavity, giving a total of 850 mW incident on the ITM.

It was possible to drive the ITM longitudinally using coils mounted on the reaction mass acting on magnets mounted on the bottom stage of the suspension (i.e. on the ITM itself). The current was limited by selecting the appropriate feedback resistor to set the ratio of voltage into the current driver to current in the coils. The circuit of the current driver is shown in Appendix B. A 922 Hz signal was injected onto the ITM whilst the EUCLID recorded data for

5 minutes. The longer the measurement time the better the SNR that is obtained. Given the injection is single-frequency, the measurement is improved as the square root of time. Figure 5.10 shows the spectra measured by the EUCLID with a positive and negative detuning applied to the cavity (by the same amount) and a tuned cavity. For all measurements a signal was injected onto the ITM.

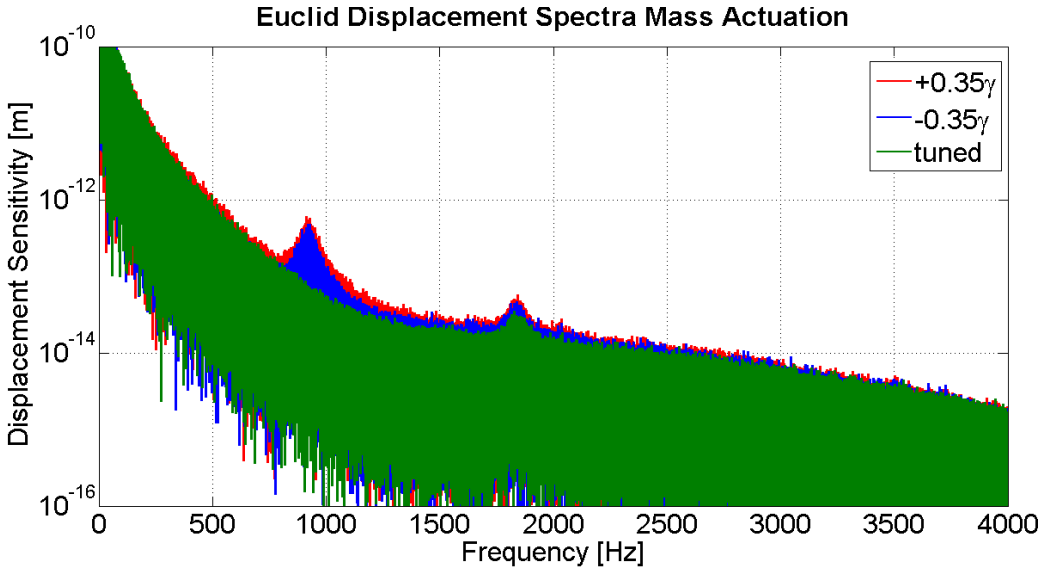

Figure 5.10: EUCLID spectra obtained from injecting a 922 Hz signal onto ITM longitudinal drive coils for both a positively and negatively detuned cavity as well as the on resonance tuned case.

From figure 5.10 we see, as expected, a signal at the injection frequency of about the same size for positive and negative detunings with zero signal for the tuned case. The lack of symmetry can be explained in two ways. Firstly whilst detuned in the spring direction the cavity becomes stiffer and therefore there is less movement of the ETM, the anti spring does not. The more likely effect to cause the asymmetry is that small offsets can propagate through the electronic frequency servo meaning the system is not locked to zero but a small offset from this point.

The second harmonic of the injected signal is seen for both detunings as well. This can be explained by the non-linearity of power fluctuations as the cavity moves along the Airy peak which will be explained in further detail in the following section. For the tuned case the second harmonic is caused by the power fluctuation oscillating around the top of the peak and so appears at twice the injected frequency.

5.3.1.1 Expected Signal Sizes

Before the signal size is calculated it is important to be able to give a value to the peak heights of the spectra. The peak values at 922 Hz are 4.8×10^{-13} m and 5.3×10^{-13} m for positive and negative detunings respectively and 5.7×10^{-14} m for the tuned case. At the second harmonic at 1844 Hz the peak values are 4.8×10^{-13} m and 5.3×10^{-13} m for positive and negative detunings respectively and 5.7×10^{-14} m for the tuned case.

The error on these values is estimated by looking at the change in peak height which is around a 20% change in the peak value or $\pm1 \times 10^{-13}$ m at 922 Hz and $\pm1 \times 10^{-14}$ m at 1844 Hz . The other main error source is the systematics of the EUCLID, which are unknown.

There were three different ways to predict the amount of ETM motion based on other system parameters that were recorded during the measurement. Firstly based on power fluctuations observed on the photodiode located in transmission of the 10 m cavity we can infer the amount of radiation pressure force fluctuation on the ETM and in turn the associated movement this force causes. Secondly by calculating the amount of frequency change from the voltage feedback to the laser PZT the length change of the cavity can be predicted. Finally, based on calibration of the amount of ITM motion for a given input voltage

to the coil driver and the Optickle model of the system giving a ITM-to-ETM coupling of motion transfer function, the ETM motion was obtained.

As stated in Equation 3.11, the transmitted field is directly proportional to the light field circulating inside the cavity and therefore the light field incident on the ETM. The measured value at D.C. of this photodiode of 1.12 V corresponds to the on resonance cavity power of 6 kW. From the spectra the voltage at 922 Hz for the positive detuning is $1.012 \times 10^{-2}\,\mathrm{V_{(rms)}}$, which is $2.86 \times 10^{-2}\,\mathrm{V_{pk}}$, and for the negative detuning is $0.866 \times 10^{-2}\,\mathrm{V_{(rms)}}$, which is $2.45 \times 10^{-2}\,\mathrm{V_{pk}}$. Given the photodiode response is flat in this region this gives a power fluctuation of 154 W and 131 W respectively. This can then be converted to a force $2P/c = 1.03 \times 10^{-6}$ N and 0.87×10^{-6} N, which in turn can be converted into an acceleration of the reduced mass (0.096) $\mathrm{F_{rp}/m_{red}} = 1.073 \times 10^{-5}\,\mathrm{m/s^{-2}}$ and $0.906^{-5}\,\mathrm{m/s^{-2}}$. We can then calculate the amplitude at 922 Hz as $a/\omega^2 = 3.2 \times 10^{-13}$ m and 2.7×10^{-13} m. These values agree well with the spectra obtained from the EUCLID and are within the error on the peak value.

Next we will consider the feedback voltage to the PZT of the laser. Whilst the cavity is tuned, with the injection signal still being driven at 922 Hz, the spike in the feedback at this frequency can be thought of as the ITM motion and converted to an equivalent length change. This can then be subtracted from the feedback voltage, again converted to metres and in the two detuned cases giving the extra motion caused by the ETM.

The feedback voltage to the laser PZT for the tuned case was $2.63 \times 10^{-4}\,\mathrm{V_{pk}}$. This can be converted to frequency, using the laser calibration of 1.35 MHz/V, and then to a length change using Equation 3.19 which gives an ITM motion of $1.26 \times 10^{-11}\,\mathrm{m_{pk}}$. Subtracting this value from the two length changes calculated in the same way for positively and negatively detuned PZT feedback gives 2.5 ×

$10^{-12}\,\mathrm{m_{pk}}$ and $3 \times 10^{-13}\,\mathrm{m_{pk}}$ which gives $3.98 \times 10^{-13}\,\mathrm{m_{rms}}$ and $3 \times 10^{-13}\,\mathrm{m_{rms}}$. These values also agree quite well with the EUCLID spectra in Figure 5.10 and it should be noted that the ratio of the two detuned values is the same as those derived from the power fluctuation calculations detailed above.

Finally we will consider the Optickle model and the amount of ETM motion that it predicts. First of all for this we need to know the amount the ITM is being driven. This was calibrated using an unlocked cavity and driving a slow triangular wave onto the mirror and counting fringes as FSR's pass. This then allows the amount of motion to be extrapolated to 922 Hz reasonably easy as the pendulum responses are well characterised. The downside to this is that the ETM is moving at the same time, however if a large signal is used the effect will be small as the ETM may only pass through 1 fringe but the ITM will pass through 20+. From this method the ITM was calibrated to give a conversion factor m/V at 922 Hz. The signal output from CDS was 8000 CDS counts which corresponds to 2.44 V giving $9.272 \times 10^{-12}\,\mathrm{m_{rms}}$ of ITM motion. This was also calculated above for the PZT feedback calculation to give $8.9 \times 10^{-12}\,\mathrm{m_{rms}}$ and will be the number used due to the directness of the measurement.

Optickle can then be used to calculate the transfer function of ETM motion for given ITM motion, taking into account suspension effects and radiation-pressure effects caused by the optical spring. The transfer functions for various detunings both positive and negative are shown in figure 5.11. As expected, below the spring features you get a 1-to-1 coupling, and above the spring there is a roll off. One can see that anti springs give essentially the same response minus the resonance effect. This is good as it gives the same value of coupling for positive and negative detuning at 922 Hz giving as we saw on the EUCLID peaks of the same size for each detuning.

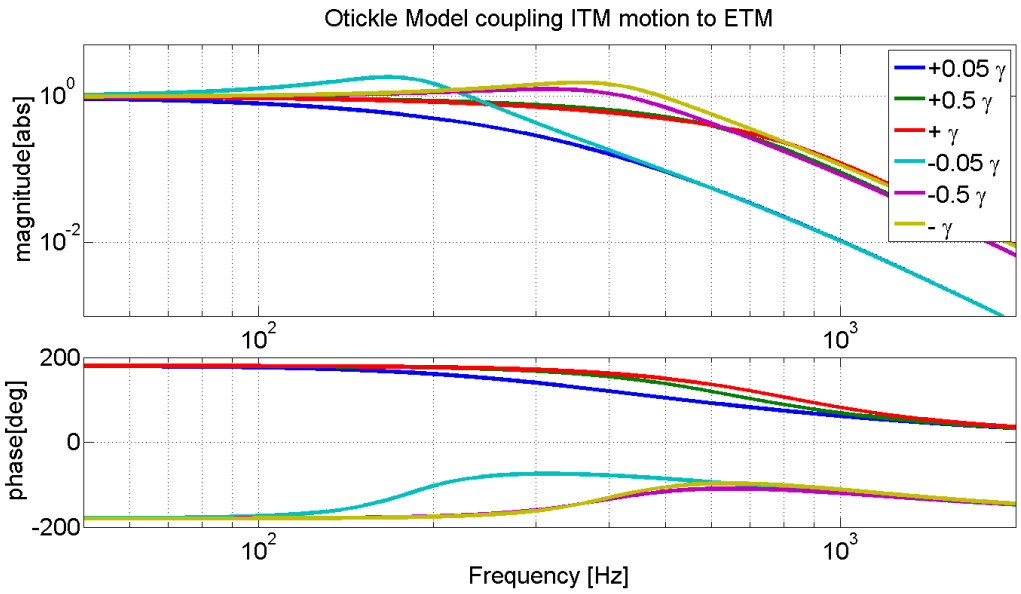

Figure 5.11: Optickle transfer function of coupling between ITM and ETM motion for positive and negative detunings. The value at 922 Hz is around 0.1 for the expected detuning of 0.05γ

From this we can multiply the ITM motion by the coupling factor predicted in Optickle to give the amount of ETM motion. For the values of detuning used this corresponds to a coupling of 0.06 multiplied by ITM motion of 9.272×10^{-12} m, giving an ETM motion of 5.56×10^{-13} m. This value agrees well with the measured spectrum and does not have any asymmetry associated with it and so is the same for positive and negative detunings.

5.3.1.2 Non-Linear Power Fluctuations

The above values deal only with the injection frequency at 922 Hz and the value at that frequency. The bulge surrounding this in the EUCLID trace will be discussed in Section 5.3.3.

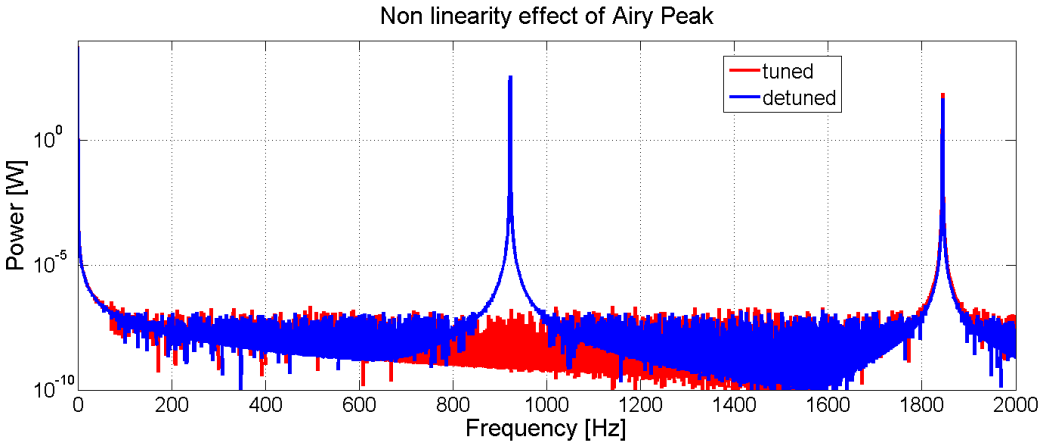

Figure 5.12: Simulation of power spectra for driving a signal up and down an Airy peak, centered on no detuning and detuned. All parameters used, detuning and signal size used were all the same as those of the measurement.

Whilst driving the ITM although the motion is sinusoidal the effective power change it causes is far from it. Changes in cavity length cause changes in power along the Airy-peak intensity profile which is non-linear. This causes signals to appear at multiples of the driving frequency. The plot 5.12 shows the power in each frequency bin by converting a sinusoidal time series of displacement into a power value for each displacement and plotting the spectrum of this. One can see the tuned case giving on-resonance or D.C. power as expected of 6 kW with 0 kW at 922 Hz, due to driving symmetrically around the top of the Airy peak.

For the detuned case, the ratio of power in f to power in $2f$ gives the same ratio as measured with the EUCLID. Table 5.2 summarises the peak-power levels at the first and second harmonic for all three degrees of detuning.

Frequency	Tuned [W]	Detuned[W]
0 Hz	5939	5506
922 Hz	0	304
1844 Hz	46	27

Table 5.2: Table showing modelled peak-power fluctuations caused by non-linearity of Airy peak for tuned and detuned case.

5.3.2 Actuation on the Light

It was also possible to emulate the results of driving the ITM by actuating directly onto the frequency of the light. Driving the mass creates frequency sidebands on the light field. In this section it is described how sidebands were applied directly to the light. This was achieved by adding our injection signal directly into the frequency-stabilisation loop at the error point before it enters the servo. For this reason the signal is not suppressed by the servo gain. This actuation is much more sensitive, making it possible to drive much larger signals which also allowed a good calibration to be made due to the well-characterised nature of the feedback system. It also removed a degree of inaccuracy caused by not being able to drive the ITM perfectly longitudinally and hence introducing slight misalignments. Due to limitations in the amount of current we are able to drive through the coils to actuate on the ITM, the frequency actuation allowed us to see the effects on what would have been a larger motion of the mirror.

The EUCLID spectra for this measurement are shown in Figure 5.13 and a very similar spectrum is observed to that of the mass-pushing case in Figure 5.10. This is good as it should essentially be measuring the same effect.

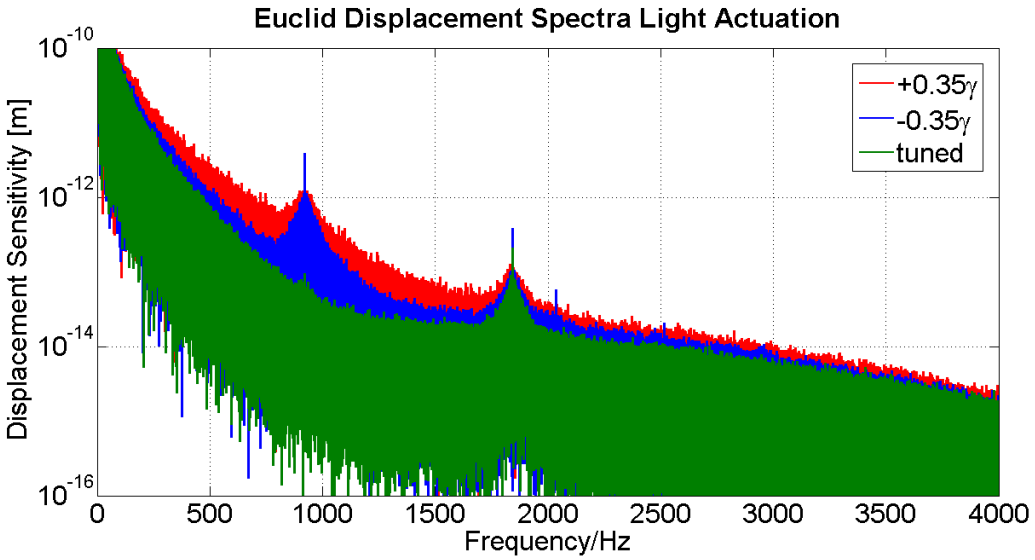

Figure 5.13: EUCLID Spectra obtained whilst injecting 922 Hz signal onto laser feedback servo.

5.3.2.1 Expected Signal Sizes

In the same way as in Section 5.3.1.1, the peak values at 922 Hz are measured on the EUCLID to be 4.8×10^{-13} m and 4.9×10^{-13} m for positive and negative detunings respectively and 2.7×10^{-14} m for the tuned cases. In this case, the error for the peak values is slightly less, due to the signal frequency being clearly above the background. In this case the error is then ± 20% of the background value either side of this frequency. This gives $\pm 2 \times 10^{-13}$ m for the tuned and detuned values at 922 Hz and $\pm 2 \times 10^{-14}$ m at 1844 Hz.

Using the same process as for the mass actuation, the expected ETM motion can now be calculated using the three different methods. We shall again start with power fluctuations on the transmitted photodiode and convert them to a displacement of the ETM. The D.C. transmitted level is 1.02 V again corresponding to a tuned intracavity power of 6 kW. The peaks at 922 Hz for positive and negative detuning are $1.454 \times 10^{-2}\,V_{rms}$ and $1.334 \times 10^{-2}\,V_{rms}$

respectively which give a power fluctuation of 242 W and 221 W and an ETM displacement of $5.2 \times 10^{-13}\,\mathrm{m_{rms}}$ and $4.59 \times 10^{-13}\,\mathrm{m_{rms}}$. Again these values agree well with the observed spectra in Figure 5.13.

The tuned case PZT feedback voltage no longer directly corresponds to a cavity length change as we are not driving the ITM. However, as has been described the mass actuation simply applies frequency sidebands to the light field and so the reverse process allows us to infer an ITM motion based on the sidebands we inject onto the light. Therefore a PZT feedback voltage of at $2.126 \times 10^{-4}\,\mathrm{V_{rms}}$ at 922 Hz gives an effective ITM motion of $3.51 \times 10^{-11}\,\mathrm{m_{rms}}$. Subtracting this from the positive and negatively detuned values of the PZT feedback give an ETM motion of $3.51 \times 10^{-13}\,\mathrm{m_{rms}}$ and $1.56 \times 10^{-13}\,\mathrm{m_{rms}}$. These values again agree very well with the measured peak heights.

Finally we look at the Optickle model coupling factor. Again we need to infer the ITM motion and will use the same value calculated in the PZT feedback calculation. The coupling factor is the same as in Section 5.3.1.1 as the system parameters have not changed. We therefore divide the ITM motion of $3.51 \times 10^{-11}\,\mathrm{m_{rms}}$ by the coupling factor 0.06 giving an expected ETM motion of $2.16 \times 10^{-12}\,\mathrm{m_{rms}}$. This value, although bigger than that from previous calculations, is still quite close to the expected value given the large error on the peak height.

5.3.3 EUCLID Spectra Analysis

We will now discuss some of the surprises that arose from the experiment and the reasons behind them. It is quite clear on the EUCLID spectra in Figures 5.13 and 5.10 that we are seeing far more than a single frequency injection. What we observe is a bulge centred around the injected 922 Hz.

Looking more closely at the bulge it is possible to see that it has structure and is symmetric around 922 Hz.

The fact that the bulge has symmetry suggests it arises from a non-linear process in the system causing beating with the injection signal. Several checks were made to pin down the source of this effect. First of all some of the more obvious potential sources of this effect are dealt with. The signal we are injecting is single-frequency and not drifting as the output comes from CDS which is locked to a 10MHz GPS signal. Most importantly, in all of the channels that were recorded it was possible to see the signal as a clear single frequency. This eliminates many of potential causes as the feedback signal being single frequency meant the cavity mirrors were not actually moving with a bulge of frequency structure. The throughput power-monitoring photodiode signal was also single frequency, meaning the change in radiation pressure on the ETM was also a single-frequency force change.

The EUCLID was checked with no light in the system and simply driving the coils of the ETM longitudinally. From this we saw some up conversion of low frequency pendulum modes to beat with the injection frequency. Although the injection spike was still quite clear above these and not the rounded bulge we see in figures 5.13 and 5.10.

It was possible to quickly rule out other potential sources of noise such as scatter by driving the ETM with light not locked but occasionally resonant in the arm cavity which produced the same measured spectrum as when there was no light present. It was also possible to rule out misalignment effects as recording both photodiode and auto-alignment signals showed no bulge.

There remain only two other places in the system where additional non-linearity can enter. Firstly the error signal demodulation mixer, if it is approaching satu-

ration. This cannot be the case as this effect would be visible in the arm-cavity error-signal spectrum which it is not. Secondly the non-linearity arising from driving up and down the Airy peak of the cavity. This has already been shown to cause the $2f$ signal peaks for the detuned cases but does not further explain the bulge.

From previous experiments, the EUCLID is limited by noise due to up conversion of large low frequency motion caused by pendulum modes. For these reasons, and given the inner workings are not fully disclosed and the fact that non-linear up-conversion has been seen in the EUCLID, this can be the only way to explain the bulge effect seen.

It was possible to model these effects to try to recreate what has been measured. By taking the displacement time series data from the EUCLID with no injections (just monitoring freely hanging ETM) and adding on a single frequency injection and then adding on the non-linearity of the Airy peak and then adding a non-linear process (assumed to be the EUCLID readout) it was possible to create the spectrum shown in Figure 5.14. This was achieved by adjusting the amount of second-order non-linearity which was seen to have the effect of suppressing the injection frequency by putting power into the sidebands or bulge. This is a good approximation of what is seen in figures 5.13 and 5.10.

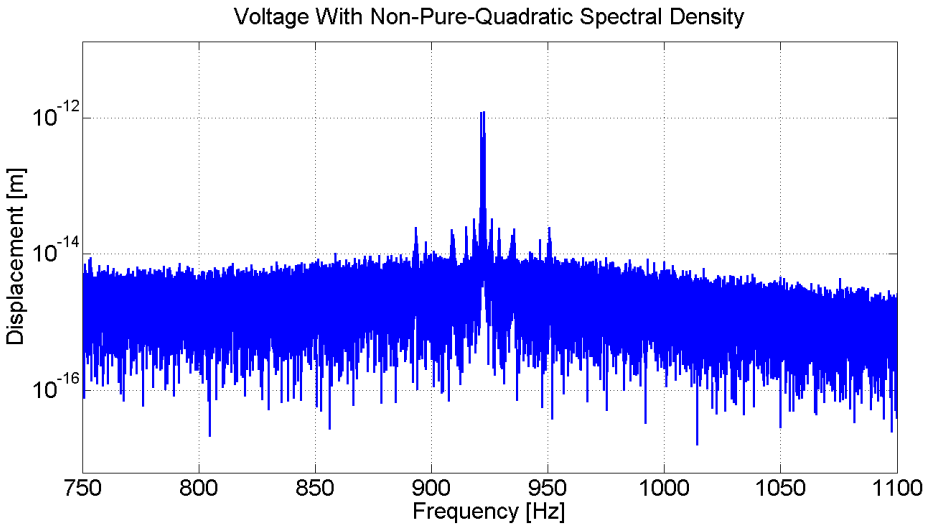

Figure 5.14: Simulation of the combination of non-linearities in the Euclid and the Airy peak.

5.3.4 Static Radiation Pressure

With the use of a local readout it becomes possible to disentangle cavity motion, which cannot be separated from frequency with an exact measure of the cavity mirror displacement. Here we investigate the static offset to the ETM mirror position caused by the build-up of cavity power and hence radiation-pressure force as the frequency stabilisation is switched on and the cavity locks.

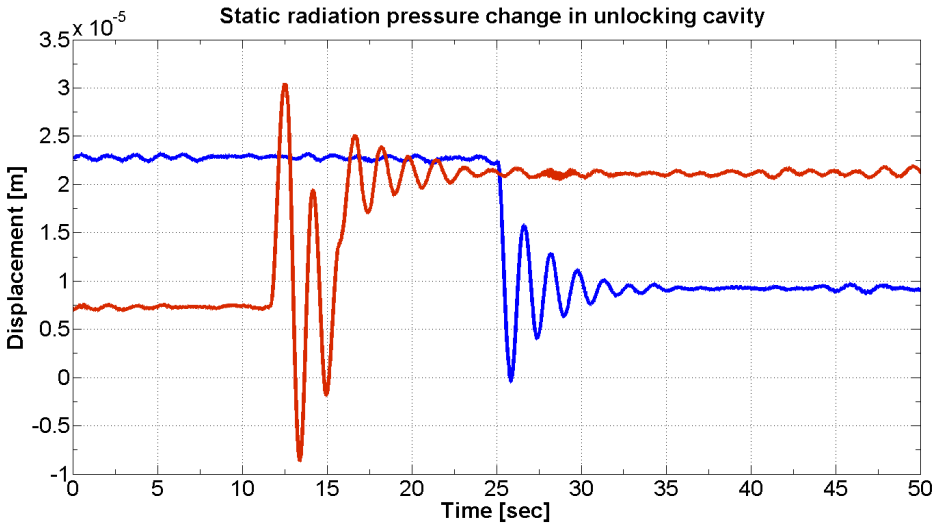

Figure 5.15: Frequency stabilisation servo is switched on (red) or off (blue) and the static offset caused by radiation pressure allows the intracavity power to be calculated.

By looking at the static displacement offset of the mirror position caused by locking the cavity, the increase in restoring force of the pendulum required to balance the radiation pressure force described in Figure 3.8 can be calculated. This then allows an estimate to be made of the intracavity power. Here we assume the pendulum sits at equilibrium when unlocked and the displacement when locked is entirely down to radiation pressure.

$$\text{The average displacement (unlock) for first } 20\,\text{secs} = 2.279 \times 10^{-5}\,\text{m}$$
$$\text{and for the last } 15\,\text{secs} = 0.922 \times 10^{-5}\,\text{m}.$$
$$\text{The average displacement (lock) for first } 10\,\text{secs} = 0.729 \times 10^{-5}\,\text{m}$$
$$\text{and for the last } 25\,\text{secs} = 2.0123 \times 10^{-5}\,\text{m}.$$

This gives a change in displacement of 1.39×10^{-5} m and 1.35×10^{-5} m respectively.

Knowing the displacement of the pendulum from equilibrium, the resulting

restoring force can be calculated. The optical power required to produce this radiation-pressure force can then be derived.

For the pendulum length $L = 0.3\,\mathrm{m}$ the last stage is what is most important for small displacements. The displacement angle θ is then

$$\theta = \arctan(\frac{X_{euc}}{L_{pen}}) = 1.079 \times 10^{-3} \text{ and } 1.05 \times 10^{-3}, \tag{5.4}$$

where X_{euc} is the displacement measured by the EUCLID. The pendulum restoring force F_{res} can then be calculated to be

$$F_{res} = mg\sin(\theta) = 4.55 \times 10^{-5}\,\mathrm{N} \text{ and } 4.43 \times 10^{-5}\,\mathrm{N}. \tag{5.5}$$

This allows the intracavity power to be calculated as, $P_{cav} = F_{res}c/2 = 6825\,\mathrm{W}$ and $6645\,\mathrm{W}$.

These values agree very well with the predicted values based on the measured cavity finesse and input power. It is also possible to estimate intracavity power by looking at the initial acceleration of the mass. As the servo is switched on and the cavity is stabilised to the peak of a resonance, the power build-up is almost instantaneous in a high-finesse cavity of the order ms (see figure 3.7). It can then be said that the acceleration of the mass in the initial instance is entirely dominated by the radiation pressure force. If we assume that the light power is at full in this region we can then calculate first the acceleration of the mass from the Euclid time series data, then the force required to accelerate the mirror, and finally the associated optical power required to give that force.

In practice it turns out this method is highly dependent on the start and end times taken. The results obtained varied from predicted intracavity power as

low as 2.5kW up to 12 kW. The reason for this is thought to be due to the dynamic nature of the setup making measurements over short time periods very difficult. With the mirrors moving freely, it is clear that the longer averaging of the first method was the best way of calculating intracavity power in this way.

5.3.5 Radiation Pressure Instability

In our experimental system it is also possible to see the effect of increased input power not only changing alignment in a static way but also in a dynamic way. By misaligning the cavity it was possible to see a pendulum-mode instability caused by the non-centered beam acting on the mirror, seen in figure 5.16. The beam being off centre exerts a torque on the mirror when power builds up in the cavity, which in turn misaligns the cavity, reducing the radiation pressure and torque, allowing the mirror to move back to the original position.

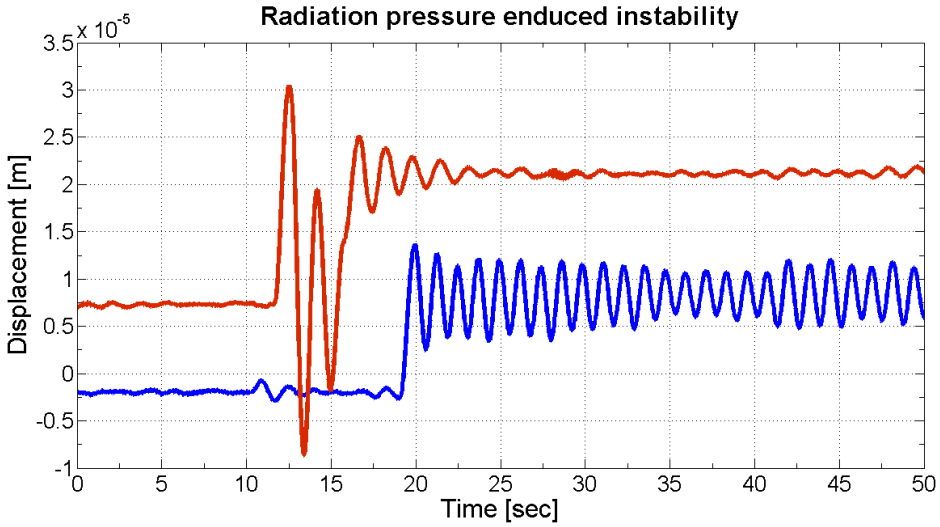

Figure 5.16: Lock capture with same input power but different alignment values. Red trace shows the well aligned case and the blue trace the misaligned case.

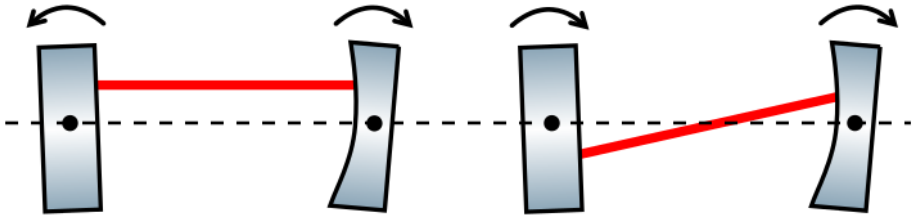

Figure 5.17: Illustration of the two Sidle Sigg instabilities. On the left a higher frequency oscillation occurs and is a more unstable configuration. On the right we see a more rigid, lower frequency, instability. The arrows indicate mass rotation direction caused by increase in force along the beam axis and dots indicate approximate centres of rotation.

As can be seen in Figure 5.16, the red trace indicates a well-aligned cavity whereby before and after lock the cavity is stable and the ETM is not moving more than expected. The blue trace shows the case of a misaligned cavity whereby after the system is locked the ETM continues to oscillate, with less power coupling given by the smaller displacement from equilibrium.

This instability is well documented and named the "Sidle Sigg" instability after they were the first to witness the effect [60]. There are two types of instability depending on the misalignment of the cavity, shown in figure 5.17. Both points of reflection on the same side of the centre of rotation or one on either side, causing an increase or decrease in the frequency of the oscillation.

This effect has been studied in prototype-sized devices [61], giving rise to the following equation to calculate the frequency shift of the fundamental mode based on input power and cavity geometry:

$$\omega_{\pm}^2 = \omega_o^2 + \frac{P_{cav} L}{Ic} \left[\frac{-(g_1 + g_2) \pm \sqrt{4 + (g_1 - g_2)^2}}{1 - g_1 g_2} \right], \tag{5.6}$$

where $g_{1,2} = 1 - \frac{L}{R_{1,2}}$ with $R_{1,2}$ the radius of curvatures of the cavity mirrors.

For this measurement, $P_{cav} = 6\,\mathrm{kW}$, $g_1 = 1$ as the input mirror is flat (i.e. very large radius of curvature), and $g_2 = 1 - 9.78/15 = 0.348$. With the fundamental pendulum resonance $\omega_0 = 0.55\,\mathrm{Hz}$ this gives a new fundamental frequency caused by the instability of $0.576\,\mathrm{Hz}$ or $0.76\,\mathrm{Hz}$, depending on the misalignment of the cavity.

By calculating the frequency of the oscillation recorded it agrees very well with the higher-frequency case. Regardless of direction of misalignment, the higher-frequency oscillation was always seen. The reason for agreement with the higher frequency is likely due to the much larger mass of the ITM, meaning misalignment to either side of centre on the ETM causes a torque that has a much greater effect on ETM rather than the ITM alignment.

5.4 Summary and Discussion

It was possible to show the coupling of motion from one mirror to another using photons which had never "seen" the initial mirror. We were able to analytically calculate the response of the system, showing that the main coupling comes simply from a change in power from moving along the Airy peak, causing a change in radiation pressure force. The detuned cavity therefore converts phase fluctuations to amplitude fluctuations. By actuating on the light we were able to successfully emulate the effect of mirror motion, achieving very good agreement.

Chapter 6

Optical Spring Enhanced Classical Measurement

In this chapter we investigate further applications of the optical-spring effect, first to confirm the analysis of the previous chapter using a novel readout method and secondly to show the increase in gain of the system due to the resonance features and how it can be utilised.

The optical-spring effect allows the cavity response to be changed by varying the detuning of the cavity. By these means it is possible to create responses that give more signal gain than could be achieved by increasing the light power or substituting mirrors of higher quality, if those options are even available. This enhancement of frequency response can be applied to any relevant cavity, a good example would be the signal-recycling cavity of a gravitational wave detector. Furthermore, the option of detuning allows dynamic tuning of the sensitivity of a detector, for example, to allow tracking of the dominant frequencies in an evolving gravitational wave signal over time [62]. In this chapter we use a novel readout method to determine the optical spring response in the

region where the cavity linewidth has a large effect. It is further shown that creating an optical spring can cause an increase in gain, such that frequency noise is suppressed more than would otherwise be possible. Finally we show that predictions from our numerical model of the system, i.e. the Optickle model agrees very well with experimental results, and that with adjustments to the setup much greater improvements could be realised.

6.1 Aim

The aim of this experiment is to show two things. First that for various detunings the optical spring behaves as modeled for the parameters used in Chapter 5. A test signal is injected into the detuned 10 m cavity and the response is read out using the readout cavity. The spring response is then calculated for various detunings and compared to the Optickle model. This method of characterising the optical spring is significantly more sensitive than that described in Chapter 5.

The second point is to show that the extra gain provided by the optical spring resonance improves the frequency-noise limited sensitivity of the readout cavity measurement. The idea behind this experiment is that the laser is stabilised to the 10 m cavity and so the response of this cavity is imposed onto the light. If the frequency-readout cavity is frequency-noise limited it should be possible to see the change in response caused by detuning, and at some frequencies improve on this value due to the optical-spring resonance.

Finally, we will show through simulation the best noise improvement that could be obtained through this method whilst making only unobtrusive changes to the system.

6.2 Setup

This experiment uses a very similar setup to the one described in Chapters 4 and 5, an overview of which is shown in Figure 6.1. The main difference is the addition of what has previously been referred to as the frequency readout cavity. This cavity is 10 cm in length and both cavity mirrors are monolithically suspended for ultra-low-noise performance. The 10 m cavity is locked to the peak of the resonance by feeding back a correction signal to the laser frequency. The 10 cm cavity is locked using feedback to the position of the ETM *via* coil-magnet actuators.

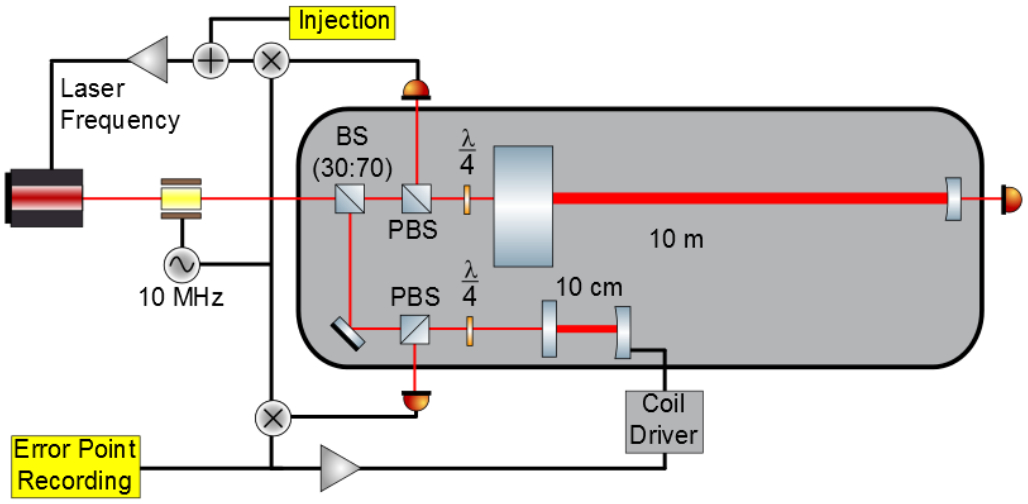

Figure 6.1: Overview of the two-cavity setup showing the feedback to the laser frequency and cavity length to control both cavities separately.

The 10 cm cavity uses two monolithically suspended mirrors to reduce ground motion and thermal motion in the suspensions. The aim, as part of experiments beyond the scope of this thesis, was to reduce all other noise sources to a level below the thermal noise from the mirror coatings, to enable measurement of that noise. The result, for application in the work of this thesis, is that the

very low displacement noise associated with the mirrors of the 10 cm cavity allows it to act as a sensitive measure of frequency noise because of its short length relative to the 10 m cavity. It can therefore act as a sensitive probe of the opto-mechanical interactions within the 10 m cavity as it is detuned.

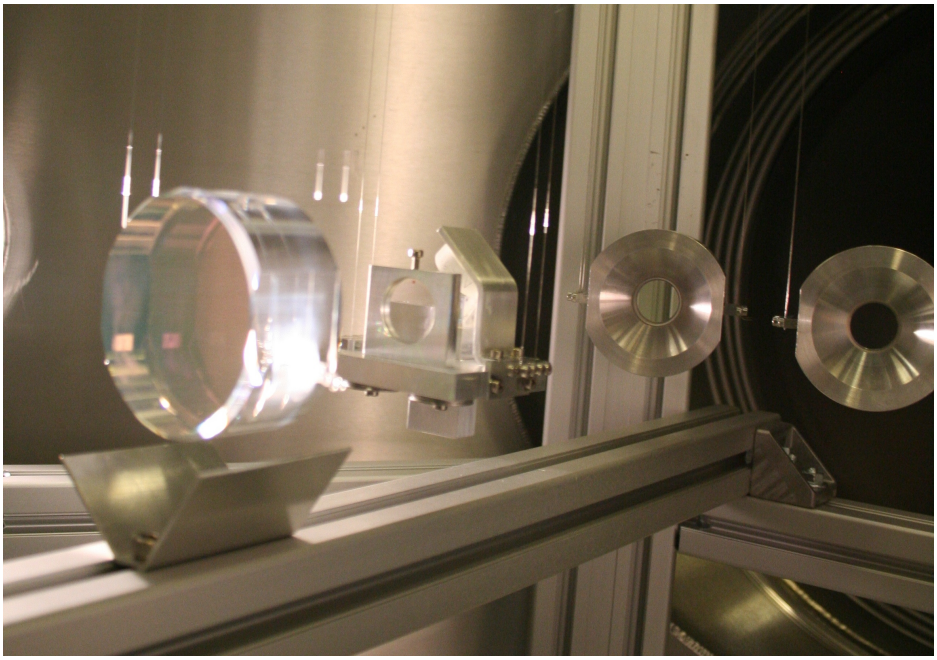

Figure 6.2: From right to left: the beam-splitter picks off light for this cavity from the main beam; the second of two steering mirrors (the first is off-right in the image) directs the light to the cavity through the quarter-wave plate polarising beam-splitter pick-off near the centre of the picture; finally, towards the left of the image is the ITM seen supported on its 4 fused-silica fibres.

The frequency-readout cavity obtains its reflection PDH locking signal in the same way as the 10 m cavity does, namely with a wave plate and PBS in front of the cavity. The detected beam is then demodulated using an RF photodiode in the same way as the 10 m cavity. The error signal is then fed to an analogue electronic servo which feeds back to coils mounted on a reaction mass that control the longitudinal position of the ETM. This gave a unity gain

Cavity Property	Value
Finesse	4870
Linewidth	306 kHz
FSR	1.49×10^9 Hz
input power	360 mW

Table 6.1: Table showing measured properties of frequency readout cavity.

at around 2.2 kHz seen in Figure 6.3. The coil-magnet actuators are similar to those used for damping the suspension oscillations in the 10 m ITM. The suspensions themselves are damped using eddy-current dampers in the same way as the ETM of the 10 m is, already described in Section 4.3.

The inertia of the suspended mirror gives the coil-magnet actuator a $1/f^2$ response. The cavity fringes pass through relatively quickly as the suspended mirrors swing (in the short cavity, a small motion corresponds to large changes in resonant frequency) and locking is assisted by employing a trigger system to activate the servo system only when the correct TEM_{00} mode is briefly resonant. This allows the controller to be operated with high gain, yet avoids the risk of the cavity locking on to unwanted modes.

As noted above, the coil-magnet actuator has a response of $1/f^2$ and so the locking servo needs to be rolling on in the area to balance the drop-off and have the correct $1/f$ crossing, to give the desired phase margin around the UGP, and thus ensure stability of the loop. The servo and electronics are shown in Appendix B, and the locked cavity transfer function is shown in Figure 6.3.

The photodiode used to lock the 10 m cavity was optimised to allow for the full range of detuning. The downside of this is that the frequency noise was

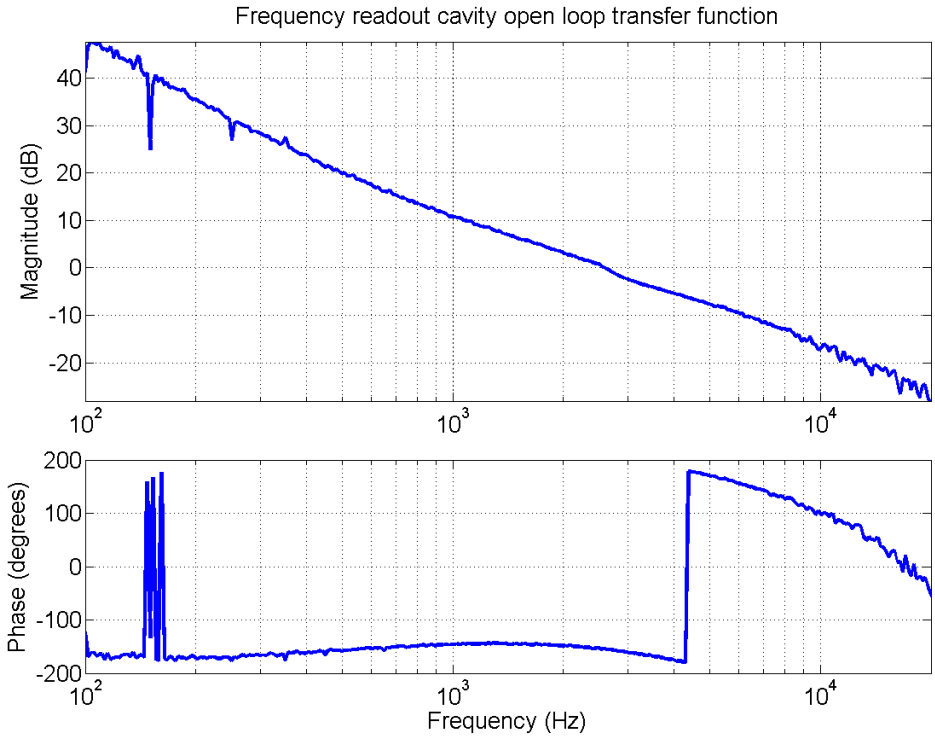

Figure 6.3: Transfer function of the servo stabilising the length of the frequency reference cavity.

not suppressed as best it could be by using a much higher-gain photodiode which could be tuned to detect the 10 MHz signal. Due to the lower-gain photodiode, the UGP of the 10 m cavity lock was 8 kHz compared to 100 kHz achievable using the high-gain photodiode and high-frequency EOM feedback briefly described in section 4.6.

To determine that the measurement is indeed limited by frequency noise of the laser, the recorded readout-cavity-feedback-signal spectrum was measured. It was then possible to subtract the loop gain and the electronic transfer functions to obtain the spectrum of the light entering the cavity, which should give laser frequency noise. Figure 6.4 shows the feedback signal and the expected frequency noise, and both agree very well in the 100 - 300 Hz region where the measurements in this chapter have been taken.

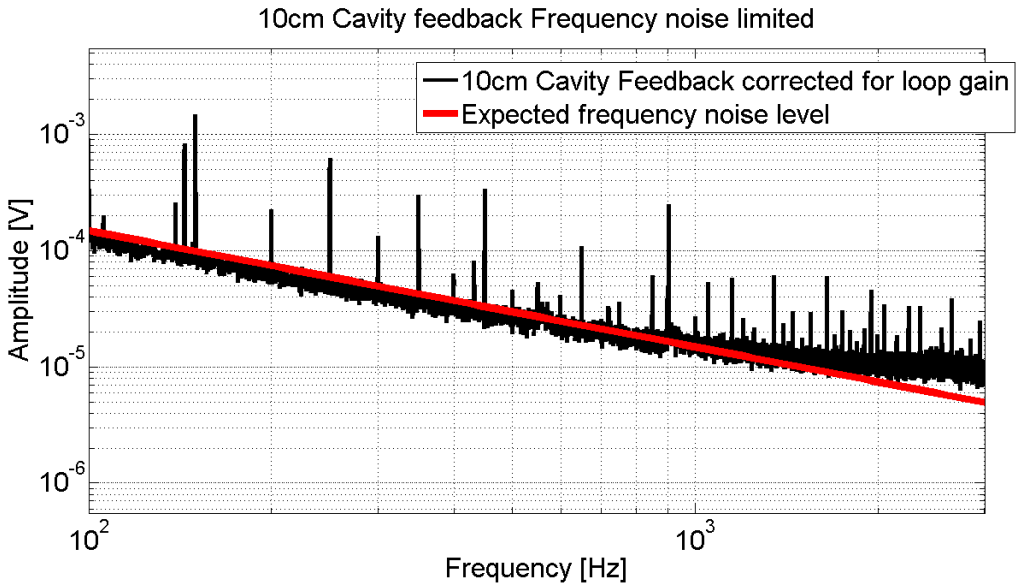

Figure 6.4: 10 cm cavity feedback monitor adjusted for loop gain compared to expected laser-frequency noise level.

6.3 Measurements

6.3.1 Optical Spring Response

The objective of the first measurement was to show that the Optickle model was a good match to the measured spring response for a range of detunings. The lower measurement noise compared to the method of Chapter 5 allows the system parameters to be matched to the model and therefore to be determined more precisely. This also provides confirmation of the coupling of motion predicted by the model.

A swept-sine frequency response measurement was taken for each value of detuning of the 10 m cavity. The test signal was injected into the frequency-stabilisation loop before the servo, shown in Figure 6.1. The signal was read out at the 10 cm cavity error point. Both points are shown in Figure 6.1. Due to frequency readout being 3 orders of magnitude more sensitive than the EUCLID, smaller signals can be used and both higher and lower frequencies can now be measured. Previous measurements of this type generally required larger signals to be injected to propagate through the entire system. This has the negative effect of generally changing the state of the system by changing the operating point. Using smaller injection signals means this is not the case. During these individual swept sine measurements for each detuning the system maintained the same lock and the system was smoothly changed from one detuning to the next to avoid step changes which would have brought a risk of knocking the system out of lock. All of the individual swept-sine measurements were taken during a single stretch of locking so as to provide consistency of the locking points.

Each measurement taken was then divided by the non-detuned case to show the

effect of detuning only. This removes the effects of electronic gains throughout the feedback loop, and the actuator responses, and it makes visualising the plots much more straightforward as the only difference between plots is caused by the detuning.

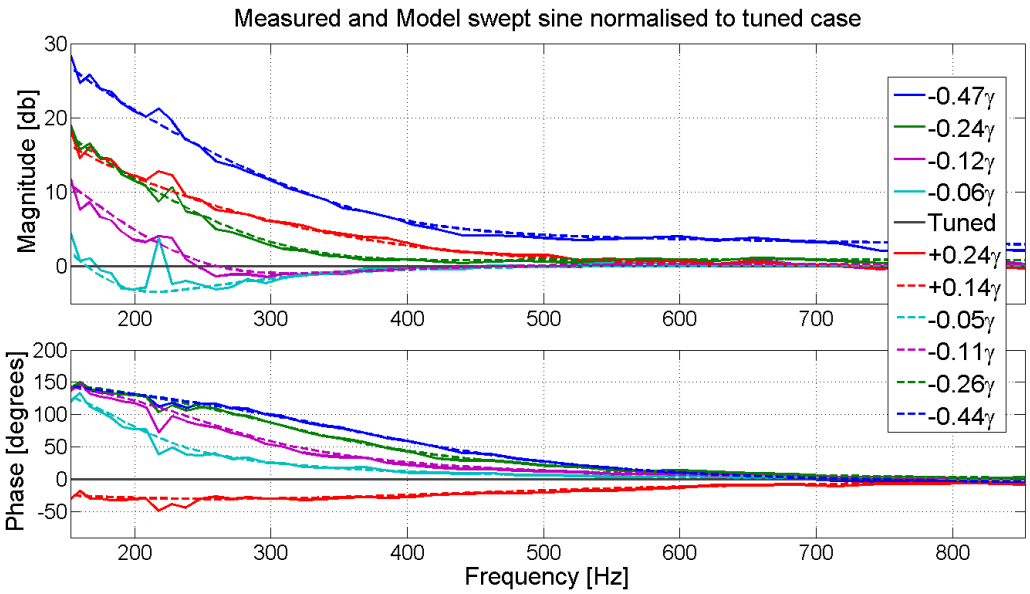

Figure 6.5: Measured optical-spring response in sensitive cavity normalised to the tuned case, measured (solid), and modelled (dashed).

Figure 6.5 shows the experimental measurements and the model which fits the values of detuning to the curves obtained. These agree very well, which further supports results obtained in the previous chapter. The feature seen at 210 Hz is a mechanical mode of the system, thought to be a violin mode of one of the suspensions and which has been rung up by different amounts by slightly different alignments and cavity powers caused by detuning.

6.3.2 Sensitivity Improvement

The aim of the second measurement is to improve the sensitivity of the readout cavity by detuning the 10 m cavity to suppress frequency noise. The noise spectrum of the 10 cm cavity error point was recorded in CDS for various detunings. The cavity was only detuned small amounts as this gives optical spring resonances with the largest Q. The larger the Q the greater the gain and therefore the greater the frequency-noise suppression and also the most obvious change in noise spectrum in the readout cavity.

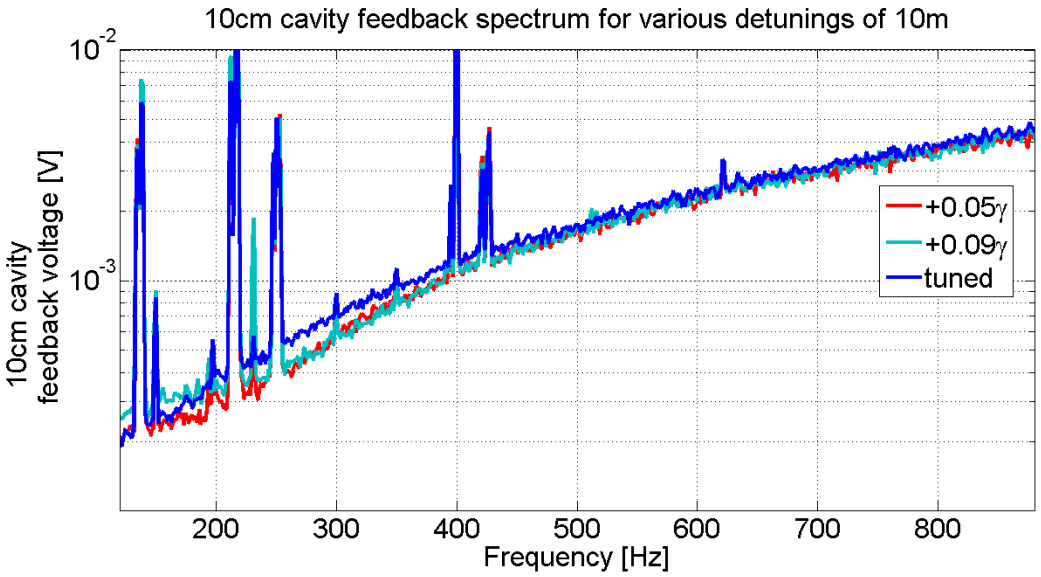

Figure 6.6: Noise spectrum of measurement cavity with two detunings of frequency reference showing a small improvement in performance.

In the frequency region from 200 - 300 Hz the noise is lower in the detuned cases compared to the tuned case, representing an improvement in displacement sensitivity in that region. This is due to the frequency-noise spectrum having the response of the 10 m cavity imposed upon it. The extent of the improvement agrees well with the spring measurements from figure 6.5 where

the increase in sensitivity is the same as the amount of gain increase caused by the optical spring for these levels of detuning. Larger detunings are not shown, as in these cases there is no frequency at which the gain of the cavity is greater than the non-detuned case and so no improvement would be seen in the sensitivity measurements.

6.4 Further Simulation

A great deal has been learned about optomechanically coupled systems throughout this work. The models have agreed well with all measurements in this regime and it is interesting to look at relatively small changes that could be made for future projects. The most important factor in the noise improvement measurements was to have an optical spring resonance of as high a Q as possible, at the expense of bandwidth. The limiting factor in preventing this in our system was the cavity linewidth, which cannot be easily changed without replacing one of the cavity optics.

For discussion purposes we will now investigate the potential response from the system given two realistic changes. Firstly increasing the cavity linewidth by increasing the transmission of one of the cavity mirrors from 2.4 ppm to 240 ppm. This increases the cavity linewidth from 570 Hz to 1800 Hz. The second change was to increase the input power to the system to the maximum output from the laser amplifier, 5 W.

In Figure 6.7 the bulge in the 200-300 Hz region is much larger due to the larger optical spring resonance. This shows it would be possible to achieve, up to 10 dB of noise improvement across a broad frequency range 10's-100 Hz. Greater noise improvement would be possible at lower frequencies at the loss of

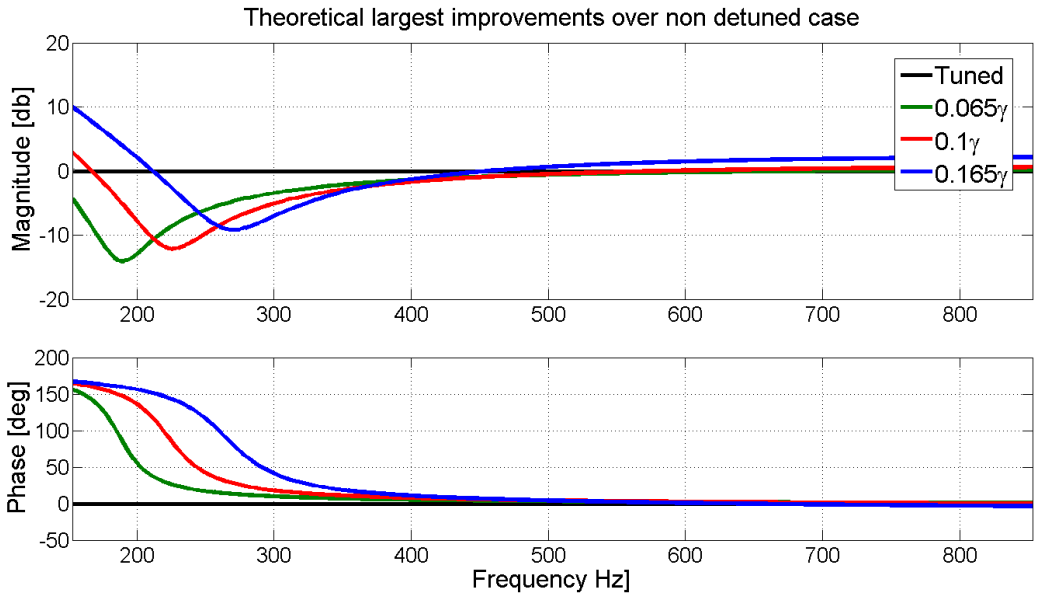

Figure 6.7: Model of potential improvement by increasing cavity linewidth and using full power available for different values of detuning.

bandwidth. A small penalty is paid at higher frequencies, but this is smallest for small detunings such is the case here. It should be noted that the absolute value of detuning in metres is now much larger due to the larger cavity linewidth, but as a fraction of the linewidth this is still considered a small detuning.

6.5 Summary and Discussion

The use of harmonic oscillators in suspended optical cavities can be employed for narrow-band improvement in sensitivity if the resonance can be arranged to be at the frequency of interest. This can be done dynamically in milliseconds by adjusting the detuning of the cavity.

The limiting case in this experiment was the low linewidth of the cavity, giving

a high finesse which helped to provide large amounts of circulating power. This put an upper limit on the spring response that was not limited by the light power but by the drop-off caused by the cavity at higher frequencies. It is noted that, as only a small detuning is required to produce the highest-Q optical spring, it may be possible to employ a photodiode amplifier of higher gain as the full range of detunings may not be required.

The effects shown can be greatly amplified when applied to gravitational wave detector setups. This is due to the much larger ratio of optical power to mirror mass, 6 kW and 100 g in this experiment to 800 kW and 40 kg in Advanced LIGO. However, the linewidth of the cavity still provides an upper limit to radiation-pressure effects, due not to the finesse but to the much longer arm lengths used.

Although the work described here has not been at the "quantum-level", the effects described will still behave in the same way in the quantum regime. Radiation pressure will be caused by statistical variations in the light beam, but if the cavity is detuned it will still behave as a harmonic oscillator. The resonance features described also can improve performance beyond the quantum limits described in Chapter 5.

Chapter 7

Conclusions and Future Work

Optical rigidity has been suggested to be one of the key concepts in advanced gravitational wave detectors. As such investigation was required at the prototype level to ensure this technology is suitably mature for integration into full-scale detectors.

This thesis aims to push optical-spring technologies forward in technical readiness as well as prototyping innovative concepts. We were able to verify that it is possible to gather information on the position of the input mirror of an optically rigid cavity via the local readout interferometer, the photons of which have never interacted with the input mirror.

We also showed that the presence of an optical spring in a 10 m cavity provides a peak in the optical gain which enhances the frequency stability of the cavity. So, this is a good example of how optical springs can be used to enhance the precision of a classical interferometric measurement.

The work described in this thesis has paved the way for further experiments in this field. Currently, work is beginning in the Glasgow 10 m prototype on

a dual-carrier configuration in a coupled-cavity system whereby two separate light fields interact with a common cavity mirror. The principle here is to create an optical spring with one carrier and an anti spring with the other. This improves the stability of the system due to the addition of a positive damping term arising from the anti spring. Furthermore this setup allows us to broaden the resonance feature, giving a wider bandwidth improvement.

One step before the dual carrier would be to investigate the high measurement frequency and large cavity detuning region of Figure 3.9. At this point the spring constant changes sign and therefore gives a region of both positive spring constant and positive damping. This increase in stability could lead to innovation in quantum locking setups and creation of stable feedback loops without the need for electronics giving ultra-low noise performance.

In summary, gravitational wave detectors are soon going to be limited in sensitivity by the quantum nature of light. The successful demonstration of an optical-bar topology was an important step towards surpassing the standard quantum limit.

Appendix A

Cavity Properties

A.1 10 m Cavity

Property	Value
ETM transmission	2.4 ppm
ITM transmission	416 ppm
ETM loss	35 ppm
ITM loss	30 ppm
10 m Cavity length	9.78 m
10 cm Cavity length	10 cm
Modulation index	0.6
Linewidth	578 Hz
Input light power	850 mW
Intracavity power on resonance	6 kW

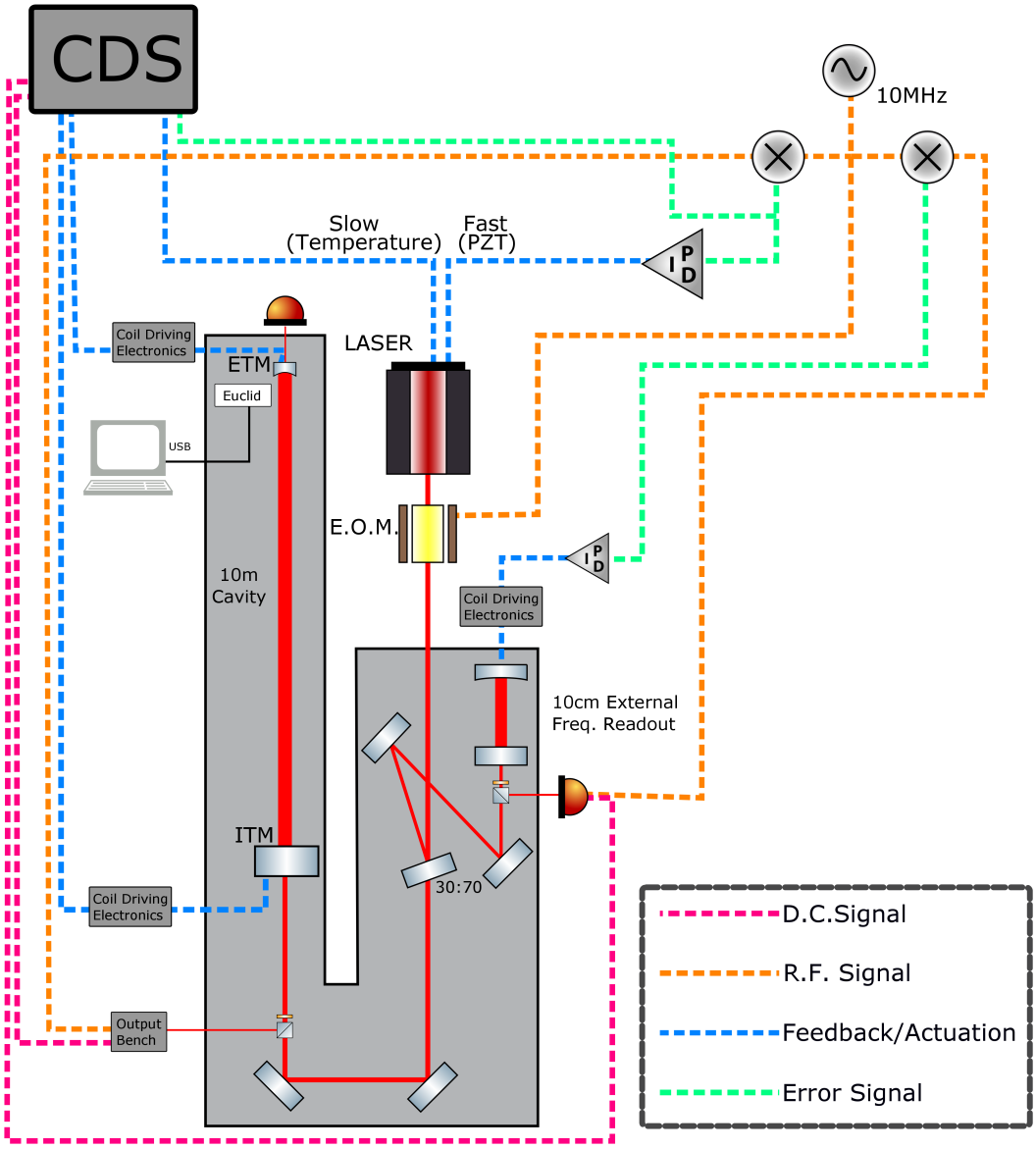

Figure A.1: Full system layout

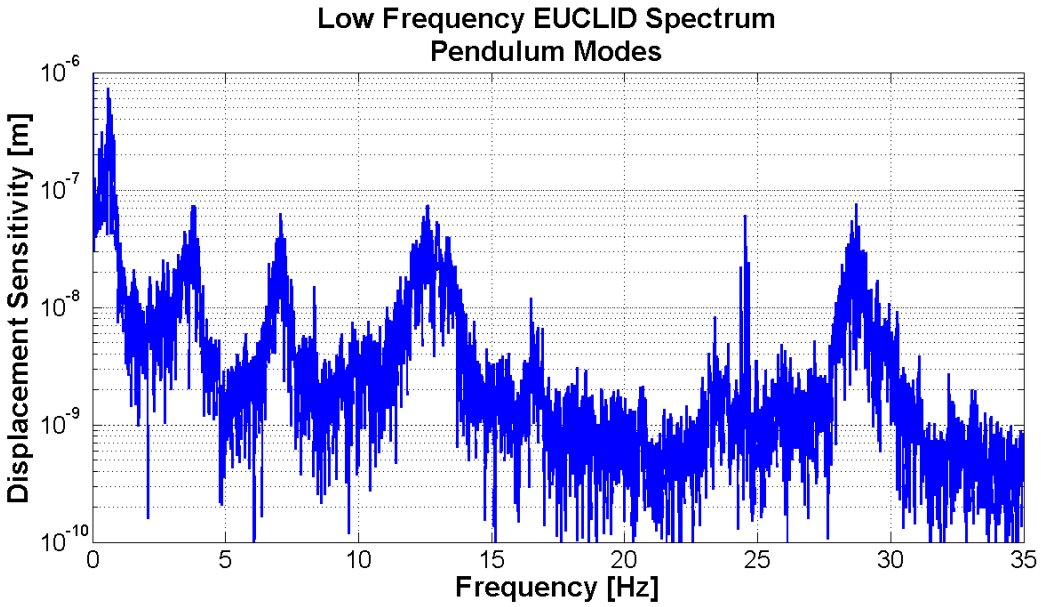

Figure A.2: Low-frequency end of the spectrum obtained from EUCLID showing Pendulum modes.

Appendix B

Electronics Circuit Diagrams and CDS Filters

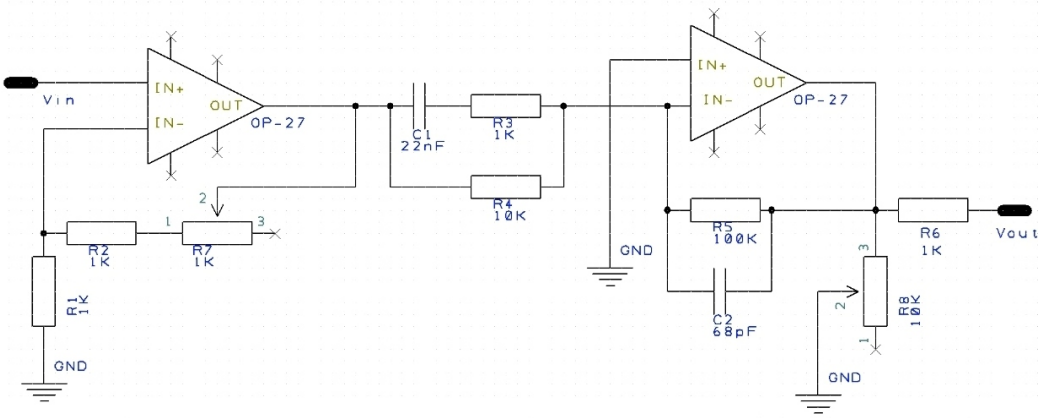

Figure B.1: Frequency readout servo electronics.

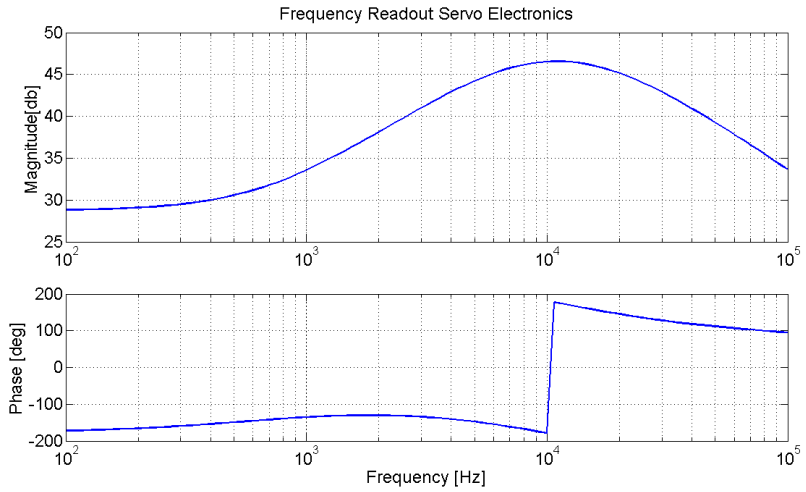

Figure B.2: Frequency readout cavity servo electronics transfer function.

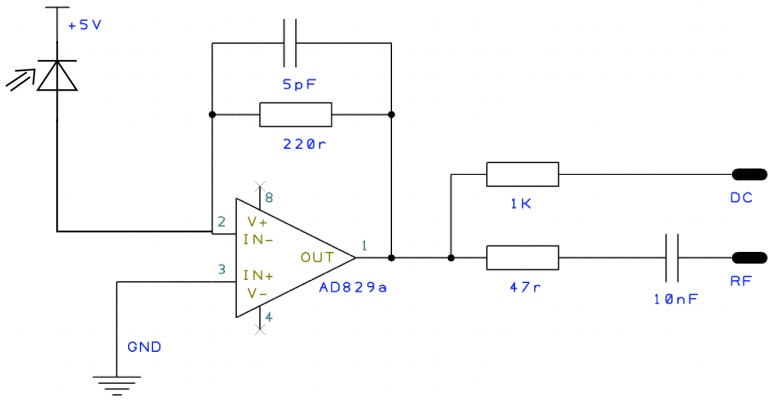

Figure B.3: 10 m cavity photodiode.

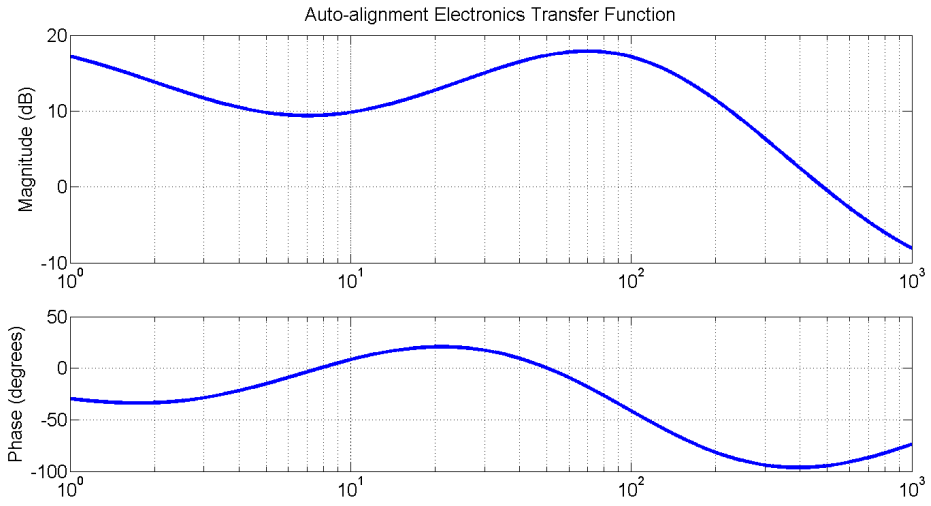

Figure B.4: Bode plot of CDS filters used for Auto alignment feedback.

Figures B.5, B.6 and B.7 show the electronics of the frequency-stabilisation servo, showing the common path electronics and the PZT feedback shaping which is then applied to the PZT directly and also further filtered using CDS as shown in Figure B.7.

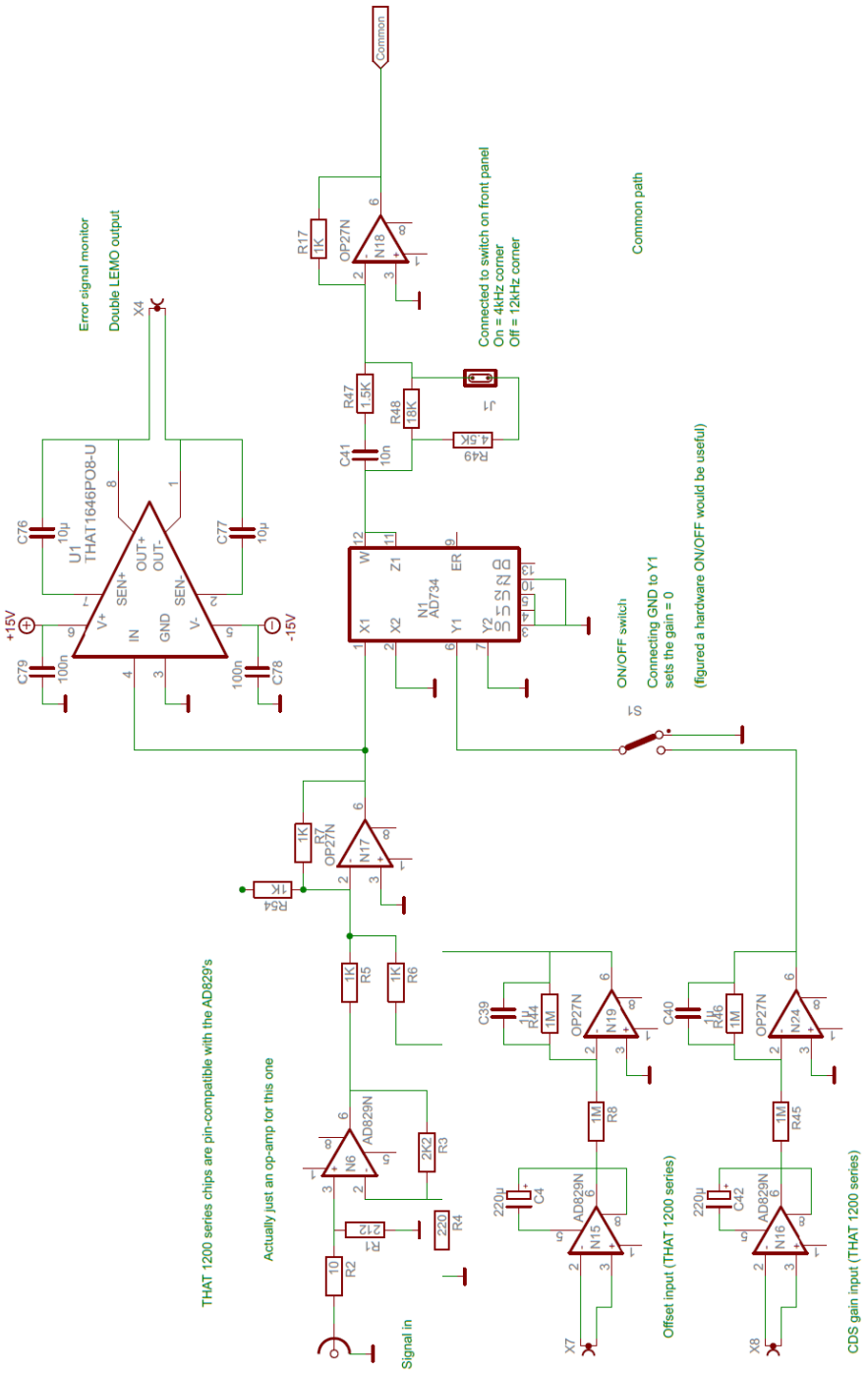

Figure B.5: Common path electronics of frequency stabilisation servo.

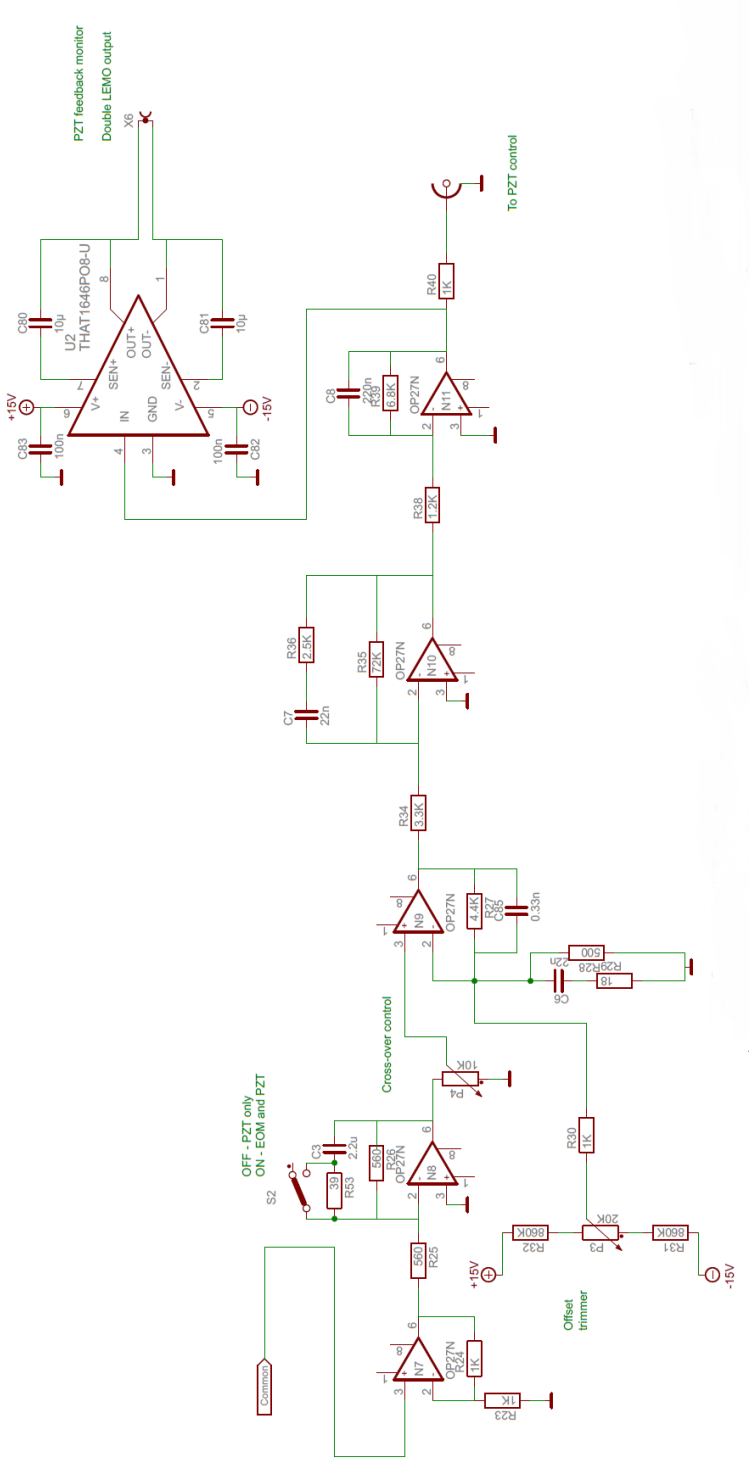

Figure B.6: PZT frequency stabilisation feedback electronics.

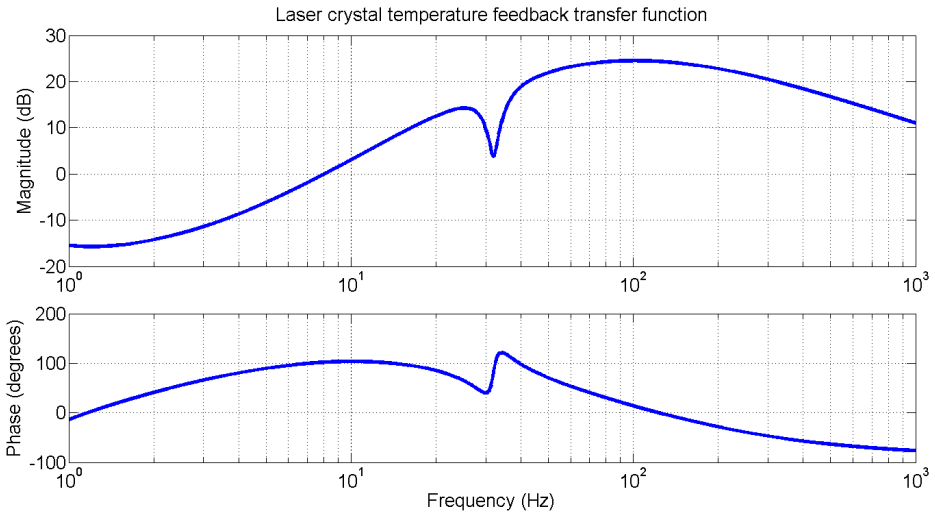

Figure B.7: Bode plot of CDS filters used for laser crystal temperature feedback. Notch filter at 32 Hz due to large suspension bounce mode at this frequency.

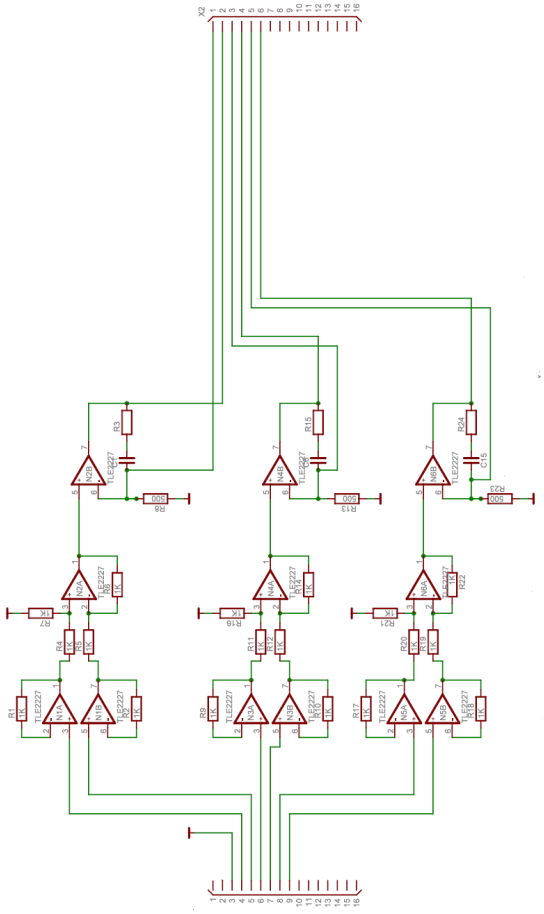

Figure B.8: Coil driver electronics. Pairs of outputs are wired to either end of the same coil and there are 3 coils and hence 6 outputs. The circuit differentially recieves the tilt rotation and longitudinal signals before setting the gain and the sign of the signal going to each coil.

Appendix C

Scripts and Code

C.1 Finesse

```
##Finesse model of high finesse cavity

m m1 0.999549 0.000416 0 n1 n2      # mirror R=0.999434 T=416ppm,
                                    #  phi=0 losses = 30 ppm
s s1 9.78 n2 n3                     # space  L=9.78m
m m2 0.9999686 0.0000024 0 n3 n4    # mirror R=0.9998476 T=2.4ppm,
                                    # phi=0  losses = 30 ppm

l i1 0.85 0 n0                      # laser P=850mW, f_offset=0Hz

mod eo1 10M 0.6 3 pm n0 n1          # phase modulator f_mod=10MHz
                                    # midx=0.6 order=3

#pd1 transmitteddc 0 0 n4           #measure finesse
```

```
#pd1 reflecteddc 0 0 n1              #measure visibility
pd1 interdc 0 0 n2                   #intracavity power
#pd1 error 10M 0 n1                  #demodulated error

xaxis m2 phi lin -0.1 0.1 5000      # xaxis: tune mirror m2
                                     # from -0.5 to 0.5 (1000 steps)
yaxis abs                            # plot 'as is'
```

C.2 Optickle

```
%% Create an Optickle Fabry-Perot
%% "definition file"

function opt = simple_cav

Pin = 0.85;   %input power 2.5
vMod = (-1:1);  %modulation freqeucies
fMod3 = 10e6;     % modulation frequency 18MHz
vFrf = [ -fMod3 0 fMod3 ];
lCav2 = 9.78;     % cavity length

%Mechanics
w = 2 * pi * 0.3;         % pendulum resonance frequency
w_pit = 2 * pi * 0.5;     % pitch mode resonance frequency
dampRes = [0.01 + 1i, 0.01 - 1i]; % assumpion


  %mirror parameters
```

```
tITM = 416e-6;    % power transmission: assumming no losses
tETM = 2.4e-6;    % power transmission: assumming no losses
lITM = 33e-6;     % Power loss on reflection
lETM = 30e-6;     % Power loss on reflection

mI = 2.7;         % mass of input mirror
rIM = 0.15;       % test-mass radius
tIM = 0.1;        % test-mass thickness

mE = 0.1;         % mass of end mirror
rEM =0.25;
tEM =0.019;

  %%%%%%%%%%%%%%%

  % create model
  opt = Optickle(vFrf);

  %% add a source
    %% [opt, sn] = addSource(opt, name, vArf, z0, z)
    %% vArf - amplitudes of each RF component (Nrf x 1)
    %% z0 - beam range = (waist size)^2 * pi / lambda
    %% z - distance to waist (negative if beam is converging)
 opt = addSource(opt, 'Laser', sqrt(Pin) * (vMod == 0));

    %% opt = addRFmodulator(opt, name, fMod, aMod)
    %% [opt, sn] = addRFmodulator(opt, name, fMod, aMod)
    %% name - name of this optic
    %% fMod - modulation frequency
```

```
   %% aMod - modulation index (imaginary for phase, real for amplitude)
aMod = 0.6;
opt = addRFmodulator(opt, 'Mod3', fMod3, 1i * aMod);


% [opt, snLink] = addLink(opt,snFrom,nameOut,snTo,nameIn,len)
opt = addLink(opt, 'Laser', 'out', 'Mod3', 'in', 0.1);

%% add mirrors
%   opt = addMirror(opt, name, aio, Chr, Thr, Lhr, Rar, Lmd, Nmd)
%%  angle, curvature, power transmission HR,
%%  Loss HR, p reflectifity AR, loss, refractiv index

opt = addMirror(opt, 'ITM', 0, 0, tITM, lITM);
opt = addMirror(opt, 'ETM', 0, 1/15, tETM, lETM);

%
opt = addLink(opt, 'Mod3', 'out', 'ITM', 'bk', 3);
opt = addLink(opt, 'ITM', 'fr', 'ETM', 'fr', lCav2);
opt = addLink(opt, 'ETM', 'fr', 'ITM', 'fr', lCav2);



%% set some mechanical transfer functions
iEM = (3 * rEM^2 + tEM^2) / 12;  % TM moment / mass
iIM = (3 * rIM^2 + tIM^2) / 12;  % TM moment / mass

iI = mI * iIM;          % moment of input mirror
```

```
iE = mE * iEM;          % moment of end mirror

opt = setMechTF(opt, 'ITM', zpk([], -w * dampRes, 1/mI));
opt = setMechTF(opt, 'ETM', zpk([], -w * dampRes, 1/mE));

opt = setMechTF(opt, 'ITM', zpk([], -w_pit * dampRes, 1/iI),2);
opt = setMechTF(opt, 'ETM', zpk([], -w_pit * dampRes, 1/iE),2);
%-------------------------

%% tell Optickle to use this cavity basis
% opt = setCavityBasis(opt, 'ITM', 'ETM');


%[opt, sn] = addSink(opt, name, loss)
%[opt, snLink] = addLink(opt,snFrom,nameOut,snTo,nameIn,len)
opt = addSink(opt, 'REFL');
opt = addLink(opt, 'ITM', 'bk', 'REFL', 'in', 0.5);


%% detectors
%[opt,snProbe] = addProbeAt(opt,name,snOpt,nameIn,freq,phase);
opt = addProbeAt(opt, 'REFL_DC', 'REFL', 'in', 0, 0)  ;
opt = addProbeAt(opt, 'REFL_f3I', 'REFL', 'in', fMod3, 0);
opt = addProbeAt(opt, 'REFL_f3Q', 'REFL', 'in', fMod3, 90);

% add unphysical intra-cavity probes
opt = addProbeIn(opt, 'IX_DC', 'ITM', 'fr', 0, 0);
opt = addProbeIn(opt, 'EX_DC', 'ETM', 'fr', 0, 0);
```

Now that the parameters of the system have been defined, the second section of code below sets the variables you wish to vary and plots the results.

```
%%
%% run-file
%%

function simple_cav_run

% create the model
 opt = simple_cav;

% get some drive indexes
 nETM = getDriveIndex(opt, 'ETM');
 nITM = getDriveIndex(opt, 'ITM');

% get some probe indexes
 nREFL_f3I   = getProbeNum(opt, 'REFL_f3I');
 nREFL_DC    = getProbeNum(opt, 'REFL_DC');

 nIX_DC    = getProbeNum(opt, 'IX_DC');
 nEX_DC    = getProbeNum(opt, 'EX_DC');

%%%%%%%%%%%%%%%%%%%%%%%%%%%% ETM sweep %%%%%%%%%%%%%%%%%%%%%%

% takes all probes (from the "definition-file") and plots them
  pos_start = zeros (opt.Ndrive, 1);
  pos_end   = zeros (opt.Ndrive, 1);
```

```
  pos_start(nETM) = -6e-7;
  pos_end(nETM)   = 6e-7;

  x=linspace(pos_start(nETM), pos_end(nETM),5000);

  [pos,sigDC,fDC]=sweepLinear(opt,pos_start, pos_end,5000);

  figure()
    plot (x,abs(sigDC))
    plot(x,sigDC)
      legend ('DC-AC', 'I-AC', 'Q-AC','test')
      grid on
      xlabel('ETM Displacement')
      ylabel('power')

%%%%%%%%%%%%%%%%%%%%%%%%%%%%%%%%%%%%%%%%%%%%%%%%%%%%%%%%%%%%%%%%%%%%%%%%%%%

% Retrieve some drive and probe serial numbers from
% the Optickle model
 nEXdrive = getDriveNum(opt, 'ETM', 'pos');
 nREFL_Iprobe = getProbeNum(opt, 'REFL_f3I');
 nREFL_Qprobe = getProbeNum(opt, 'REFL_f3Q');

% Set up the limit of our sweep
 pos = zeros(opt.Ndrive, 1);
 pos(nEXdrive) = -8e-11; % [meters]
 % 6e-7 for FSR; 8e-11 for Power peak

% Do the sweep
```

```
 [poses, sigDC, fDC] = sweepLinear(opt, pos, -pos, 201);

 figure()
   subplot(2,1,1);
     plot(poses(nEXdrive,:), sigDC(nREFL_Iprobe, :), '-', ...
     poses(nEXdrive,:), sigDC(nREFL_Qprobe, :), '-');
     legend('REFL I [phase = 0]', 'REFL Q [phase = 90]');
     xlabel('cavity detuning [meters]');
     ylabel('signal [Watts]');
     title('Pound-Drever-Hall error signal');
     grid on;

   subplot(2,1,2);
     nIXprobe = getProbeNum(opt, 'IX_DC');
     plot(poses(nEXdrive,:), sigDC(nIXprobe, :));
     title('Intra-cavity power');
     xlabel('cavity detuning [meters]');
     ylabel('power [Watts]');


f = linspace(153, 853, 300)';

% compute the DC signals and TFs on resonances
  [fDC, sigDC0, sigAC0, mMech0, noiseAC0] = tickle(opt, [], f);

  pos = zeros(opt.Ndrive, 1);

% compute the same a little off resonance
  pos(nITM) = -1.6e-12;
```

```
  [fDC1, sigDC1, sigAC1, mMech1, noiseAC1] = tickle(opt, pos, f);
  pos(nITM) = -3.2e-12;
  [fDC7, sigDC7, sigAC7, mMech7, noiseAC7] = tickle(opt, pos, f);
  pos(nITM) = -4.8e-12;
  [fDC3, sigDC3, sigAC3, mMech3, noiseAC3] = tickle(opt, pos, f);
  pos(nITM) = -6.4e-12;
  [fDC6, sigDC6, sigAC6, mMech6, noiseAC6] = tickle(opt, pos, f);
  pos(nITM) = -8.2e-12;
  [fDC8, sigDC8, sigAC8, mMech8, noiseAC8] = tickle(opt, pos, f);
   pos(nITM) = -10.54e-12;
  [fDC9, sigDC9, sigAC9, mMech9, noiseAC9] = tickle(opt, pos, f);
   pos(nITM) = 3.2e-12;
  [fDC2, sigDC2, sigAC2, mMech2, noiseAC2] = tickle(opt, pos, f);

% make a response plot
  h0 = getTF(sigAC0, nREFL_f3I, nITM);
  h1 = getTF(sigAC1, nREFL_f3I, nITM);
  h3 = getTF(sigAC3, nREFL_f3I, nITM);
  h6 = getTF(sigAC6, nREFL_f3I, nITM);
  h7 = getTF(sigAC7, nREFL_f3I, nITM);
  h8 = getTF(sigAC8, nREFL_f3I, nITM);
  h9 = getTF(sigAC9, nREFL_f3I, nITM);
  h2 = getTF(sigAC2, nREFL_f3I, nITM);

  h = [h9,h8,h6,h3,h7,h1,h0,h2];
  hn = [h0,h0,h0,h0,h0,h0,h0,h0];

  h = hn./h;
```

```
    ang = 180 * angle(h)/pi;
    mags = abs(h);
    magdb = 20*log10(mags);


figure()
    subplot(2, 1, 2)
    plot(f,ang, 'LineStyle',':')
        axis([153 853 -200 200])
        ylabel('phase[deg]')
        grid on
    subplot(2, 1, 1)
    plot(f, magdb, 'LineStyle',':')
        axis([153 853 -10 30])
        ylabel('mag[abs]')
        grid on
    title('AC-PDH Response for Detuned Cavity (ITM) divided by...
     0 detuned case', 'fontsize', 18);
    legend('On resonance','-1.6e-12','-3.2e-12','-4.8e-12',...
    '-6.4e-12','-8.2e-12','-10e-12','+3.2e-12');
%%%%%%%%%%%%%%%%%%%%%%
```

Bibliography

[1] I. Newton. Philosophiæ Naturalis Principia Mathematica. (1687).

[2] J C. Maxwell. A Dynamical Theory of the Electromagnetic Field. *Philosophical Transactions of the Royal Society*, (1865).

[3] A. Einstein Zur Elektrodynamik bewegter Körper. *Annalen der Physik*, (1905).

[4] A. Einstein Die Grundlage der allgemeinen Relativit¨atstheorie. *Annalen der Physik*,(1916).

[5] C. Cutler An Overview of Gravitational Wave sources *Preecedings of 16th international conference of General Relativity*, (2002).

[6] J. Aasi et al. Gravitational waves from known pulsars: results from the initial detector era. *arXiv:1309.4027*, (2013).

[7] P. A. R. Ade et al. BICEP2 I: Detection Of B-mode Polarization at Degree Angular Scales. *arXiv:1403.3985*, (2014).

[8] R. A. Hulse and J. H. Taylor. Discovery of a pulsar in a binary system. *APJL*, **195** P51 (1975).

[9] J. Weber General relativity and Gravitational waves. *Interscience Publishers Inc., New York*, (1961).

[10] H. Grote The GEO 600 status. *Class. Quantum Grav.*, **27** 084003 (2010).

[11] B. Abbott et al. LIGO: The Laser Interferometer Gravitational-Wave Observatory. *arXiv: 0711:3041*, (2009).

[12] T. Accadia et al. Virgo: a laser interferometer to detect gravitational waves. *Journal of Instrumentation*, P3012 (2012).

[13] B. Willke. The geo-hf project. *Class. and Quantum Grav.*, **23** 207 (2006).

[14] G. Harry et al. Advanced ligo: the next generation gravitational wave detector. *Class. Quantum Grav.*, **27** 084006 (2010).

[15] http://www.cascina.virgo.infn.it/advirgo/docs.php.

[16] K. Somiya Advanced ligo: the next generation gravitational wave detector. *Class. Quantum Grav.*, **29** 124007 (2012).

[17] D. Herriott. Off-axis paths in spherical mirror interferometers. *Appl. Opt.*, **3** 4 (1964).

[18] B. J. Meers Recycling in laser-interferometric gravitational-wave detectors. *Phys. Rev. D*, **38** 2317 (1988).

[19] J. Mizuno Resonant sideband extraction: a new configuration for interferometric gravitational wave detectors. *Phys. Lett. A*, **175** 5 (1993).

[20] S. Danilishin Quantum measurement theory in Gravitational wave detectors. *Living Rev. Relativity*, **15** (2012).

[21] S. M. Aston Update on quadruple suspension design for Advanced LIGO. *Class. Quantum Grav.*, **29** 23 (2012).

[22] R. Lawrence Adaptive thermal compensation of test masses in aLIGO *Class. Quantum Grav.*, **19** 7 (2002).

[23] B. Sorazu Experimental test of higher order Laguerre Gauss modes in the 10m Glasgow prototype interferometer. *Class. Quantum Grav.*, **30** 035004 (2013).

[24] S. Huges Seismic gravity gradient noise in interferometric gravitational wave detectors. *Phys. Rev. D*, **58** 122002 (1998).

[25] Ling-An Wu Generation of Squeezed States by Parametric Down Conversion. *Phys. Rev. Lett.*, **57** 2520 (1986).

[26] H. Vahibruch GEO600 squeezed light source. *Class. Quantum Grav.*, **27** 8 (2010).

[27] S. Hild Beyond second generation of LIGO *arXiv:gr-qc/1111.6277* (2011).

[28] C. Graf Design of a speed meter interferometer proof-of-principle experiment. *http://arxiv.org/abs/1405.2783* (2014).

[29] S. Hild Sensitivity studies for third-generation gravitational wave observatories. *Phys. Rev. Lett.*, **28** 094013 (2011).

[30] https://www.elisascience.org

[31] F. Antonucci LISA Pathfinder: mission and status. *Class. Quantum Grav.*, **28** 094001 (2011).

[32] K. A. Strain Thermal lensing in recycling interferometric gravitational wave detectors. *Phys. Lett. A*, **194** 124 (1994).

[33] M. Rakhmanov Dynamics of Laser Interferometric Gravitational Wave Detectors. *PhD Thesis, California Institute of Technology*, (2000).

[34] J. Mizuno Comparison of optical configurations for laser-interferometric gravitational-wave detectors. *PhD Thesis, University of Hannover*, (1995).

[35] R. W. P. Drever Laser phase and frequency stabilization using an optical resonator. *Appl. Phys. B*, **31** 97 (1983).

[36] F. Ya. Khalili Frequency-dependent rigidity in large-scale interferometric gravitational-wave detectors. *arXiv:gr-qc/0107084* (2001).

[37] F. Ya. Khalili Observation of optical spring effect in a microtoroidal optomechanical resonator. *arXiv:gr-qc/0107084* (2001).

[38] M. Hossein-Zadeh Measurement of radiation-pressure-induced optomechanical dynamics in a suspendedFabry-Perot cavity. *Opt. Lett.*, **31** 12 (2007).

[39] B. S. Sheard Observation and characterization of an optical spring. *Phys. Rev. A,* **69** 051801 (2004).

[40] M. Plissi GEO 600 triple pendulum suspension system: Seismic isolation and control. *Rev. Sci. Inst.*, **71** 2539 (2000).

[41] M. Edgar Experimental Investigations into Diffractive Optics and Optomechanical Systems for Future Gravitational Wave Detectors. *PhD Thesis, University of Glasgow*, (1995).

[42] M. Plissi Investigation of eddy current dampinjg of multi stage suspensions *Rev. Sci. Inst.*, **75** 11 (2004).

[43] http://www.coherent.com/products/?2064/Mephisto-Mephisto-S

[44] http://www.wenzel.com/model/streamline/

[45] http://www.minicircuits.com/pdfs/RAY-3.pdf

[46] G. Heinzel LISO http://www.mpg.de/ros/geo600_docu/soft/liso/

[47] E. Morrison Automatic alignment of optical interferometers. *Applied Optics*, **33** 22 (1994).

[48] E. Morrison Experimental demonstration of an automatic alignment system for optical interferometers. *Applied Optics*, **33** 22 (1994).

[49] A. Thuring JamMt http://www.sr.bham.ac.uk/dokuwiki/doku.php?id=geosim:jammt.

[50] A. Friese Finesse http://www.gwoptics.org/finesse/.

[51] N. Smith Optickle https://github.com/Optickle/Optickle.

[52] S. Danilishin Quantum Measurement Theory in Gravitational-Wave Detectors *Living Rev.*, **15** (2012).

[53] A. Khalaidovski Status of the GEO 600 squeezed-light laser. *arXiv:1112.0198.* (2011).

[54] V B Braginsky. Optical bars in graavitational wave antennas. *Phys. Lett. A,* **232** (1997).

[55] S. Danilishin. To the practical design of the optical lever intracavity topology of gravitational-wave detectors. *Phys. Rev. D*, **73** (2006).

[56] H. Rehbein Local readout enhancement for detuned signal-recycling interferometers. *arXiv:0705.2987v3* (2007).

[57] P. Grangier Quantum non-demolition measurements in optics. *Nature*, **396** (1998).

[58] S M. Aston Optical Read-out Techniques for the Control of Test-masses in Gravitational Wave Observatories. *PhD Thesis, University of Birmingham*, (2011).

[59] http://www.polytec.com/int/products/vibration-sensors/single-point-vibrometers/.

[60] J A. Sidles and D. Sigg Optical torques in suspended Fabry-Perot interferometers. *Phys. Lett. A*, **354** (2006).

[61] E. Hirose Angular instability due to radiation pressure in the LIGO gravitational-wave detector. *Applied Optics*, **49** 18 (2010).

[62] B J. Meers Dynamically tuned interferometers for the observation of gravitational waves from coalescing compact binaries. *Phys. Rev. D,* **47** 6 (1993).